UNIVERSITÀ
DEGLI STUDI
DI TRIESTE

UNIVERSITÀ DEGLI STUDI DI TRIESTE

XXXVI CICLO DEL DOTTORATO DI RICERCA IN FISICA

The noisy gates approach and its applications to quantum computation

Settore scientifico-disciplinare: **FIS/02 FISICA TEORICA E MODELLI MATEMATICI**

DOTTORANDO
Michele Vischi

COORDINATORE
Francesco Longo

SUPERVISORE DI TESI
Angelo Bassi

ANNO ACCADEMICO 2022/2023

Contents

Chapter 1

Introduction

The advent of quantum computers promises a paradigm shift for computation, unlocking unprecedented computational power to solve many problems with renowned high impact, e.g. optimization problems, artificial intelligence, molecular and material simulations. However, the practical realization of quantum utility to advance industry relevant applications is hindered by some technological limitations, among which noises affecting the ideal functionality of quantum computers. While quantum error correction techniques are envisioned as the standard solution to such issues, their successful implementation necessitates challenging breakthroughs yet to come.

Despite their imperfections, over the past three decades quantum computing devices have evolved from being experiments in a lab, to complex machines able to tackle non trivial tasks. It is becoming increasingly accepted that the best strategy to be adopted is to direct efforts to accelerate practical applications involving the presently available quantum hardware, acknowledging its imperfections. This sets the main goal at this stage of development: it becomes of paramount importance to understand and accurately model the impact of noises on quantum computation. This entails the characterization and modeling of noises acting on quantum devices, as well as the development of classical simulation tools that accurately mimic the effects of a given noise model on quantum circuits. These efforts constitutes the solid grounds onto which it is possible to devise techniques to actively suppress the impact of noises. Particularly, this realizes the vision of turning a hardware problem into a software problem, as the average effect of noises can be suppressed via effective error mitigation strategies, that are software techniques that, differently from full quantum error correction, aim at reducing the impact of noises to a level sufficient to enable quantum utility.

As a milestone towards this long term vision, the core result of the thesis lies in the introduction of a novel method for classically simulating the noisy behavior of quantum circuits, named the noisy gates approach. We argue that this approach

successfully surpasses existing methods by implementing the most efficient and accurate simulator of the noisy results of a quantum circuit. The idea behind the noisy gates approach is to improve the accuracy of the results by relaxing the main physical assumptions of standard simulation methods while maintaining, or even improving, the computational costs to run simulations. This results in a more accurate simulator using less computing resources.

The simulation of noisy digital gate-based quantum circuits is typically implemented by adding appropriate quantum operations, what we refer to as *noise gates*, before and after each ideal gate of a quantum circuit. This is generally assumed to be legitimate since the time scales of noises are very slow compared to the ideal gate evolution, resulting in a formal decoupling of the two dynamics. However, separating the action of the gate from that of the noise does not represent a faithful description of what happens during a quantum computation. The controlled action on the qubits generating the gates and the environment act simultaneously and potentially affect each other. In this scenario, neglecting their interplay leads to inaccurate predictions, especially when the number of gates and qubits is relatively large, which is actually the regime where simulations are more interesting.

The noisy gates approach, as underlined by its name, efficiently incorporates environmental effects into the evolution of gates, employing linear stochastic Schrödinger equations to directly model state vector evolution. This allows not only to evolve state vectors instead of density matrices (this is possible also for standard methods) but also the linearity of the equations reduces the total amount of matrix vector multiplications, improving computational costs. The most notable result of the thesis is to show the superiority of the noisy gates approach tailored to superconducting devices, by rigorously benchmarking it against standard simulation methods, demonstrating closer accuracy to analytical solutions and to real noisy quantum computers.

The application of the noisy gates approach is then extended to simulate noisy optical circuits within the dual rail framework, rooted in the second quantization formalism. Successfully adapting the approach to this domain is not straightforward. The noisy version of optical elements is derived underlining the versatility of the approach. The simulation is tested on a variational quantum algorithm for linear optics.

The second part of the thesis introduces two complementary results. First, a modification of the noisy gates approach is presented, enabling applications beyond error analysis for quantum circuits. In particular, an efficient quantum algorithm for simulating open quantum systems is devised, grounded in the generalization of the noisy gate approach to quantum stochastic Schrödinger equations. Notably, the algorithm exhibits a constant ancilla overhead, irrespective of the system size, and, building upon the results of the noisy gates approach, provides a more accurate perturbative approximation of the open system evolution. This is contrast with other

proposals in the literature for algorithms that simulate open systems which present an ancilla overhead dependent on the system size and less accurate approximate solutions of the system evolution. These two aspects imply a substantial reduction of both width and depth of the resulting circuit.

Finally, the thesis presents an example of characterization of fundamental noises on superconducting transmon qubits. Specifically, the effects of the Continuous Spontaneous Localization (CSL) model are derived. CSL is a formulation of quantum mechanics that introduces a classical noise field that collapse superpositions of macroscopic objects. The direct effect of CSL of reducing superpositions of a transmon qubit is found to be negligible, while its indirect manifestation as dissipation-induced decoherence through superconducting excited states generation is stronger but still not the leading contribution to the excess of excited states detected with experiments on superconducting devices.

The thesis is organized as follows. In Chapter 2 we briefly introduce the formalism of open quantum systems. In Chapters 3 and 4 we present different methods for simulating noisy quantum circuits and we derive the generic expression of noisy gates. Then in Chapter 5 the noisy gates approach is specified to superconducting devices, and its superiority against standard method is thoroughly analysed. Chapter 6 presents the extension of the approach to integrated optical devices in the second quantization formalism. The application of the quantum noisy gates to devise a quantum algorithm to simulate open quantum systems is presented in Chapter 7. Chapter 8 estimates the impact of CSL on transmon qubits. We summarize the main results of the thesis in the conclusions in Chapter 9.

The research presented in this thesis has resulted in the following publications:

1. **Publication I**. M. Vischi, L. Ferialdi, A. Trombettoni and A. Bassi. Possible limits on superconducting quantum computers from spontaneous wave-function collapse models. Phys. Rev. B 106, 174506, 2022.

2. **Publication II**. G. Di Bartolomeo, M. Vischi, F. Cesa, R. Wixinger, M. Grossi, S. Donadi and A. Bassi. Noisy gates for simulating quantum computers. Phys. Rev. Research 5, 043210, 2023.

3. **Preprint I**. M. Vischi, G. Di Bartolomeo, M. Proietti, S. Koudia, F. Cerocchi, M. Dispenza and A. Bassi. Simulating photonic devices with noisy optical elements. arXiv:2311.10613 [quant-ph].

4. **Preprint II**. G. Di Bartolomeo, M. Vischi, T. Feri, A. Bassi and S. Donadi. Efficient quantum algorithm to simulate open systems through the quantum noise formalism. arXiv:2311.10009 [quant-ph].

Chapter 2

Noises in quantum computing devices

The goal of this chapter is to introduce the basics of open quantum systems. We show how the evolution of open systems is generally described through the operator sum representation or, when this is possible, through the Lindblad master equation. These represent the basic tools that are used throughout the rest of the thesis. The presentation is based on references [1, 2].

2.1 The theory of open quantum systems

The effects of noises affecting quantum computing devices are usually described by the theory of open quantum systems [1, 2] where the system of interest interacts with an external environment. This description is suitable to assess the effects of noises on quantum computation at many levels. At the physical level, each qubit experiences decoherence, the loss of its quantum information, because of its interaction with the environment. This corrupts the outcomes of a quantum algorithm: a quantum circuit is composed by many gates that are realized via time evolution of specific engineered Hamiltonians, and decoherence of qubits modifies such ideal evolution, eventually corrupting the final results of a circuit. We start by briefly reviewing the basics of open quantum systems.

2.1.1 Quantum operations and the operator sum representation

The evolution of an open quantum system is usually regarded as the effective result of the interaction between the system of interest in contact with an environment. The

system and the environment together form a closed quantum system, thus one usually assumes that the full dynamics of system plus environment is unitary. However, when tracing out the degrees of freedom of the environment, the effective evolution of the system alone generally looses unitarity. Assuming the system-environment input state is a product state $\hat{\rho} \otimes \hat{\rho}_{\text{env}}$, the reduced state of the system after the total unitary interaction $\hat{U}$ is

$$\mathcal{E}(\hat{\rho}) = \text{Tr}_{\text{env}}\left[\hat{U}(\hat{\rho} \otimes \hat{\rho}_{\text{env}})\hat{U}^\dagger\right], \tag{2.1}$$

where Tr_{env} is the partial trace over the environment. The map $\mathcal{E}(\cdot)$ in Eq. (2.1) describes the evolution of the system and as such it can be expressed in terms of operators of the system Hilbert space alone. This constitutes the operator sum representation of the map $\mathcal{E}(\cdot)$. We assume, without loss of generality, that the initial state of the environment is a pure state $\hat{\rho}_{\text{env}} = |e_0\rangle\langle e_0|$, where $|e_k\rangle$ is an orthonormal basis for the environment. Then, Eq. (2.1) can be expressed as

$$\mathcal{E}(\hat{\rho}) = \sum_i \langle e_i| \hat{U}(\hat{\rho} \otimes |e_0\rangle\langle e_0|)\hat{U}^\dagger |e_i\rangle \tag{2.2}$$

$$\mathcal{E}(\hat{\rho}) = \sum_i \hat{K}_i \hat{\rho} \hat{K}_i^\dagger\,, \tag{2.3}$$

where $\hat{K}_i := \langle e_i| \hat{U} |e_0\rangle$ are operators acting on the system alone, called operation elements. Eq. (2.3) is the operator sum representation of $\mathcal{E}(\cdot)$. The operation elements satisfy the completeness relation

$$\text{Tr}[\mathcal{E}(\hat{\rho})] = \text{Tr}\left(\sum_i \hat{K}_i \hat{\rho} \hat{K}_i^\dagger\right) = \text{Tr}\left(\sum_i \hat{K}_i^\dagger \hat{K}_i \hat{\rho}\right) = 1\,, \tag{2.4}$$

where we used the ciclicity of the trace. Since this equality holds for any density matrix $\hat{\rho}$, this implies that

$$\sum_i \hat{K}_i^\dagger \hat{K}_i = \mathbb{1}\,. \tag{2.5}$$

The completeness relation, which is valid for trace-preserving quantum operations, can be relaxed to include non-trace preserving quantum operations for which it takes the expression $\sum_i \hat{K}_i^\dagger \hat{K}_i \leq \mathbb{1}$, taking into account further leakage of information after measurements. When the quantum operation is trace preserving is also called a Kraus map, and the operation elements are called Kraus operators.

2.1.2 The Lindblad master equation

The operator sum representation is very effective in providing a general description of the evolution of density matrices, including evolution of pure states into mixed

states. It is often possible to describe the evolution of a density matrix by a differential equation called master equation, that captures infinitesimal changes in the density matrix. In general, a master equation has a closed form only when the evolution of the system is Markovian, meaning that it is local in time. A closed form for the master equation is not suitable in the general case because of flow of information from the system to the environment and viceversa, which embody non-Markovian effects. This means that $\hat{\rho}(t+\mathrm{d}t)$ depends not only on $\hat{\rho}(t)$ but also on $\hat{\rho}$ at any earlier time, as the environment could retain past information of the system and put it back in it: this flow of information results in non-Markovian fluctuations of the system.

The idea behind a Markovian description is that there is a sharp division between the typical correlation time of the fluctuations and the time scale of the system evolution. We denote with Δt_{env} the time it takes for the environment to lose information acquired from the system and with $\Delta t_{\mathrm{coarse}}$ a coarse graining in time as if we perceive the dynamics through a filter that screens out the high frequency components of the motion, with $\omega \ll \Delta t_{\mathrm{coarse}}^{-1}$. A Markovian description is possible if $\Delta t_{\mathrm{env}} \ll \Delta t_{\mathrm{coarse}}$, meaning that we can neglect memory effects of the environment because the coarse graining is not able to resolve them. The Markovian approximation is useful when the time scale of the desired dynamics Δt_{damp} is long compared to $\Delta t_{\mathrm{coarse}}$

$$\Delta t_{\mathrm{damp}} \gg \Delta t_{\mathrm{coarse}} \gg \Delta t_{\mathrm{env}} \,. \tag{2.6}$$

Now suppose that the Markovian approximation applies and the initial state of the system is $\hat{\rho}(0)$. Then a general trace preserving quantum operation has Kraus representation

$$\hat{\rho}(t) = \mathcal{E}_t(\hat{\rho}(0)) = \sum_i \hat{K}_i(t)\hat{\rho}(0)\hat{K}_i^\dagger(t) \,, \tag{2.7}$$

with $\mathcal{E}_0 = \mathbb{1}$. After an infinitesimal time interval $\mathrm{d}t$ one has that

$$\hat{\rho}(\mathrm{d}t) = \hat{\rho}(0) + \mathcal{O}(\mathrm{d}t) \,, \tag{2.8}$$

implying that one of the Kraus operators is $\hat{K}_0 = \mathbb{1} + \mathcal{O}(\mathrm{d}t)$ and all the others $\hat{K}_i$ with $i > 0$ describe the quantum jumps that the system might undergo each occurring with a probability of order $\mathrm{d}t$, and being themselves of order $\sqrt{\mathrm{d}t}$. Thus we can write

$$\hat{K}_0 = \mathbb{1} + (-i\hat{H} + \hat{M})\mathrm{d}t \qquad\qquad \hat{K}_i = \sqrt{\gamma_i \mathrm{d}t}\hat{L}_i \,, \tag{2.9}$$

where γ_i are frequency factors, $\hat{H}$ and $\hat{M}$ are Hermitian and $\hat{L}_i$, $\hat{H}$ and $\hat{M}$ are all zeroth order in $\mathrm{d}t$. $\hat{M}$ is determined by the normalization condition

$$\mathbb{1} = \sum_i \hat{K}_i^\dagger \hat{K}_i = \mathbb{1} + \mathrm{d}t(2\hat{M} + \sum_{i>0} \gamma_i \hat{L}_i^\dagger \hat{L}_i) \,, \tag{2.10}$$

leading to

$$\hat{M} = -\frac{1}{2}\sum_{i>0}\gamma_i \hat{L}_i^\dagger \hat{L}_i \,. \tag{2.11}$$

Substituting $\hat{M}$ into Eq. (2.7), expressing $\hat{\rho}(\mathrm{d}t) = \hat{\rho}(0) + \mathrm{d}t\dot{\hat{\rho}}(0)$ and equating terms of order $\mathrm{d}t$ one obtains the Lindblad master equation [3, 4]

$$\frac{\mathrm{d}}{\mathrm{d}t}\hat{\rho}_t = -\frac{i}{\hbar}[\hat{H}_t, \hat{\rho}_t] + \sum_k \gamma_k \left[\hat{L}_k \hat{\rho}_t \hat{L^\dagger}_k - \frac{1}{2}\{\hat{L^\dagger}_k \hat{L}_k, \hat{\rho}_t\}\right]; \tag{2.12}$$

the first term is the free term generating the unitary evolution of the system, the other terms describe possible transitions of the system due to interactions with the environment. $\hat{L}_k$ are called Lindblad operators. One usually expresses the Lindblad terms as a superoperator, acting on density matrices, such that $\mathcal{L}_D[\hat{\rho}_t] = \sum_k \gamma_k(\hat{L}_k\hat{\rho}_t\hat{L}_k^\dagger - \frac{1}{2}\{\hat{L}_k^\dagger\hat{L}_k, \hat{\rho}_t\})$.

Now consider the Lindblad equation Eq. (2.12). Moving to the interaction picture by defining $\hat{\chi}_t = \hat{U}^\dagger(t, t_0)\hat{\rho}_t\hat{U}(t, t_0)$ and $\hat{\chi}_{t_0} = \hat{\rho}_{t_0}$, leads to

$$\frac{\mathrm{d}}{\mathrm{d}t}\chi_t = \mathcal{L}_D(t)[\chi_t] \,, \tag{2.13}$$

where $\mathcal{L}_D(t)[\hat{\chi}_t] = \hat{U}^\dagger(t, t_0)\mathcal{L}_D[\hat{\rho}_t]\hat{U}(t, t_0)$. The formal solution of Eq. (2.13) is

$$\hat{\chi}_t = \mathcal{T}\left[e^{\int_{t_0}^t \mathrm{d}s\mathcal{L}_D(s)}\right]\hat{\chi}_{t_0} \,, \tag{2.14}$$

where $\mathcal{T}[\cdot]$ is the time ordering. Thus in the Schrödinger picture we can write the formal solution of Eq. (2.12) as

$$\hat{\rho}_t = \hat{U}(t, t_0)\mathrm{T}\left[e^{\int_{t_0}^t \mathrm{d}s\mathcal{L}_D(s)}\right]\hat{\rho}_{t_0}\hat{U}^\dagger(t, t_0) \,. \tag{2.15}$$

This formal expression captures, within the limits of validity of Lindblad's equation, the entire physics occurring during the open system's evolution.

2.2 Discussion

The theory of open quantum systems has a broad applicability in the study of noises in quantum computing. It allows to understand the effects of noises to help suggesting hardware improvements or novel error mitigation strategies. From this point of view, there are two main objectives of applying the theory of open quantum

systems to quantum computing: characterize and model the noises acting on quantum devices and, secondly, have good simulation tools allowing to simulate as accurately as possible the effects of a given noise model on quantum circuits and algorithms. In the next chapter we discuss different strategies to reach the second objective, that are different ways to derive approximate solution of the Lindblad equation in Eq. (2.15) by means of specific algorithmic approaches. We leave the discussion on noise characterization for Chapter 8, where we investigate the effects of fundamental noise sources on superconducting devices.

Chapter 3

Simulation of noisy quantum circuits

In this chapter we present different algorithmic approaches for simulating the effects of noises in quantum circuits. We argue that to reach a good accuracy a simulation method should substitute each ideal gate with a noisy gate, an expression taking into account the unitary and the noise evolution all together. We further show that when it is possible to derive an approximate noisy gate expression, the best option at the algorithmic level is to unravel the Lindblad equations in terms of diffusive stochastic Schrödinger equations.

3.1 From noise gate to noisy gates

The primary goal of a software simulator of noisy quantum circuit is to have the most accurate results possible. This means that given a quantum circuit and an underlying noise model of the device, that essentially specify a Lindblad equation (or, more generally a quantum operation), we are interested in the most accurate way to simulate the evolution dictated by such an equation, which is a complex computational task.

The problem can be simplified by exploiting the structure of the quantum circuit which consists of a sequence of gates. Setting the initial density matrix and considering the first gate in the circuit, one has to solve the corresponding Lindblad equation, which is generally acting on a small subset of all qubits. The output density matrix is the input to the second gate whose Lindblad equation has to be solved to get the output density matrix and so on until the final density matrix is obtained. However, exact analytic solutions of the gates' Lindblad equations are not available. The brute force approach of solving numerically for the gates' Lindblad equations requires nu-

merical efforts while other techniques such as quantum process tomography [2] that reconstructs the full quantum operations of gates, involves the run of actual experiments. This could and should be avoided when analytic approximate expressions for the solutions of gates' Lindblad equations are available.

It is possible to resort to analytic and approximate expressions based on reasonable physical assumptions. Indeed, for most current noisy devices, characteristic times of the noises are usually very large with respect to the time needed to realize a gate, meaning that the effective dynamics of the system during the gate time can reasonably assumed to be the ideal one with a small perturbation provided by the noises. For instance, in IBM's superconducting devices [5], the gate time is $t_g \sim 10^{-8}s$, while typical environmental effects have characteristic times of order $T_1, T_2 \sim 10^{-4}s$.

Based on this observation, the standard assumption is that in this regime it is allowed to completely decouple the noise evolution from the ideal one. Thus, the simulation of noisy gate-based quantum circuits is mostly implemented by adding appropriate quantum operations, referred here as *noise gates*, before and after each ideal gate [1,2,6]: schematically if an ideal (unitary) gate G is supposed to be executed, the noises affecting it are modeled by adding appropriate operations $\mathcal{E}_1$ ($\mathcal{E}_2$) mimicking the noise, before (after) the gate

$$\hat{\rho} \;\text{—}\boxed{\mathcal{E}_1}\text{—}\boxed{G}\text{—}\boxed{\mathcal{E}_2}\text{—}\; \hat{\rho}' \;\;, \tag{3.1}$$

where neither $\mathcal{E}_1$ nor $\mathcal{E}_2$ have any dependence on the gate G or viceversa. More specifically, the standard assumption translates to assuming in Eq. (2.15) that

$$\mathcal{L}_D(t) \simeq \mathcal{L}_D \,, \tag{3.2}$$

thus getting

$$\hat{\rho}_t \simeq \hat{U}(t, t_0) e^{\mathcal{L}_D (t-t_0)} \hat{\rho}_{t_0} \hat{U}^\dagger(t, t_0) \,. \tag{3.3}$$

The noise term $e^{\mathcal{L}_D(t-t_0)}$ is independent from the unitary evolution $\hat{U}(t, t_0)$ and viceversa. This reduces the problem to solving the Lindblad equation in Eq. (2.12) for each gate without the Hamiltonian term to get $e^{\mathcal{L}_D(t-t_0)}$, or if this is already known, as it usually happens, to apply $e^{\mathcal{L}_D \cdot (t-t_0)}$ as a quantum operation, that constitutes a noise gate.

This standard approach has some limitations. During a quantum circuit the controlled action generating the gate and the environment act simultaneously and potentially affect each other. Moreover current gate and noise characteristic times do not completely justify a formal decoupling of the noise and gate dynamics. In this scenario, neglecting this interplay leads to inaccurate predictions, especially when the number of gates and qubits increases, approaching the regime where simulations are more interesting.

An alternative and more accurate approach should not involve a noise gate but rather a *noisy gate* expression where the noise is integrated into the gates, in the sense that the resulting noisy gate is computed by solving for the dynamics generating it, with additional terms describing the noise added to it, schematically

$$\hat{\rho} \text{ —} \boxed{\mathcal{G}} \text{— } \hat{\rho}' \ , \tag{3.4}$$

where in general $\mathcal{G} \neq \mathcal{E}_2 \circ G \circ \mathcal{E}_1$. This task is obviously achieved by solving the full Lindblad master equation for each gate to get Eq. (2.15) or to know its operator sum representation. However, as already pointed out, the gate's Lindblad equations are not solvable exactly and without such solutions it is not easy to know in advance the operator sum representation of a noisy gate, as it is not clear how the ideal gate evolution and the noise one will contribute together in the resulting full map in Eq. (2.15). As we show in Chapter 4, it is possible to get an analytic expression $\mathcal{G}$ for the solution of the Lindblad equation with perturbative (in the noise parameters) methods. In particular we devise a noisy gate approach that corresponds to a first order approximation in Eq. (2.15)

$$\mathrm{T}\left[e^{\int_{t_0}^{t} \mathrm{d}s \mathcal{L}_D(s)}\right] \simeq \mathbb{1} + \int_{t_0}^{t} \mathrm{d}s \mathcal{L}_D(s)\,, \tag{3.5}$$

such that

$$\hat{\rho}_t \simeq \hat{U}(t,t_0)\left(\mathbb{1} + \int_{t_0}^{t} \mathrm{d}s \mathcal{L}_D(s)\right)\hat{\rho}_{t_0}\hat{U}^\dagger(t,t_0)\,. \tag{3.6}$$

In Eq. (3.6) the noise depends on the Hamiltonian dynamics through $\mathcal{L}_D(s) = \hat{U}^\dagger(t,t_0)\mathcal{L}_D\hat{U}(t,t_0)$. Notably, this expression contains more terms to first order in the noise parameters than those included in Eq. (3.3) and since the first order is the leading one, such method is expected to offer a more accurate description of each gate evolution and therefore a better protocol for circuit simulations.

Both the standard approach and the noisy gate approach formulated in terms of density matrices, face a computational limitation. Even though Eqs. (3.3) and (3.6) are usually computed for single and two qubit gates, their results have to be composed to get, eventually, the full density matrix of the circuit. This scales quadratically with the number of qubits, as for N qubits the dimension of the density matrix is 2^{2N}.

It is possible to employ stochastic descriptions, statistically equivalent to the density matrix formalism, that evolve state vectors whose dimension for N qubits is 2^N, thus providing a quadratic speedup. However, a stochastic description involves an average over multiple realizations, i.e. a sampling overhead. The advantage is that such overhead does not depend in general on N and thus stochastic state vector descriptions are still preferable from the computational point of view.

In the following, we recap the main stochastic state vector approaches and their algorithmic implementations, highlighting when these allow for expressions in which gates and noise dynamics affect each other. We further report their performances in terms of both accuracy in reproducing the Lindblad equation and computational costs. We already mention that the most favourable option to reproduce the approximate solution in Eq. (3.6) is the noisy gate approach presented in this thesis, based on the unraveling in terms of stochastic Schrödinger equation.

3.1.1 Unraveling of quantum operation

Most of the relevant quantum computing frameworks implement a noisy simulation approach based on the so called stochastic unraveling of Kraus maps. A generic Kraus map reads

$$\mathcal{E}(\hat{\rho}) = \sum_{i}^{m} \hat{K}_i \hat{\rho} \hat{K}_i^\dagger \,, \tag{3.7}$$

where $\sum_i^m \hat{K}_i^\dagger \hat{K}_i = \mathbb{1}$ and m is the total number of Kraus operators. Suppose that the state of the system is initially in a pure state $|\psi\rangle$. The map is unraveled to a stochastic map on state vectors by imposing that, at a given time, $|\psi\rangle$ changes randomly as follows

$$|\psi'\rangle = \frac{1}{\sqrt{p_j}} \hat{K}_j |\psi\rangle \,, \tag{3.8}$$

with probability

$$p_j = |\langle\psi| \hat{K}_j^\dagger \hat{K}_j |\psi\rangle|^2 \,. \tag{3.9}$$

The p_j are probabilities as the normalization condition $\sum_i^m \hat{K}_i^\dagger \hat{K}_i = \mathbb{1}$ ensures their values ranges between zero and one and that they sum up to one. In the limit of a large number of realizations N_s, the average density matrix is given by

$$\hat{\rho} = \frac{1}{N_s} \sum_{n=1}^{N_s} |\psi_i'\rangle \langle\psi_i'| \tag{3.10}$$

$$= \frac{1}{N_s} \sum_{n=1}^{N_s} p_{j_n}^{-1} \hat{K}_{j_n} |\psi\rangle \langle\psi| \hat{K}_{j_n}^\dagger \,, \tag{3.11}$$

where $\hat{K}_{j_n}$ is the randomly picked Kraus operator in the n-th trial. This channel, which is itself a Kraus map, can be rewritten by grouping terms involving the same Kraus operators as

$$\hat{\rho} = \sum_{i=1}^{m} \frac{N_i}{N_s} p_i^{-1} \hat{K}_i |\psi\rangle \langle\psi| \hat{K}_i^\dagger \,, \tag{3.12}$$

where N_i is the total number of times the Kraus operator $\hat{K}_i$ is randomly selected. This number in the limit of large N_s can be approximated as $N_i \approx N_s p_i$, leading to

$$\hat{\rho} \approx \sum_{i=1}^{m} \hat{K}_i \left|\psi\right\rangle \left\langle\psi\right| \hat{K}_i^\dagger \,, \tag{3.13}$$

recovering the original Kraus map. We report in Alg. 1 the pseudo code associated to the unraveling of Kraus maps.

Algorithm 1 KRAUS MAP SIMULATION

Input: Initial state $|\psi_0\rangle$, a noiseless circuit $\hat{C} = \{\hat{U}^{(1)}, ..., \hat{U}^{(n_g)}\}$ composed by n_g gates $\hat{U}^{(i)}$ and number of samples N_s

for $0 \leq k \leq N_s$ **do**

  while $1 \leq i \leq n_g$ **do**

    compute $|\psi_k\rangle^{(i)} = \hat{U}^{(i)} |\psi_k\rangle^{(i-1)}$

    compute $p_j = |\langle\psi_k|^{(i)} \hat{K}_j^\dagger \hat{K}_j |\psi_k\rangle^{(i)}|^2$

    sample $\hat{K}_j$ operator from $\{p_j\}$

    update the state to $|\psi_k\rangle^{(i)} = \frac{1}{\sqrt{p_j}} \hat{K}_j |\psi_k\rangle^{(i)}$

  end

  compute $\hat{\rho}_k = |\psi_k\rangle^{(n_g)} \langle\psi_k|^{(n_g)}$

end

Output: $\hat{\rho}_f = \frac{1}{N_s} \sum_{k=1}^{N_s} \hat{\rho}_k$

The time complexity of Alg. 1 is primarily determined by the matrix vector multiplication step, exhibiting a complexity of $\mathcal{O}(2^{2n})$, where n is the number of qubits. The space complexity is dominated by the storage of the state vector and it scales as $\mathcal{O}(2^n)$. It has to be noted that when the Kraus operators are not unitary one needs to store the intermediate state vectors, which are necessary in order to compute the probabilities in Eq. (3.9). This operation has the same time and space complexity as those of the the previous step but introduces further computational costs. The computation of probabilities can be avoided only for mixed unitary error channels, for which all Kraus operators are unitary. In this case probabilities are known and independent of the current state.

Alg. 1 works for any noise channel that admits a Kraus representation meaning that this approach allows for a noisy gates description. This, however, requires the knowledge of the full gate plus noise Kraus map. As previously suggested, one option is to perform quantum process tomography and then use algorithm Alg. 1. This

not only scales bad as for each one-qubit gate and for each two-qubit gate one must estimate 12 and 240 parameters respectively [2], but also requires the characterization of such parameters via experiment. Another option is to derive the approximate solutions of the Lindblad equations of each gate as in Eq. (3.6), express them as a Kraus maps, and then use algorithm Alg. 1. This reproduces the desired system dynamics but it involves, in general, the additional computational cost of recovering the probabilities in Eq. (3.9).

3.1.2 Unraveling of master equation in terms of random quantum jumps

Another commonly used state vector stochastic method is the so called random quantum jump approach. The Lindblad master equation in Eq. (2.12) can be equivalently written as

$$\frac{\mathrm{d}}{\mathrm{d}t}\hat{\rho}_t = -\frac{i}{\hbar}[\hat{H}_t, \hat{\rho}_t] + \sum_k \gamma_k \left[\hat{L}_k \hat{\rho}_t \hat{L}^\dagger{}_k - \frac{1}{2}\{\hat{L}^\dagger{}_k \hat{L}_k, \hat{\rho}_t\}\right] \tag{3.14}$$

$$= -\frac{i}{\hbar}[\hat{H}_{\text{eff}}, \hat{\rho}_t] + \sum_k \gamma_k \hat{L}_k \hat{\rho}_t \hat{L}^\dagger{}_k \,, \tag{3.15}$$

where the Hamiltonian term and the anticommutator term are grouped together leading to an evolution under an effective non-Hermitian operator

$$\hat{H}_{\text{eff}} = \hat{H}_t - i\hbar \sum_k \frac{\gamma_k}{2} \hat{L}^\dagger{}_k \hat{L}_k \,, \tag{3.16}$$

plus an additional term $\sum_k \gamma_k \hat{L}_k \hat{\rho}_t \hat{L}^\dagger{}_k$ responsible for quantum jumps. In this context the Lindblad operators are also called jump operators.

Given a system initially in a pure state $\hat{\rho}(t_0) = |\psi(t_0)\rangle \langle\psi(t_0)|$, after a small time $\mathrm{d}t$ the density matrix evolves to

$$\hat{\rho}(t_0 + dt) = \left(1 - \sum_k \mathrm{d}p_k\right) |\psi_0\rangle \langle\psi_0| + \sum_k \mathrm{d}p_k \, |\psi_k\rangle \langle\psi_k| \,, \tag{3.17}$$

where $\mathrm{d}p_k$ are probabilities and they are defined by

$$\mathrm{d}p_k = \gamma_k \langle\psi(t_0)| \hat{L}^\dagger{}_k \hat{L}_k |\psi(t_0)\rangle \mathrm{d}t \,. \tag{3.18}$$

These probabilities are infinitesimal as they depend on $\mathrm{d}t$. The new states appearing

in Eq. (3.17) are

$$|\psi_0\rangle = \frac{1}{\sqrt{1-\sum_k \mathrm{d}p_k}}(\mathbb{1} - \frac{i}{\hbar}\hat{H}_{\text{eff}}\mathrm{d}t)\,|\psi(t_0)\rangle \tag{3.19}$$

$$|\psi_k\rangle = \frac{1}{||\hat{L}_k\,|\psi(t_0)\rangle\,||}\hat{L}_k\,|\psi(t_0)\rangle\ , \tag{3.20}$$

with the following interpretation: after a time $\mathrm{d}t$, with probability $\mathrm{d}p_k$ the state of the system jumps to $|\psi_k\rangle$, a state associated to the jump operator $\hat{L}_k$. With probability $1-\sum_k \mathrm{d}p_k$ no jump occurs and the system evolves to $|\psi_0\rangle$ according to the effective operator $\hat{H}_{\text{eff}}$. Since in both cases the evolution is not unitary, the state in Eq. (3.19) has to be normalized.

The algorithmic implementation of the quantum jumps dynamics relies on the so-called Monte Carlo wave function approach [7]. Suppose we want to simulate the evolution of the open system in the time interval $[t_0, t_g]$ needed to execute a gate. Let the initial state of the system be the pure state $|\psi(t_0)\rangle$ and choose a time step $\mathrm{d}t$ smaller than the time scales relevant for the evolution of the system in the interval $[t_0, t_g]$. At each time step $\mathrm{d}t$, sample a random number ϵ from a uniform distribution in the unit interval $[0, 1]$. If $\epsilon < \sum_k \mathrm{d}p_k$, the system jumps to one of the state $|\psi_k\rangle$. In particular to $|\psi_1\rangle$ if $0 < \epsilon < \mathrm{d}p_1$, to $|\psi_2\rangle$ if $\mathrm{d}p_1 < \epsilon < \mathrm{d}p_1 + \mathrm{d}p_2$ and so on. On the other hand if $\epsilon > \sum_k \mathrm{d}p_k$, the state evolve to $|\psi_0\rangle$ via the effective evolution operator. We repeat the sampling for each $\mathrm{d}t$. This constitutes a realization in terms of quantum trajectories. The associated pseudo code is reported in Alg. 2.

Algorithm 2 RANDOM QUANTUM JUMP SIMULATION

Input: Initial state $|\psi_0\rangle$, a noiseless circuit $\mathrm{C} = \{\hat{U}^{(1)}, ..., \hat{U}^{(n_g)}\}$ composed by n_g gates $\hat{U}^{(i)}$, time step $\mathrm{d}t$ and number of samples N_s

for $0 \leq k \leq N_s$ **do**
  while $1 \leq i \leq n_g$ **do**
    while $dt \leq j \;\; dt \leq t_g$ **do**
      compute $\mathrm{d}p_l^{(i,j)} = \gamma_l^{(i)} \langle\psi_k((j-1)\mathrm{d}t)|^{(i)} \hat{L}_l^{(i)\dagger} \hat{L}_l^{(i)} |\psi_k((j-1)\mathrm{d}t)\rangle^{(i)} \mathrm{d}t$;
      sample a random number $0 < \epsilon < 1$;
      if $0 < \epsilon < dp_1^{(i,j)}$ **then**
        update the state to
        $|\psi_k(j\mathrm{d}t)\rangle^{(i)} = \frac{1}{||\hat{L}_1^{(i)}|\psi_k((j-1)\mathrm{d}t)\rangle^{(i)}||} \hat{L}_1^{(i)} |\psi_k((j-1)\mathrm{d}t)\rangle^{(i)}$
      else if $dp_1^{(i,j)} < \epsilon < dp_1^{(i,j)} + dp_2^{(i,j)}$ **then**
        update the state to
        $|\psi_k(j\mathrm{d}t)\rangle^{(i)} = \frac{1}{||\hat{L}_2^{(i)}|\psi_k((j-1)\mathrm{d}t)\rangle^{(i)}||} \hat{L}_2^{(i)} |\psi_k((j-1)\mathrm{d}t)\rangle^{(i)}$
      $\vdots$
      else
        update the state to
        $|\psi_k(j\mathrm{d}t)\rangle^{(i)} = \frac{1}{\sqrt{1-\sum_l \mathrm{d}p_l^{(i,j)}}} (\mathbb{1} - \frac{i}{\hbar} \hat{H}_{\mathrm{eff}}^{(i)} \mathrm{d}t) |\psi_k((j-1)\mathrm{d}t)\rangle^{(i)}$
      end
    end
  end
  compute $\hat{\rho}_k = |\psi_k\rangle^{(n_g)} \langle\psi_k|^{(n_g)}$
end

Output: $\hat{\rho}_f = \frac{1}{N_s} \sum_{k=1}^{N_s} \hat{\rho}_k$

We mention that the evolution of the state vector is formalized by means of a non linear stochastic Schrödinger equation of the form

$$\begin{aligned} \mathrm{d}|\psi_t\rangle = \Bigg[& -i\hat{H} - \sum_k \frac{\gamma_k}{2} (\hat{L}_k^\dagger \hat{L}_k - \langle\psi_t| \hat{L}_k^\dagger \hat{L}_k |\psi_t\rangle) \mathrm{d}t \\ & + \sum_k \left(\frac{1}{\sqrt{\langle\psi_t| \hat{L}_k^\dagger \hat{L}_k |\psi_t\rangle}} \hat{L}_k - \mathbb{1} \right) \mathrm{d}N_k \Bigg] |\psi_t\rangle \;, \end{aligned} \tag{3.21}$$

where $\mathrm{d}N_k$ are Poisson increments, that satisfy $\mathrm{d}N_i \mathrm{d}N_j = \delta_{ij} \mathrm{d}N_j$ and $\mathbb{E}[\mathrm{d}N_k] = \gamma_k \langle\psi_t| \hat{L}_k^\dagger \hat{L}_k |\psi_t\rangle \mathrm{d}t$. Thus, the probability that the variable $\mathrm{d}N_k$ is 1 during the given

time step $\mathrm{d}t$ is $\gamma_k \langle\psi_t| \hat{L}_k^\dagger \hat{L}_k |\psi_t\rangle \mathrm{d}t$, showing a direct dependence on the state vector. For most of the time the variables $\mathrm{d}N_k$ are zero, and the system evolves continuously by means of the non-Hermitian effective operator. When a variable $\mathrm{d}N_k$ is 1 a quantum jump occurs.

The time and space complexities of Alg. 2 are the same as those for Alg. 1, respectively $\mathcal{O}(2^{2n})$, where n is the number of qubits, and $\mathcal{O}(2^n)$. Similarly to the unraveling of Kraus maps, the state of the system must be stored in order to compute the probabilities in Eq. (3.18) and the normalization factors in Eq. (3.19) and Eq. (3.20). This is an effect of the non linearity of the method that increases its computational cost. Notably, the quantum jump approach provides, in the limit of a large number of realization N_s and small $\mathrm{d}t$, a solution to the full Lindblad equation, as in Eq. (2.15), allowing for a very accurate noisy gate description. However this can be achieved only by dividing the time interval of a given gate into small time steps $\mathrm{d}t$, increasing the number of total matrix vector multiplications. This becomes inefficient and therefore analytic and approximate expressions for the whole gate time are preferable.

3.1.3 Unraveling of master equation in terms of Stochastic Schrödinger equation

The stochastic Schrödinger equation in Eq. (3.21) is one of the many equivalent unravelings of the Lindblad equation in terms of stochastic Schrödinger equations. Among them there is always one which is linear [8–12]

$$\mathrm{d}|\psi_t\rangle = \left[-\frac{i}{\hbar}\hat{H}_t \mathrm{d}t + \sum_k \left(i\sqrt{\gamma_k}\hat{L}_k \mathrm{dW}_k(t) - \frac{\gamma_k}{2}\hat{L^\dagger}_k \hat{L}_k \mathrm{d}t \right) \right] |\psi_t\rangle \ , \tag{3.22}$$

where the $\mathrm{dW}_k(t)$ are Wiener increments with means zero $\mathbb{E}[\mathrm{dW}_i(t)] = 0$ and correlations $\mathbb{E}[\mathrm{dW}_i(t),\mathrm{dW}_j(t)] = \delta_{ij}\mathrm{d}t$. Eq. (3.22) is a stochastic Itô equation. We notice its similarity with Eq. (3.21), but in this case Wiener increments are continuous and diffusive and not discrete and jump-like as Poissonian increments.

The distinctive feature of Eq. (3.22) is linearity: given the state at time $|\psi_{t_0}\rangle$, the state at a later time is expressed as

$$|\psi_t\rangle = \hat{N}_g(t, t_0) |\psi_{t_0}\rangle \ , \tag{3.23}$$

where $\hat{N}_g(t, t_0)$ is a linear matrix which constitutes a stochastic noisy gate. For this reason, from now on we will call this approach the noisy gates approach. $\hat{N}_g(t, t_0)$ is not unitary in general. Indeed Eq. (3.22) does not preserve the norm of the state

vector in a single trajectory; the variation of the norm is given by

$$\mathrm{d}\||\psi_t\rangle\|^2 = \langle \mathrm{d}\psi_t|\psi_t\rangle + \langle \psi_t|\mathrm{d}\psi_t\rangle + \langle \mathrm{d}\psi_t|\mathrm{d}\psi_t\rangle = -i\sum_k \langle\psi_t|\,\hat{L^\dagger}_k - \hat{L}_k\,|\psi_t\rangle \mathrm{dW}_k(t)\,, \tag{3.24}$$

which is zero only if $\hat{L^\dagger}_k = \hat{L}_k$ for each k, i.e. only if each Lindblad operator is Hermitian. We notice that according to the rules of Itô calculus, terms like $\langle \mathrm{d}\psi_t|\mathrm{d}\psi_t\rangle$ must be taken into account because squared Wiener increments contribute to order $\mathrm{d}t$. Non preservation of the norm is a consequence of the chosen unraveling: one could have chosen norm-preserving unravelings [13, 14] (involving Wiener increments but similar to Eq. (3.21)), which however are not linear and therefore do not allow for a gate-like formulation. The lack of norm preservation is not a problem since at the statistical level, i.e. when the average over the noise is taken, one recovers the Lindblad equation, which is trace preserving. Given

$$\hat{\rho}_t = \mathbb{E}\Big[\,|\psi_t\rangle\,\langle\psi_t|\,\Big]\,, \tag{3.25}$$

by resorting to the rules of Itô calculus, one can prove that

$$\begin{aligned}\mathrm{d}\hat{\rho}_t &= \mathbb{E}[\mathrm{d}|\psi_t\rangle\,\langle\psi_t|] = \mathbb{E}[\mathrm{d}|\psi_t\rangle\,\langle\psi_t|] + \mathbb{E}[|\psi_t\rangle\mathrm{d}\langle\psi_t|] + \mathbb{E}[\mathrm{d}|\psi_t\rangle\mathrm{d}\langle\psi_t|] \\ &= -\frac{i}{\hbar}[\hat{H}_t,\hat{\rho}_t]\mathrm{d}t + \sum_k \gamma_k\left[\hat{L}_k\hat{\rho}_t\hat{L^\dagger}_k\mathrm{d}t - \frac{1}{2}\{\hat{L^\dagger}_k\hat{L}_k,\hat{\rho}_t\}\mathrm{d}t\right],\end{aligned} \tag{3.26}$$

showing that the linear stochastic Schrödinger equation is statistically equivalent to the Lindblad equation.

Eq. (3.22) does not admit a solution in closed form, unless for special cases e.g. when the deterministic terms commute with the stochastic ones. However when $\gamma_k \ll \Omega$ where Ω is the characteristic frequency of the gate Hamiltonian, it is possible to use a perturbative approach to write an analytic expression over the entire gate time of the noisy gate, as in Eq. (3.23). This will be the subject of the next chapter. We notice the advantages of the noisy gates approach: on the one hand, linearity and the statistical equivalence allow to avoid the computation of any intermediate norm of the state vector, as in Eqs. (3.9) and (3.18), on the other hand it is not required to discretize the gate time in smaller time steps to maintain a good accuracy. The noisy gates approach does not present any additional time complexity other than the matrix vector multiplications, at the same time significantly reducing the total number of such multiplications.

The general procedure therefore is the following. Given a noiseless algorithm, the corresponding noisy one is obtained by replacing each ideal gate with a noisy

gate as in Eq. (3.23). The resulting noisy algorithm, which is stochastic, is repeated for different realizations of the random variables, as if they were different runs on a physical quantum computer. This produces a statistics of outcomes, to be compared with those of a real computer, or to be used to predict the behavior of a noisy device. We summarize the noisy gates simulation approach in Alg. 3.

Algorithm 3 NOISY GATES SIMULATION

Input: Initial state $|\psi_0\rangle$, a noiseless circuit $\hat{C} = \{\hat{U}^{(1)}, ..., \hat{U}^{(n_g)}\}$ composed by n_g gates $\hat{U}^{(i)}$ and number of samples N_s

for $0 \leq k \leq N_s$ **do**

map a noisy circuit $\hat{\tilde{C}} = \{\hat{N}^{(1)}, ..., \hat{N}^{(n_g)}\}$ on $\hat{C}$

sample stochastic processes W inside noisy gates $\hat{N}^{(i)}$

compute $|\psi_k\rangle = \hat{N}^{(n_g)} \dots \hat{N}^{(1)} |\psi_0\rangle$

compute $\rho_k = |\psi_k\rangle \langle\psi_k|$

end

Output: $\rho_f = \frac{1}{N_s} \sum_{k=1}^{N_s} \rho_k$

The time complexity of Alg. 3 is again $\mathcal{O}(2^{2n})$, determined by the matrix vector multiplication step. Analogously, the space complexity is $\mathcal{O}(2^n)$. We stress again that in Alg. 3 there is no need to perform the scalar product in Eq. (3.9) or Eq. (3.18). Moreover, all the optimizations to reduce the time complexity that are possible for Algs. 1 and 2 are also possible for Alg. 3. Finally, we show later that the sampling of random numbers has a constant scaling.

The unraveling in terms of a linear stochastic Schrödinger equation is the only one providing a noisy gate description, which is analytic in the gate time (but approximate) and being linear it avoids any norm computation of intermediate states. In this regard, it is the best approach to use, keeping in mind both accuracy in reproducing the system evolution and algorithmic complexity. Moreover the linear stochastic Schrödinger equations are very flexible. Indeed Markovianity, which is the main physical assumption behind the Lindblad equation, and it is a very convenient working hypothesis, can be released in favour of more general noises [1,10,15–18]. The advantage of using stochastic Schrödinger equations is that it is possible to describe a non-Markovian evolution of the state vector even when this does not correspond to a master equation for density matrices in closed form. The treatment of non-Markovian evolution is left for future research.

3.1.4 Unitary unraveling

The noisy gates in Eq. (3.23) are matrices which, in general, are not unitary, as the norm of state vectors is not preserved, see Eq. (3.24). It is possible to derive a unitary unraveling of the Lindblad equation, through the quantum noise formalism [12, 19] that essentially promotes classical Wiener processes to quantum Wiener processes. The quantum noise formalism arises by considering the system in contact with a reservoir of thermal baths. The system-environment Hamiltonian reads

$$\hat{H} = \hat{H} + \hat{H}_{\mathrm{E}} + \hat{H}_{\mathrm{SE}} \tag{3.27}$$

where $\hat{H}$ is the system Hamiltonian while $\hat{H}_{\mathrm{E}}$ and $\hat{H}_{\mathrm{SE}}$ are, respectively, the environment Hamiltonian and the system-environment interaction Hamiltonian

$$\hat{H}_{\mathrm{E}} = \hbar \sum_k \int \mathrm{d}\omega \omega \hat{b}_k^\dagger(\omega)\hat{b}_k(\omega), \tag{3.28}$$

$$\hat{H}_{\mathrm{SE}} = i\hbar \sum_k \int \mathrm{d}\omega \chi_k(\omega)\Big(\hat{b}_k^\dagger(\omega)\hat{L}_k - \hat{L}_k^\dagger \hat{b}_k(\omega)\Big), \tag{3.29}$$

where $\hat{b}_k(\omega)$ is the annihilation operator of the k-th thermal bath, ω is the frequency of the mode and $\hat{L}_k$ is an arbitrary system operator. Starting from the Hamiltonian in Eq. (3.27), one can solve the Heisenberg equation for $\hat{b}_k(\omega)$ and substitute the corresponding solution in the Heisenberg equation for an arbitrary system-environment operator $\hat{O}$. In the Markov approximation, namely when $\chi_k(\omega) = \sqrt{\gamma_k/(2\pi)}$, the Heisenberg equation for the operator $\hat{O}$ reads [19]

$$\begin{aligned} \frac{\mathrm{d}}{\mathrm{d}t}\hat{O} = \frac{i}{\hbar}[\hat{H}, \hat{O}] + \sum_k \gamma_k \Big(\hat{L}_k^\dagger \hat{O} \hat{L}_k - \frac{1}{2}\{\hat{L}_k^\dagger \hat{L}_k, \hat{O}\}\Big) \\ + \sum_k \sqrt{\gamma_k}\Big(\hat{b}_{\mathrm{in},k}^\dagger(t)[\hat{O}, \hat{L}_k] + \hat{b}_{\mathrm{in},k}(t)[\hat{L}_k^\dagger, \hat{O}]\Big), \end{aligned} \tag{3.30}$$

where $\hat{b}_{\mathrm{in},k}(t) = \frac{1}{\sqrt{2\pi}} \int \mathrm{d}\omega e^{-i\omega(t-t_0)} \hat{b}_k(\omega)$.

Given the vacuum state $|0_\omega\rangle_{\mathrm{E}}$ of the thermal baths, we define $\hat{\rho}_{\mathrm{in}} = |0_\omega\rangle_{\mathrm{E}} \langle 0_\omega|_{\mathrm{E}}$. By defining a quantum average as $\mathbb{E}_{\mathrm{Q}}[\,\cdot\,] \equiv \mathrm{Tr}_{\mathrm{E}}(\hat{\rho}_{\mathrm{in}}\,\cdot\,)$ the following relation holds

$$\mathbb{E}_{\mathrm{Q}}[\hat{b}_k(\omega)\hat{b}_j^\dagger(\omega')] = \mathrm{Tr}_{\mathrm{E}}(\hat{\rho}_{\mathrm{in}}\hat{b}_k(\omega)\hat{b}_j^\dagger(\omega')) = \delta_{kj}\delta(\omega - \omega') \tag{3.31}$$

and the mean value of any other combination of two bath operators is zero. We notice that by identifying

$$\mathrm{d}\hat{B}_k(t) = \hat{b}_{\mathrm{in},k}(t)\mathrm{d}t, \tag{3.32}$$

then the only non zero mean value involving a combination of two such operators is

$$\mathbb{E}_{\mathrm{Q}}\Big[\mathrm{d}\hat{B}_k(t)\mathrm{d}\hat{B}_j^\dagger(t)\Big] = \delta_{kj}\mathrm{d}t. \tag{3.33}$$

Eq. (3.33) generalizes to operators the properties of means and correlations of classical Wiener increments $\mathrm{d}W(t)$. Thus, the operators $\hat{B}_k(t)$ can be interpreted as the quantum generalization of Wiener processes [20, 21] and from Eq. (3.30) one can write down the following quantum stochastic differential equation (QSDE) for the state vector of the system-environment $|\Psi_t\rangle$

$$\mathrm{d}|\Psi_t\rangle = \Big[-\frac{i}{\hbar}\hat{H}\mathrm{d}t + \sum_k \sqrt{\gamma_k}\left(\hat{L}_k\,\mathrm{d}\hat{B}_k^\dagger(t) - \hat{L}_k^\dagger\,\mathrm{d}\hat{B}_k(t)\right) - \sum_k \frac{\gamma_k}{2}\hat{L}_k^\dagger\hat{L}_k dt\Big]\,|\Psi_t\rangle\,. \tag{3.34}$$

Such equation leads to the Lindblad master equation for the density matrix $\hat{\rho}$ of the system, when this is calculated as $\hat{\rho}_t = \mathrm{Tr}_{\mathrm{E}}(|\Psi_t\rangle\langle\Psi_t|)$. To show this fact, we assume that the initial state of system-environment is factorized as $|\Psi_{t_0}\rangle = |\psi_{t_0}\rangle_S\,|0_\omega\rangle_E$ and for simplicity we consider a single Lindblad operator $\hat{L}$ with coefficient γ, the generalization to more Lindblad operators being straightforward. Starting from $\hat{\rho}_t = \mathrm{Tr}_{\mathrm{E}}(|\Psi_t\rangle\langle\Psi_t|)$, we differentiate on both sides to get

$$\mathrm{d}\hat{\rho}_t = \mathrm{Tr}_{\mathrm{E}}\big(\mathrm{d}|\Psi_t\rangle\langle\Psi_t| + |\Psi_t\rangle\mathrm{d}\langle\Psi_t| + \mathrm{d}|\Psi_t\rangle\mathrm{d}\langle\Psi_t|\big). \tag{3.35}$$

By using the expression for $\mathrm{d}|\Psi_t\rangle$ in Eq. (3.34), its conjugate for $\mathrm{d}\langle\Psi_t|$, and neglecting terms of order $\mathcal{O}(\mathrm{d}t^2)$ one gets

$$\begin{aligned}
\mathrm{d}\hat{\rho}_t &= -\frac{i}{\hbar}[\hat{H},\hat{\rho}_t]\mathrm{d}t - \frac{\gamma}{2}\{\hat{L}^\dagger\hat{L},\hat{\rho}_t\}\mathrm{d}t + \sqrt{\gamma}\hat{L}\,\mathrm{Tr}_{\mathrm{E}}\big(\mathrm{d}\hat{B}^\dagger(t)\,|\Psi_t\rangle\langle\Psi_t|\big)\\
&- \sqrt{\gamma}\hat{L}^\dagger\,\mathrm{Tr}_{\mathrm{E}}\big(\mathrm{d}\hat{B}(t)\,|\Psi_t\rangle\langle\Psi_t|\big) + \sqrt{\gamma}\,\mathrm{Tr}_{\mathrm{E}}\big(|\Psi_t\rangle\langle\Psi_t|\mathrm{d}\hat{B}(t)\big)\hat{L}^\dagger\\
&- \sqrt{\gamma}\,\mathrm{Tr}_{\mathrm{E}}\big(|\Psi_t\rangle\langle\Psi_t|\mathrm{d}\hat{B}^\dagger(t)\big)\hat{L} + \gamma\hat{L}\,\mathrm{Tr}_{\mathrm{E}}\big(\mathrm{d}\hat{B}^\dagger(t)\,|\Psi_t\rangle\langle\Psi_t|\mathrm{d}\hat{B}\big)\hat{L}^\dagger\\
&- \gamma\hat{L}\,\mathrm{Tr}_{\mathrm{E}}\big(\mathrm{d}\hat{B}^\dagger(t)\,|\Psi_t\rangle\langle\Psi_t|\mathrm{d}\hat{B}^\dagger(t)\big)\hat{L} - \gamma\hat{L}^\dagger\,\mathrm{Tr}_{\mathrm{E}}\big(\mathrm{d}\hat{B}\,|\Psi_t\rangle\langle\Psi_t|\mathrm{d}\hat{B}\big)\hat{L}^\dagger\\
&+ \gamma\hat{L}^\dagger\,\mathrm{Tr}_{\mathrm{E}}\big(\mathrm{d}\hat{B}\,|\Psi_t\rangle\langle\Psi_t|\mathrm{d}\hat{B}^\dagger(t)\big)\hat{L}\\
&= -\frac{i}{\hbar}[\hat{H},\hat{\rho}_t]\mathrm{d}t - \frac{\gamma}{2}\{\hat{L}^\dagger\hat{L},\hat{\rho}_t\}\mathrm{d}t + \gamma\hat{L}\hat{\rho}_t\hat{L}^\dagger\mathrm{d}t
\end{aligned} \tag{3.36}$$

where we used the fact that since $\mathrm{d}\hat{B}(t_0)\,|\Psi_{t_0}\rangle = 0$ then $\mathrm{d}\hat{B}(t)\,|\Psi_t\rangle = 0$ at all times [22], together with the ciclicity of the trace, which implies that the only term surviving is the second term in the third line, leading to the Lindblad master equation, Eq. (2.12). We mention that the equivalence is valid for a generic state $|\Psi_t\rangle$ of the system-environment, i.e. not necessarily factorized, as far as this state is

evolved from an initial state which is factorized with the bath in the vacuum state i.e. $|\Psi_{t_0}\rangle = |\psi_{t_0}\rangle_S |0_\omega\rangle_E$.

Similarly to the standard stochastic Schrödinger equation (see Eq. (3.22)), since Eq. (3.34) is linear its solution can be written as

$$|\Psi_t\rangle = \hat{\mathrm{N}}_g(t, t_0) |\Psi_{t_0}\rangle \ . \tag{3.37}$$

The matrix $\hat{\mathrm{N}}_g(t, t_0)$ has another important property: it is always unitary. However this comes at the price of enlarging the Hilbert space, as $\hat{\mathrm{N}}_g(t, t_0)$ is unitary in the system-environment Hilbert space. The latter is a reservoir of thermal baths with infinite dimension, making the approach of no practical use, in principle. However, in Chapter 7 we show that it is possible to define a suitable finite representation of the $\mathrm{d}\hat{B}$ operators, such that they act on a single bath qubit, i.e. on a two dimensional Hilbert space. Even if this leads to a finite dimensional matrix $\hat{\mathrm{N}}_g(t, t_0)$, if the approach has to be used for classical simulating the output of noisy quantum circuits, it is not favourable from the computational point of view with respect to the classical noisy gates approach introduced in Sec. 3.1.3 as, even in this finite representation, the dimension of $\hat{\mathrm{N}}_g(t, t_0)$ is double that of the noisy gates $\hat{N}_g(t, t_0)$ in Eq. (3.23). This is a consequence of the fact that unitarity is possible only in a larger physical system.

However unitarity opens up the possibility of using this framework in a way that goes beyond the classical simulation of noisy quantum circuits: in Chapter 7 we show that it is possible to implement $\hat{\mathrm{N}}_g(t, t_0)$ in Eq. (3.37) as unitary gates on a quantum computer, effectively devising a quantum algorithm that simulates the dynamics of open quantum systems.

3.2 Libraries for noisy quantum circuit simulations

There exist many relevant quantum computing software frameworks. In Tab. 3.2 we list them together with the indication of which of the algorithmic approach described above they apply. Most of them rely on Alg. 1 which for this reason is generally regarded as the standard approach. Few examples implement Alg. 2. None of the software frameworks in Tab. 3.2 implements Alg. 3. The added value of this work is that the noisy gates approach presented here is available as an open source python package QUANTUM-GATES at this link. The current available version of the QUANTUM-GATES package implements the noisy gate approach that will be presented in the next chapters, designed on IBM superconducting devices.

Company	**Name**	**Ref.**	**Alg. I**	**Alg. II**	**Alg. III**
IBM	Qiskit	[23]	Yes	-	-
Rigetti	pyQuil	[24]	Yes	-	-
Quantinuum	t$\|ket\rangle$	[25]	Yes	-	-
Xanadu	Pennylane	[26]	Yes	-	-
Xanadu	Strawberry Field	[27]	Yes	-	-
Microsoft	LIQUI$\|\rangle$	[28]	Yes	-	-
Google	Cirq	[29]	Yes	-	-
Google	TensorFlow Quantum	[30]	Yes	-	-
Intel	Intel QS	[31]	Yes	-	-
Baidu	Paddle Quantum	[32]	Yes	-	-
Amazon	Braket	[33]	Yes	-	-
-	QiBO	[34]	Yes	-	-
-	QuTiP	[35]	-	Yes	-

Table 3.1: List of relevant quantum computing software frameworks. In the first column we list the owner companies while in the fourth, fifth and sixth columns we specify whether the noise simulation is implemented through Alg. 1, Alg. 2 or Alg. 3 respectively.

Chapter 4

The noisy gates approach

In this chapter we derive the analytic and approximate expression of the stochastic noisy gates introduced in Sec. 3.1.3. We show how this expression is statistically equivalent to an approximate solution to first order in the noise parameters of the Lindblad equation, as in Eq. (3.6). We finally comment on the properties of the noisy gates.

4.1 General derivation of noisy gates

In order to derive the analytic expression for the noisy gates, we consider the linear stochastic unraveling of the Lindbald equation in terms of the stochastic Schrödinger equation introduced in Sec. 3.1.3

$$\mathrm{d}|\psi_t\rangle = \left[-\frac{i}{\hbar}\hat{H}_t\mathrm{d}t + i\epsilon\sum_k \hat{L}_k\mathrm{dW}_k(t) - \frac{\epsilon^2}{2}\sum_k \hat{L^\dagger}_k\hat{L}_k\mathrm{d}t\right]|\psi_t\rangle \ , \tag{4.1}$$

where $\hat{H}_t$ is the time dependent Hamiltonian realizing a given gate, and $\hat{L}_k$ are the Lindblad operators capturing the action of the environment. For practical purposes we now indicate with $\epsilon := \sqrt{\gamma}$. We notice that, in principle, a different $\epsilon_k := \sqrt{\gamma_k}$ should correspond to each $\hat{L}_k$ in Eq. (2.12); however, for simplicity and without loss of generality, we assume that all noise strengths are of the same order of magnitude, and we consider a single ϵ. In general, Eq. (4.1) cannot be solved in a closed form [20, 36] except for few specific cases, for example when all operators commute. We show how to solve Eq. (4.1) to order $O(\epsilon^2)$, valid for small ϵ, by using perturbative methods for stochastic differential equations [20].

4.1.1 Small noise expansion

We use a perturbative method known as *small noise expansion* or *asymptotic perturbative expansion* [20]. For simplicity, let us consider the Stochastic Schrödinger equation in Eq. (4.1) with a single Lindblad operator

$$d\left|\psi_t\right\rangle = \left[-\frac{i}{\hbar}\hat{H}_s \mathrm{d}t + i\epsilon\hat{L}\mathrm{dW}_t - \frac{\epsilon^2}{2}\hat{L}^\dagger\hat{L}\mathrm{d}t\right]\left|\psi_t\right\rangle, \tag{4.2}$$

the generalization to the general case of multiple Lindblad operators being straightforward, and let us set the following ansatz

$$\left|\psi_t\right\rangle = \left|\psi_s^0\right\rangle + \epsilon\left|\psi_t^1\right\rangle + \epsilon^2\left|\psi_t^2\right\rangle + \mathcal{O}(\epsilon^3). \tag{4.3}$$

Substituting this ansatz into Eq. (4.2) and equating terms with the same power of ϵ, we get a system of stochastic differential equations (SDE)

$$\begin{aligned}
\mathrm{d}\left|\psi_t^0\right\rangle &= -\frac{i}{\hbar}\hat{H}_t\left|\psi_t^0\right\rangle \mathrm{d}t \\
\mathrm{d}\left|\psi_t^1\right\rangle &= -\frac{i}{\hbar}\hat{H}_t\left|\psi_t^1\right\rangle \mathrm{d}t + i\hat{L}\left|\psi_t^0\right\rangle \mathrm{dW}_t \\
\mathrm{d}\left|\psi_t^2\right\rangle &= -\frac{i}{\hbar}\hat{H}_t\left|\psi_t^2\right\rangle \mathrm{d}t + i\hat{L}\left|\psi_t^1\right\rangle \mathrm{dW}_t - \frac{1}{2}\hat{L}^\dagger\hat{L}\left|\psi_t^0\right\rangle \mathrm{d}t,
\end{aligned} \tag{4.4}$$

which must be solved with the initial condition $\left|\psi_{t_0}^0\right\rangle = \left|\psi_{t_0}\right\rangle$. The zero-th order differential equation is the standard Schrödinger evolution driven by the gate Hamiltonian, hence its expression is $\left|\psi_t^0\right\rangle = \hat{U}(t,t_0)\left|\psi_{t_0}\right\rangle$, where $\hat{U}(t,t_0) = e^{-i/\hbar\int_{t_0}^t \hat{H}(s)\mathrm{d}s}$. The first order SDE is an example of a time-dependent Ornstein-Uhlenbeck process [20]. In this case the stochastic term of the equation does not depend on the process itself, $\left|\psi_t^1\right\rangle$. For this type of stochastic differential equations the solution is known and it is given by [20]

$$\left|\psi_t^1\right\rangle = i\hat{U}(t,t_0)\hat{S}(t,t_0)\left|\psi_0\right\rangle, \tag{4.5}$$

where we defined the matrix $\hat{S}(t,t_0) = \int_{t_0}^t \mathrm{dW}_s\hat{L}(s,t_0)$ of random processes called Itô integrals, with $\hat{L}(s,t_0) = \hat{U}^\dagger(s,t_0)\hat{L}\hat{U}(s,t_0)$ the time dependent Lindblad operator. The solution to the second order SDE is expressed as

$$\left|\psi_t^2\right\rangle = -\hat{U}(t,t_0)\left[\frac{1}{2}\int_{t_0}^t \hat{L}^\dagger(s,t_0)\hat{L}(s,t_0)\mathrm{d}s + \int_{t_0}^t \hat{L}(s,t_0)\hat{S}(s,t_0)\mathrm{dW}_s\right]\left|\psi_0\right\rangle. \tag{4.6}$$

Then, the solution to order ϵ^2 is given by $\left|\psi_t\right\rangle = \hat{N}_g(t,t_0)\left|\psi_0\right\rangle + \mathcal{O}(\epsilon^3)$, where the noisy gate is $\hat{N}_g(t,t_0) = \hat{U}(t,t_0)\hat{N}(t,t_0)$, with

$$\hat{N}(t,t_0) = \left[\mathbb{1} + i\epsilon\hat{S}(t,t_0) - \frac{\epsilon^2}{2}\int_{t_0}^t \hat{L}^\dagger(s,t_0)\hat{L}(s,t_0)\mathrm{d}s - \epsilon^2\int_{t_0}^t \hat{L}(s,t_0)\hat{S}(s,t_0)\mathrm{dW}_s\right]. \tag{4.7}$$

We can recast the last term in the above equation in a suitable form by using Itô calculus [20]. We start from

$$\begin{aligned}\mathrm{d}\hat{S}^2(t,t_0) =& \mathrm{d}\hat{S}(t,t_0)\hat{S}(t,t_0) + \hat{S}(t,t_0)\mathrm{d}\hat{S}(t,t_0) + \mathrm{d}\hat{S}(t,t_0)\mathrm{d}\hat{S}(t,t_0) \\ =& \hat{L}(t,t_0)\hat{S}(t,t_0)\mathrm{d}W_t + \hat{S}(t,t_0)\hat{L}(t,t_0)\mathrm{d}W_t + \hat{L}^2(t,t_0)\mathrm{d}t \\ =& 2\hat{L}(t,t_0)\hat{S}(t,t_0)\mathrm{d}W_t - [\hat{L}(t,t_0),\hat{S}(t,t_0)]\mathrm{d}W_t + \hat{L}^2(t,t_0)\mathrm{d}t\end{aligned} \tag{4.8}$$

where we used the fact that $(\mathrm{d}W_t)^2 = \mathrm{d}t$ and $[\cdot,\cdot]$ is the commutator. Isolating for $\hat{L}(t,t_0)\hat{S}(t,t_0)\mathrm{d}W_t$ and integrating over $[t,t_0]$ on both sides of the equation, one has that

$$\int_{t_0}^{t} \hat{L}(s,t_0)\hat{S}(s,t_0)\mathrm{d}W_s = \frac{1}{2}\int_{t_0}^{t} \hat{S}^2(s,t_0) - \frac{1}{2}\int_{t_0}^{t} \hat{L}^2(s,t_0)\mathrm{d}s + \hat{C}(t,t_0)\,, \tag{4.9}$$

where we have defined $\hat{C}(t,t_0) := \frac{1}{2}\int_{t_0}^{t}[\hat{L}(s,t_0),\hat{S}(s,t_0)]\mathrm{d}W_s$. Substituting this expression into Eq. (4.7), we get to second order

$$\hat{N}(t,t_0) = \mathbb{1} + i\epsilon\hat{S}(t,t_0) - \frac{\epsilon^2}{2}\hat{S}^2(t,t_0) - \frac{\epsilon^2}{2}\hat{D}(t,t_0) + \epsilon^2\hat{C}(t,t_0) \tag{4.10}$$

where $\hat{D}(t,t_0) := \int_{t_0}^{t}(\hat{L}^\dagger(s,t_0)\hat{L}(s,t_0) - \hat{L}^2(s,t_0))\mathrm{d}s$ is a deterministic term. Inserting the final expression in Eq. (4.10) in the noisy gate $\hat{N}_g(t,t_0)$, the latter is equivalent to an approximate solution of the Lindblad equation as in Eq. (3.6)

$$\begin{aligned}&\rho(t) = \mathbb{E}[|\psi_t\rangle\langle\psi_t|] = \mathbb{E}[\hat{N}_g(t,t_0)\,|\psi_{t_0}\rangle\langle\psi_{t_0}|\,\hat{N}_g^\dagger(t,t_0)] \\ &= \hat{U}(t,t_0)\mathbb{E}\Big[\big(\mathbb{1} + i\epsilon\hat{S}(t,t_0) - \frac{\epsilon^2}{2}\hat{S}^2(t,t_0) - \frac{\epsilon^2}{2}\hat{D}(t,t_0) + \epsilon^2\hat{C}(t,t_0)\big) \\ &\hat{\rho}(t_0)\big(\mathbb{1} + i\epsilon\hat{S}^\dagger(t,t_0) - \frac{\epsilon^2}{2}\hat{S}^{\dagger 2}(t,t_0) - \frac{\epsilon^2}{2}\hat{D}^\dagger(t,t_0) + \epsilon^2\hat{C}^\dagger(t,t_0)\big)\Big]\hat{U}^\dagger(t,t_0) \\ &= \hat{U}(t,t_0)\Big[\hat{\rho}(t_0) + \epsilon^2\int_{t_0}^{t}\hat{L}(s,t_0)\hat{\rho}(t_0)\hat{L}^\dagger(s,t_0)\mathrm{d}s \\ &- \frac{\epsilon^2}{2}\int_{t_0}^{t}\{\hat{L}^\dagger(s,t_0)\hat{L}(s,t_0),\hat{\rho}(t_0)\}\mathrm{d}s\Big]\hat{U}^\dagger(t,t_0) \\ &= \hat{U}(t,t_0)\Big[\mathbb{1} + \int_{t_0}^{t}\mathcal{L}_D(s)\mathrm{d}s\hat{\rho}(t_0)\Big]\hat{U}^\dagger(t,t_0)\,,\end{aligned} \tag{4.11}$$

where we are keeping only terms up to order ϵ^2 and we used the fact that $\mathbb{E}[\hat{S}^2(t,t_0)] = \int_{t_0}^{t}\hat{L}^2(s,t_0)\mathrm{d}s$ and $\mathbb{E}[\hat{S}^{2\dagger}(t,t_0)] = \int_{t_0}^{t}\hat{L}^{2\dagger}(s,t_0)\mathrm{d}s$, which is a consequence of Eq. (4.9)

and the fact that $\mathbb{E}[\hat{C}(t,t_0)] = \mathbb{E}[\hat{C}^\dagger(t,t_0)] = 0$. Indeed

$$\begin{aligned}\mathbb{E}[\hat{C}(t,t_0)] &= \mathbb{E}\left[\frac{1}{2}\int_{t_0}^{t}\hat{L}(s,t_0)\hat{S}(s,t_0)\mathrm{d}W_s\right] - \mathbb{E}\left[\frac{1}{2}\int_{t_0}^{t}\hat{S}(s,t_0)\hat{L}(s,t_0)\mathrm{d}W_s\right] \\ &= \mathbb{E}\left[\frac{1}{2}\int_{t_0}^{t}\int_{t_0}^{s}\hat{L}(s,t_0)\hat{L}(u,t_0)\mathrm{d}W_u\mathrm{d}W_s\right] - \mathbb{E}\left[\frac{1}{2}\int_{t_0}^{t}\int_{t_0}^{s}\hat{L}(u,t_0)\mathrm{d}W_u\hat{L}(s,t_0)\mathrm{d}W_s\right],\end{aligned} \tag{4.12}$$

both terms in the last line have mean zero, since the process integrated over $\mathrm{d}W_s$, which is $\int_{t_0}^{s}\hat{L}(u,t_0)\mathrm{d}W_u$, depends on $\mathrm{d}W$ at times u always earlier than s and thus it is non anticipating [20]. Itô integrals of non anticipating functions have mean zero [20]. Despite this fact, the term $\hat{C}(t,t_0)$ is problematic from the computational point of view in a single realization of $\hat{N}_g(t,t_0)$. Being the sum of two matrices of Itô integrals whose integrand are random processes, their probability distributions are generally not known. This raises the problem of how to sample processes inside $\hat{C}(t,t_0)$. However, the derivation in Eq. (4.11) shows that the presence of the term $\hat{C}(t,t_0)$ is important to order ϵ^2 only in a single realization, but its effects on the final averaged density matrix are washed away, i.e. on average it gives zero contribution to the final density matrix. For this reason we can simply drop $\hat{C}(t,t_0)$ in Eq. (4.10), and write

$$\begin{aligned}\hat{N}(t,t_0) &= \mathbb{1} + i\epsilon\hat{S}(t,t_0) - \frac{\epsilon^2}{2}\hat{S}^2(t,t_0) - \frac{\epsilon^2}{2}\hat{D}(t,t_0) \\ &= \left[\mathbb{1} - \frac{\epsilon^2}{2}\hat{D}(t,t_0)\right]\left[\mathbb{1} + i\epsilon\hat{S}(t,t_0) - \frac{\epsilon^2}{2}\hat{S}^2(t,t_0)\right] \\ &= e^{-\frac{\epsilon^2}{2}\hat{D}(t,t_0)}e^{i\epsilon\hat{S}(t,t_0)} + \mathcal{O}(\epsilon^3),\end{aligned} \tag{4.13}$$

where the second equality holds to order ϵ^2. The expression for $\hat{N}(t,t_0)$ in Eq. (4.13) leads to the same approximate average density matrix in Eq. (4.11).

The final expression for $\hat{N}_g$ generalizes in the case of multiple Lindblad operators $\hat{L}_k$. Now we substitute different $\epsilon_k := \sqrt{\gamma_k}$ for each Lindblad operators, and the expression becomes

$$\hat{N}_g(t,t_0) = \hat{U}(t,t_0)e^{\hat{\mathcal{D}}(t,t_0)}e^{i\hat{\mathcal{S}}(t,t_0)}\,, \tag{4.14}$$

where the deterministic term $\hat{\mathcal{D}}(t,t_0)$ and the stochastic term $\hat{\mathcal{S}}(t,t_0)$ are defined as

$$\begin{aligned}\hat{\mathcal{D}}(t,t_0) &= \sum_k \hat{D}_k(t,t_0) = -\sum_k \frac{\gamma_k}{2}\int_{t_0}^{t}\mathrm{d}s(\hat{L}_k^\dagger(s,t_0)\hat{L}_k(s,t_0) - \hat{L}_k^2(s,t_0)) \\ \hat{\mathcal{S}}(t,t_0) &= \sum_k \hat{S}_k(t,t_0) = \sum_k \sqrt{\gamma_k}\int_{t_0}^{t}\hat{L}_k(s,t_0)\mathrm{d}W_s\,.\end{aligned} \tag{4.15}$$

4.1.2 Protocol for noisy gates simulations

At a first glance, Eq. (4.14) suggests that the final expression has a unitary (ideal) term $\hat{U}(t,t_0)$ separated from the noise terms $e^{\hat{\mathcal{D}}(t,t_0)}e^{i\hat{\mathcal{S}}(t,t_0)}$, thus we obtained a noise gate rather than a noisy gate. Indeed such terms act as separate matrices on the state vector. However, it has to be noted that $e^{\hat{\mathcal{D}}(t,t_0)}$ and $e^{i\hat{\mathcal{S}}(t,t_0)}$ contain the Lindblad operators $\hat{L}_k(s,t_0)$ in the interaction picture, $\hat{L}_k(s,t_0) = \hat{U}^\dagger(s,t_0)\hat{L}_k\hat{U}(s,t_0)$, which make them dependent on the gate Hamiltonian, i.e. the noise dynamics is influenced by the unitary evolution realized by $\hat{U}(t,t_0)$.

Moreover, the final noisy gate expression in Eq. (4.14) is very handy from the computational point of view. The real part $[\hat{S}_k^R(t,t_0)]_{ij}$ and the imaginary part $[\hat{S}_k^I(t,t_0)]_{ij}$ of the entries of the operators $\hat{S}_k$ in Eq. (4.15) are Itô integrals of deterministic functions: $[\hat{S}_k^m(t,t_0)]_{ij} = \int_{t_0}^t \mathrm{dW}_k(s)[\hat{L}_k^m(s,t_0)]_{ij}$ for $m = R, I$. Differently from entries of the problematic term $\hat{C}(t,t_0)$, their probability distribution is known. They are Gaussian stochastic processes with means zero

$$\mathbb{E}\big[[\hat{S}_k^m(t,t_0)]_{ij}\big] = 0\,, \tag{4.16}$$

and with variances and covariances given by

$$\begin{aligned}
\mathbb{V}\big[[\hat{S}_k^m(t,t_0)]_{ij}\big] &= \int_{t_0}^t \mathrm{d}s([\hat{L}_k^m(s,t_0)]_{ij})^2 \\
\mathbb{E}\big[[\hat{S}_k^m(t,t_0)]_{ij}[\hat{S}_k^n(t,t_0)]_{i'j'}\big] &= \int_{t_0}^t \mathrm{d}s[\hat{L}_k^m(s,t_0)]_{ij}[\hat{L}_k^n(s,t_0)]_{i'j'}\,.
\end{aligned} \tag{4.17}$$

Once all the variances and covariances are computed, the stochastic processes can be sampled to generate a single realization of each $\hat{S}_k(t,t_0)$, to be used to compute $e^{i\hat{\mathcal{S}}(t,t_0)}$. Indeed for each $\hat{S}_k(t,t_0)$ the final resulting probability distribution is a multi-normal distribution with zero mean and with covariance matrix defined by the variances and covariances of its entries. Sampling from such distributions has a constant computational cost. Other terms in $\hat{N}_g$ are deterministic and can be easily computed.

The noisy gate approach presented here is general and valid for any Hamiltonian and Lindblad operators. As such it can be applied to different noisy quantum computers, as long as the approximation holds. The approach results in the following procedure to implement the simulations of noisy quantum circuit on a given device through Alg. 3

1. specify the Hamiltonians, i.e. the unitaries, realizing the set of native gates of the given quantum device. This constitutes a universal set with a very limited number of gates;

2. given a noise model of the device specify all the possible Lindblad operators and compute them in the interaction picture for each native gate. Find the resulting expressions of each native noisy gate in Eq. (4.14);

3. characterize the momenta in Eqs. (4.16) and (4.17) of the Itô integrals appearing in $\hat{\mathcal{S}}(t, t_0)$.

Native gates are usually single-qubit or two-qubit operations and typical noises have a limited m locality of the Lindbladians, meaning that Lindblad operators act non trivially at most on m qubits (generally $m = 2$, meaning nearest neighbor interaction). Thus, the calculation of Lindblad operators in the interaction picture is not computationally intensive: the dimension of matrices to be computed does not scale with the size of the quantum device, but it is ultimately dictated by the locality of the noise. In the next chapter we follow the outlined procedure for IBM superconducting devices. In this case it is rather straightforward to carry out results with analytic calculations. However me mention that all these steps can be easily automated.

Once all the steps are performed, given an ideal quantum circuit decomposed into native gates it is sufficient to follow Alg. 3. By averaging over the number $\mathrm{N}_{\mathrm{samples}}$ of realizations of the final state $|\psi_t\rangle_k$, one recovers the final density matrix of the system

$$\hat{\rho} = \frac{1}{\mathrm{N}_{\mathrm{samples}}} \sum_k |\psi_t\rangle_k \langle\psi_t|_k \ , \tag{4.18}$$

where $\hat{\rho}$ is an approximate solution of the Lindblad equation as in Eq. (3.6).

Chapter 5

Noisy gates on IBM superconducting devices

In this chapter we specify the noisy gates method on IBM superconducting quantum computers [5]. The primary aim is to show the improved performance of Alg. 3 with respect to the standard Alg. 1. Particularly, to implement the latter we use the noise simulator provided by Qiskit (see also Tab.3.2). We show the superiority of Alg. 3 in the simplest scenario possible: a standard underlying noise model. Casting the behaviour of a real quantum device in a complete noise model is a hard task, and the more accurate the model, the less general it is. The aim is not that of finding the best noise model for a given quantum computer; rather, given a noise model, we are interested in the best way, in terms of accuracy and computational resources, to simulate its effects on quantum circuits. The standard noise model that we employ gives appreciable results in the simulations, allowing to enlighten the main points. When the aim is that of predicting the output of the noisy devices as accurately as possible, better results can be achieved by refining the noise model. This goes beyond the scope of this chapter.

First we report all Kraus maps of the standard noise model, necessary for Alg. 1 and their equivalent Lindblad terms, necessary for Alg. 3; then we specialize the general derivation of the noisy gates presented in Chapter 4 to the native single and two-qubits gates of IBM devices. We discuss the results of the simulations, which test our approach against the standard one in reproducing the solution of the Lindlbad equation, as well as the outcomes of current IBM quantum computers. We conclude with some general remarks.

5.1 Standard noise model

The noises which are more relevant in the functioning of superconducting devices have extensively been characterized in the literature [2,6,37]; in this section we briefly present the standard noise model that we used for the simulations. First we indicate the Kraus maps needed for Alg. 1. Then we present their equivalent Lindblad terms needed for Alg. 3.

5.1.1 Kraus maps

The standard noise model assumes that noises associated to gate execution are suitable compositions of single-qubit depolarization and single-qubit amplitude and phase damping, noise associated to measurements is the single-qubit bitflip channel and noise acting on idle qubits is the single-qubit amplitude and phase damping channel [37, 38]. Here we report the Kraus maps for these channels. These define a custom noise model in Qiskit that is used for the simulations through Alg. 1.

Single-qubit depolarization brings the qubit state towards the totally mixed one [6], $\mathbb{1}/\sqrt{2}$; the Kraus map of single-qubit depolarization on the a-th qubit reads

$$\mathcal{E}_d^{(a)}(\hat{\rho}) = \big(1 - \frac{3}{4}p^{(a)}\big)\hat{\rho} + \frac{p^{(a)}}{4}\hat{X}\hat{\rho}\hat{X} + \frac{p^{(a)}}{4}\hat{Y}\hat{\rho}\hat{Y} + \frac{p^{(a)}}{4}\hat{Z}\hat{\rho}\hat{Z}\,, \tag{5.1}$$

where $\hat{\rho}$ is the density matrix of the qubit, $\hat{X}, \hat{Y}, \hat{Z}$ are the Pauli matrices and $p^{(a)}/4$ is the equal probability of having a bit flip, a phase flip or a bit and phase flip of the states of the computational basis. The probability $p^{(a)}$ used in the simulations is the single-qubit gate error provided as a calibration parameter for IBM devices. We assume a behaviour in time of the form $p^{(a)} = (1 - e^{-\gamma_d^{(a)} t})$ for a characteristic time $T_d^{(a)} = 1/\gamma_d^{(a)}$ and with t the evolution time.

The second type of noise associated to gates execution is due to the thermalization with the environment, inducing the decay of the qubit towards its ground state $|0\rangle$, an effect which is also known as amplitude damping [2, 6]. Amplitude damping of the a-th qubit is characterized by a relaxation time $T_1^{(a)}$, which identifies the time scale for the initial state to decay towards $|0\rangle$; in turn this induces also a damping of the off-diagonal elements of the density matrix, a phase damping, which (if only amplitude damping is acting) has a characteristic time $2T_1^{(a)}$. However, at the same time the environment contributes with a further pure phase damping, resulting in an effective dephasing rate $1/T_2^{(a)} \geq 1/2T_1^{(a)}$. The Kraus map of the single-qubit amplitude and phase damping on the a-th qubit is given by [2,6]

$$\mathcal{E}_{apd}^{(a)}(\hat{\rho}) = \hat{K}\hat{\rho}\hat{K} + p_1^{(a)}\hat{\sigma}^-\hat{\rho}\hat{\sigma}^+ + p_z^{(a)}\hat{\mathcal{P}}_1\hat{\rho}\hat{\mathcal{P}}_1\,, \tag{5.2}$$

where we defined the operator

$$\hat{K} = \begin{pmatrix} 1 & 0 \\ 0 & \sqrt{1 - p_1^{(a)} - p_z^{(a)}} \end{pmatrix} , \tag{5.3}$$

and $\hat{\mathcal{P}}_1 = |1\rangle\langle 1|$ is the projector onto the $|1\rangle$ state. In this case, $p_1^{(a)} = 1 - e^{-t/T_1^{(a)}}$ is the probability of amplitude damping, t is the evolution time, $T_1^{(a)}$ is the relaxation time and $p_z^{(a)} = (1 - p_1^{(a)})p_{pd}^{(a)}$, where $p_{pd}^{(a)} = 1 - e^{-t/T_{pd}^{(a)}}$ is the probability of pure dephasing with $T_{pd}^{(a)} = T_1^{(a)}T_2^{(a)}/(2T_1^{(a)} - T_2^{(a)})$, $T_2^{(a)}$ being the decoherence time. The time scales $T_1^{(a)}$ and $T_2^{(a)}$ are related as $T_2^{(a)} \leq 2T_1^{(a)}$. The times $T_1^{(a)}$ and $T_2^{(a)}$ that are used in the simulations are directly provided as calibration parameters for IBM devices.

Single-qubit depolarization and amplitude and phase damping are composed to get the Kraus map associated to the execution of single-qubit gates on qubit a

$$\mathcal{E}^{(a)}(\cdot) = \mathcal{E}_d^{(a)}(\cdot) \circ \mathcal{E}_{apd}^{(a)}(\cdot) . \tag{5.4}$$

The Kraus map is equivalent to the Lindblad term in Eq. (5.9) when $t = t_g$, where t_g is the single-qubit gate time, $\gamma_1^{(a)} = 1/T_1^{(a)}$, $\gamma_{pd}^{(a)} = 1/4T_{pd}^{(a)}$, $\gamma_d^{(a)} = p^{(a)}/(4t_g)$.

The standard noise model neglects cross talks and correlated noises [39] between qubits; thus the Kraus map associated to two-qubit gates on qubits a and b is the tensor product of the single-qubit Kraus maps in Eq. (5.4)

$$\mathcal{E}^{(a,b)}(\cdot) = \mathcal{E}^{(a)}(\cdot) \otimes \mathcal{E}^{(b)}(\cdot) . \tag{5.5}$$

The two-qubit Kraus map is equivalent to the Lindblad term in Eq. (5.10) by choosing $t = t_g^{(a,b)}$ the two qubit gate time on qubits a and b, $\gamma_1^{(a)} = 1/T_1^{(a)}$, $\gamma_1^{(b)} = 1/T_1^{(b)}$, $\gamma_{pd}^{(a)} = 1/4T_{pd}^{(a)}$ and $\gamma_{pd}^{(b)} = 1/4T_{pd}^{(b)}$, $\gamma_d^{(a)} = \gamma_d^{(b)} = \gamma_d^{(a,b)} = p^{(a,b)}/(4t_g^{(a,b)})$.

We mention that since in IBM devices $t_g^{(a,b)}$ is ten times larger than t_g, then $p_1^{(a)}$, $p_z^{(a)}$ and $p^{(a,b)}$ are ~ 2 orders of magnitude higher than any probability appearing in the single-qubit Kraus map. Thus, the standard noise model already takes into account that two-qubit operations are more faulty than single-qubit ones.

Along with errors associated with the execution of each gate, the standard model takes into account measurement errors at the very end of a quantum circuit. Such errors are modeled with the single-qubit bit flip channel [6], whose Kraus map on qubit a reads

$$\mathcal{E}_m^{(a)}(\hat{\rho}) = (1 - r^{(a)})\hat{\rho} + r^{(a)}\hat{X}\hat{\rho}\hat{X} , \tag{5.6}$$

where $\hat{X}$ is the X-Pauli matrix and $r^{(a)}$ is the probability of having a flip of the states of the computational basis. The probability $r^{(a)}$ that we used in the simulations is

the readout error provided as a calibration parameter for IBM devices. We assume a behaviour in time of the form $r^{(a)} = (1 - e^{-2\gamma_m^{(a)} t})/2$ for a characteristic time $T_m^{(a)} = 1/\gamma_m^{(a)}$. The map is equivalent to the corresponding Lindblad equation in Eq. (5.11) by choosing $t = t_m^{(a)}$ the measurement time on qubit a, and $\gamma_m^{(a)} = r^{(a)}/t_m^{(a)}$. $t_m^{(a)}$ is also provided as a calibration parameter for IBM devices, and it is usually 100 times larger than single-qubit gate times.

5.1.2 Lindblad terms

We list the Lindblad terms corresponding to the Kraus maps presented above. Single-qubit depolarization on qubit a has the following Lindblad term [2, 6],

$$\mathcal{L}_d^{(a)}(\hat{\rho}) = \gamma_d^{(a)} \sum_{k=1}^{3} \left[\hat{\sigma}^k \hat{\rho} \hat{\sigma}^k - \hat{\rho}\right], \tag{5.7}$$

where $\hat{\sigma}^1 = \hat{X}$, $\hat{\sigma}^2 = \hat{Y}, \hat{\sigma}^3 = \hat{Z}$ are the standard Pauli matrices.

When $T_1 \geq T_2$ holds (and this is the case of interest to us), the single-qubit amplitude and phase damping on qubit a has the following Lindblad term

$$\mathcal{L}_{apd}^{(a)}(\hat{\rho}) = \gamma_1^{(a)} \left[\hat{\sigma}^- \hat{\rho} \hat{\sigma}^+ - \frac{1}{2}\left\{\hat{\mathbb{P}}^{(1)}, \hat{\rho}\right\}\right] + \gamma_{pd}^{(a)} \left[\hat{Z}\hat{\rho}\hat{Z} - \hat{\rho}\right], \tag{5.8}$$

where we use the convention $\hat{\sigma}^- = |0\rangle\langle 1|$ and $\hat{\mathbb{P}}^{(1)} = |1\rangle\langle 1|$ is the projector onto $|1\rangle$;

According to the standard noise model, during the execution of single-qubit gates, we consider both sources of noise together, meaning that the Lindblad term is

$$\mathcal{L}^{(a)}(\rho) = \mathcal{L}_d^{(a)}(\rho) + \mathcal{L}_{apd}^{(a)}(\rho)\,. \tag{5.9}$$

As already pointed out, this term is equivalent to the single-qubit Kraus map in Eq. (5.4) by solving for a time $t = t_g$ and with the choices $\gamma_1^{(a)} = 1/T_1^{(a)}$, $\gamma_{pd}^{(a)} = 1/4T_{pd}^{(a)}$, $\gamma_d^{(a)} = p^{(a)}/4t_g$.

The two-qubit Lindblad term on qubits a and b is obtained with the direct sum

$$\mathcal{L}^{(a,b)}(\rho) = \mathcal{L}^{(a)}(\rho) \bigoplus \mathcal{L}^{(b)}(\rho)\,. \tag{5.10}$$

This is equivalent to the two qubit Kraus map in Eq. (5.5) by solving for a time $t = t_g^{(a,b)}$ and with the choices $\gamma_1^{(a)} = 1/T_1^{(a)}$, $\gamma_1^{(b)} = 1/T_1^{(b)}$, $\gamma_{pd}^{(a)} = 1/4T_{pd}^{(a)}$, $\gamma_{pd}^{(b)} = 1/4T_{pd}^{(b)}$, $\gamma_d^{(a)} = \gamma_d^{(b)} = \gamma_d^{(a,b)} = p^{(a,b)}/4t_g^{(a,b)}$.

For measurements and noises on idle qubits, no drive is implemented and the corresponding Lindblad equation does not contain the Hamiltonian term. The Lindblad

equation for measurement errors is that of a single-qubit bitflip channel. On the a-th qubit this reads

$$\frac{\mathrm{d}}{\mathrm{d}t}\hat{\rho}_t = \gamma_m^{(a)}(\hat{X}\hat{\rho}_t\hat{X} - \hat{\rho}_t). \tag{5.11}$$

Solving for a time $t_m^{(a)}$, with the choice $\gamma_m^{(a)} = r^{(a)}/t_m^{(a)}$ is equivalent to the Kraus map in Eq. (5.6). Finally for idle qubits, i.e. qubits over which no gate is applied while other are manipulated, the Lindblad equation is $\frac{\mathrm{d}}{\mathrm{d}t}\hat{\rho}_t = \mathcal{L}_{apd}^{(a)}(\hat{\rho})$ where $\mathcal{L}_{apd}^{(a)}(\hat{\rho})$ is the single-qubit amplitude and phase damping term in Eq. (5.8). We do not consider depolarization error on idle qubits, because this channel is used to model incoherent gate infidelities.

5.2 Noisy gates derivation

In this section we specialize the general derivation of noisy gates presented in Chapter 4 to the native single-qubit and two-qubit gates of IBM superconducting devices. The underlying noise model is the standard noise model introduced in Sec. 5.1.

5.2.1 Single qubit noisy gates

Single-qubit gates are realized by the capacitive coupling of a microwave drive line with the superconducting transmon qubit in IBM devices. The effective Hamiltonian of the drive is [37, 40]

$$\hat{H}_D(t) = \frac{\hbar}{2}\omega(t)(\cos(\phi)\hat{X} + \sin(\phi)\hat{Y})\,, \tag{5.12}$$

where $\omega(t) = -\chi V_0 s(t)$ is the drive pulse, χ is a parameter depending on the capacities of the transmon qubit and the coupling capacity, V_0 is the amplitude of the drive potential, $s(t)$ is a dimensionless envelope function of the drive pulse and ϕ is an arbitrary phase. The unitary evolution due to the drive Hamiltonian is given by

$$\hat{U}_D(t, t_0) = e^{-\frac{i}{2}\theta(t,t_0)(\cos(\phi)\hat{X}+\sin(\phi)\hat{Y})}\,, \tag{5.13}$$

where $\theta(t, t_0) = \int_{t_0}^{t}\omega(s)\mathrm{d}s$ is the rotation angle on the X-Y plane. In matrix notation Eq. (5.13) reads

$$\hat{U}_D(t, t_0) = \begin{pmatrix} \cos\left(\frac{\theta(t,t_0)}{2}\right) & -i\sin\left(\frac{\theta(t,t_0)}{2}\right)e^{-i\phi} \\ -i\sin\left(\frac{\theta(t,t_0)}{2}\right)e^{i\phi} & \cos\left(\frac{\theta(t,t_0)}{2}\right) \end{pmatrix}. \tag{5.14}$$

In IBM devices, the drive Hamiltonian is calibrated to realize the native single-qubit gates X and SX, which are rotations around the X-axis obtained by setting that $\theta(t,t_0)=\pi$ or $\theta(t,t_0)=\pi/2$ in Eq. (5.13). The additional phase ϕ allows to implement rotations around the z-axis of arbitrary angles as *virtual* gates, since they are mimicked by the software and are not associated to a physical action on the device [40]. We derive the expression of the single-qubit noisy gates with generic unitary evolution as in Eq. (5.14) modified by adding the single-qubit Lindblad term in Eq. (5.9). The corresponding stochastic Schrödinger equation (see Eq. (3.22)) is

$$\begin{aligned}\mathrm{d}|\psi_t\rangle =&\Bigg[-\frac{i}{\hbar}\hat{H}_D(t)\mathrm{d}t+i\sqrt{\gamma_d}\hat{X}\mathrm{d}W_{t,x}+i\sqrt{\gamma_d}\hat{Y}\mathrm{d}W_{t,y}+i\sqrt{\gamma_d}\hat{Z}\mathrm{d}W_{t,z}-\frac{3}{2}\gamma_d\hat{I}\mathrm{d}t\\&+i\sqrt{\gamma}_1\hat{\sigma}^-\mathrm{d}W_{t,1}-\frac{\gamma_1}{2}\hat{\mathcal{P}}_1\mathrm{d}t+i\sqrt{\frac{\gamma_{pd}}{4}}\hat{Z}\mathrm{d}W_{t,2}-\frac{\gamma_{pd}}{8}\hat{I}\mathrm{d}t\Bigg]|\psi_t\rangle\,,\end{aligned}\tag{5.15}$$

to be solved from $t_0=0$ to t_g, the single-qubit gate time. By using the perturbative expression for the noisy gate in Eq. (4.14), we have

$$\begin{aligned}\hat{U}_D^{(N)}(t_g,0)=&\hat{U}_D(t_g,0)\cdot\exp\left(\frac{\gamma_1}{2}\hat{D}(t_g,0)\right)\cdot\exp\Bigg(i\sqrt{\gamma_d}\hat{S}_x(t_g,0)+i\sqrt{\gamma_d}\hat{S}_y(t_g,0)\\&+i\sqrt{\gamma_d}\hat{S}_z(t_g,0)+i\sqrt{\gamma_1}\hat{S}_1(t_g,0)+i\sqrt{\gamma_{pd}/4}\hat{S}_2(t_g,0)\Bigg)\end{aligned}\tag{5.16}$$

where

$$\begin{aligned}&\hat{D}(t,t_0)=\int_{t_0}^{t}\hat{\mathcal{P}}_1(s,t_0)\mathrm{d}s;\quad \hat{S}_x(t,t_0)=\int_{t_0}^{t}\hat{X}(s,t_0)\mathrm{d}W_{s,x}\\&\hat{S}_y(t,t_0)=\int_{t_0}^{t}\hat{Y}(s,t_0)\mathrm{d}W_{s,y};\quad \hat{S}_z(t,t_0)=\int_{t_0}^{t}\hat{Z}(s,t_0)\mathrm{d}W_{s,z};\\&\hat{S}_1(t,t_0)=\int_{t_0}^{t}\hat{\sigma}^-(s,t_0)\mathrm{d}W_{s,1};\quad \hat{S}_2(t,t_0)=\int_{t_0}^{t}\hat{Z}(s,t_0)\mathrm{d}W_{s,2}\end{aligned}\tag{5.17}$$

$\hat{D}(t,t_0)$ is the deterministic term associated to the non Hermitian operator $\hat{\sigma}^-$ of amplitude and phase damping and all other $\hat{S}_k$ are stochastic matrices. As an illustrative example the matrix form of $\hat{S}_z(t,t_0)$ is

$$\hat{S}_z(t,t_0)=\begin{pmatrix}S_{z,1}(t,t_0) & -i\,e^{-i\phi}\,S_{z,2}(t,t_0)\\ i\,e^{i\phi}\,S_{z,2}(t,t_0) & -S_{z,1}(t,t_0)\end{pmatrix},\tag{5.18}$$

where

$$S_{z,1}(t,t_0)=\int_{t_0}^{t}\cos(\theta(s,t_0))\mathrm{d}W_{s,z}\quad S_{z,2}(t,t_0)=\int_{t_0}^{t}\sin(\theta(s,t_0))\mathrm{d}W_{s,z}\,.\tag{5.19}$$

These two Itô integrals have a binormal joint probability distribution, with the following momenta

$$\begin{aligned}
\mathbb{E}[S_{z,1}(t,t_0)] &= \mathbb{E}[S_{z,2}(t,t_0)] = 0 \\
\mathbb{E}[S^2_{z,1}(t,t_0)] &= \int_{t_0}^{t} \cos^2(\theta(s,t_0))\mathrm{d}s \\
\mathbb{E}[S^2_{z,2}(t,t_0)] &= \int_{t_0}^{t} \sin^2(\theta(s,t_0))\mathrm{d}s \\
\mathbb{E}[S_{z,1}(t,t_0)S_{z,2}(t,t_0)] &= \int_{t_0}^{t} \cos(\theta(s,t_0))\sin(\theta(s,t_0))\mathrm{d}s\,.
\end{aligned} \tag{5.20}$$

The remaining $\hat{S}$ matrices in Eq. (5.17) have similar matrix forms, which can be computed straightforwardly. If we assume that $\theta(t,t_0) = \pi$ one gets the noisy gate $\mathrm{X}_N(\phi)$, or with $\theta(t,t_0) = \pi/2$ one gets $\mathrm{SX}_N(\phi)$. We mention that for the simulations in the next section and in the current version of the QUANTUM-GATES library, we considered constant pulses for simplicity, i.e. $\omega(t) = \omega$ with ω constant, being the generalization to general functions rather straightforward. It should be noted that according to the noisy gates approach the functional form of $\theta(t,t_0)$, that in turn depend on that of $\omega(t)$, affects the action of the noises on the system, meaning that different pulse shapes could lead to different or perhaps smaller noise effects, i.e. error mitigation; this is a question left for future research.

Finally we have decided to not diagonalize the single-quibt Lindblad term in Eq. (5.9) in canonical form. In this way it is easier to discern terms coming from depolarization or amplitude and phase damping. The total of five Lindblad operators is redundant as any Lindblad term on n qubits can be diagonalized in canonical form to always have $2^{2n} - 1$ Lindblad operators, thus in the single-qubit case a total of three Lindblad operators. In [41] the derivation is performed with the diagonalized Lindblad term. This procedure involves a rewriting of the latter thus the resulting dynamics is left unchanged and predictions are equivalent in the two formulations.

5.2.2 Two-qubit noisy gates

The native two-qubit interaction in IBM devices is the so-called cross resonant (CR) gate [37, 40, 42], realized by the CR Hamiltonian [37, 40, 42]

$$\hat{H}_{CR}(t) = \frac{\hbar}{2}\omega(t)\hat{Z}\otimes(\cos(\phi)\hat{X} + \sin(\phi)\hat{Y})\,, \tag{5.21}$$

where $\omega(t)$ is the drive pulse and ϕ is an arbitrary phase. The additional phase ϕ allows to implement virtual z gates similarly to single-qubit gates, see [40] for further

details. The corresponding unitary evolution is given by

$$\hat{CR}(t,t_0) = e^{-\frac{i}{2}\theta(t,t_0)\hat{Z}\otimes(\cos(\phi)\hat{X}+\sin(\phi)\hat{Y})} \tag{5.22}$$

where $\theta(t,t_0) = \int_{t_0}^{t}\omega(s)\mathrm{d}s$. In matrix notation Eq. (5.22) reads

$$\hat{CR}(t,t_0) = \begin{pmatrix} \hat{U}_D(\theta(t,t_0),\phi) & 0 \\ 0 & \hat{U}_D(-\theta(t,t_0),\phi) \end{pmatrix}, \tag{5.23}$$

where $\hat{U}_D(\theta(t,t_0),\phi)$ and $\hat{U}_D(-\theta(t,t_0),\phi)$ are as in Eq. (5.14). The CNOT gate and its inverse are implemented by combining single-qubit gates and CR gates.

In order to derive the corresponding CR noisy gate, the unitary dynamics is modified by adding the two-qubit Lindblad term in Eq. (5.10). The corresponding SDE on qubits c, the control, and t, the target, is the following

$$\begin{aligned}
\mathrm{d}|\psi_t\rangle = \Bigg[& -\frac{i}{\hbar}\hat{H}_{CR}(t)\mathrm{d}t + i\sqrt{\gamma_d}\hat{X}\hat{I}\mathrm{d}W_{t,x}^{(c)} + i\sqrt{\gamma_d}\hat{Y}\hat{I}\mathrm{d}W_{t,y}^{(c)} + \\
& i\sqrt{\gamma_d}\hat{Z}\hat{I}\mathrm{d}W_{t,z}^{(c)} + i\sqrt{\gamma_d}\hat{I}\hat{X}\mathrm{d}W_{t,x}^{(t)} + i\sqrt{\gamma_d}\hat{I}\hat{Y}\mathrm{d}W_{t,y}^{(t)} + \\
& i\sqrt{\gamma_d}\hat{I}\hat{Z}\mathrm{d}W_{t,z}^{(t)} - 3\gamma_d\hat{I}\hat{I}\mathrm{d}t + i\sqrt{\gamma_1^{(c)}}\hat{\sigma}^-\hat{I}\mathrm{d}W_{t,1}^{(c)} - \\
& \frac{\gamma_1^{(c)}}{2}\hat{\mathcal{P}}_1\hat{I}\mathrm{d}t + i\sqrt{\gamma_1^{(t)}}\hat{I}\hat{\sigma}^-\mathrm{d}W_{t,1}^{(t)} - \frac{\gamma_1^{(t)}}{2}\hat{I}\hat{\mathcal{P}}_1\mathrm{d}t + \\
& i\sqrt{\frac{\gamma_{pd}^{(c)}}{4}}\hat{Z}\hat{I}\mathrm{d}W_{t,2}^{(c)} + i\sqrt{\frac{\gamma_{pd}^{(t)}}{4}}\hat{I}\hat{Z}\mathrm{d}W_{t,2}^{(t)} - \frac{1}{8}\Big(\gamma_{pd}^{(c)} + \gamma_{pd}^{(t)}\Big)\hat{I}\hat{I}\mathrm{d}t\Bigg]|\psi_t\rangle\,,
\end{aligned} \tag{5.24}$$

where for simplicity the tensor product between operators acting on the two qubits is omitted.

Using the perturbative expression in Eq. (4.14) with $t_0 = 0$ and $t = t_{CR}^{(c,t)}$, where $t_{CR}^{(c,t)}$ is the time needed to implement the cross resonance gate on qubits c and t, we get

$$\begin{aligned}
\hat{CR}_N(t_{CR}^{(c,t)},0) = & \hat{CR}(t_{CR}^{(c,t)},0)\cdot\exp\left(\frac{\gamma_1^{(c)}}{2}\hat{D}^{(c)}(t_{CR}^{(c,t)},0) + \frac{\gamma_1^{(t)}}{2}\hat{D}^{(t)}(t_{CR}^{(c,t)},0)\right) \\
& \cdot\exp\Bigg(i\sqrt{\gamma_d}\hat{S}_x^{(c)}(t_{CR}^{(c,t)},0) + i\sqrt{\gamma_d}\hat{S}_y^{(c)}(t_{CR}^{(c,t)},0) + i\sqrt{\gamma_d}\hat{S}_z^{(c)}(t_{CR}^{(c,t)},0) \\
& + i\sqrt{\gamma_d}\hat{S}_x^{(t)}(t_{CR}^{(c,t)},0) + i\sqrt{\gamma_d}\hat{S}_y^{(t)}(t_{CR}^{(c,t)},0) + i\sqrt{\gamma_d}\hat{S}_z^{(t)}(t_{CR}^{(c,t)},0) \\
& + i\sqrt{\gamma_1^{(c)}}\hat{S}_1^{(c)}(t_{CR}^{(c,t)},0) + i\sqrt{\gamma_1^{(t)}}\hat{S}_1^{(t)}(t_{CR}^{(c,t)},0) + i\sqrt{\gamma_{pd}^{(c)}/4}\hat{S}_2^{(c)}(t_{CR}^{(c,t)},0) \\
& + i\sqrt{\gamma_{pd}^{(t)}/4}\hat{S}_2^{(t)}(t_{CR}^{(c,t)},0)\Bigg)\,.
\end{aligned} \tag{5.25}$$

Stochastic and deterministic matrices are similar to those of Eq. (5.17). For instance $\hat{S}_z^{(c)}(t,t_0) = \int_{t_0}^{t} \hat{Z}\hat{I}(s,t_0)\mathrm{d}s$. Their entries are deterministic or Itô integrals of trigonometric functions similar to Eq. (5.19).

5.2.3 Other noises

Noise gates corresponding to measurement errors and noises on idle qubits can be derived exactly as in [43]. The single-qubit bit flip Lindblad equation in Eq. (5.11) is unravelled to get the stochastic Schrödinger equation

$$\mathrm{d}|\psi_t\rangle = \left[i\sqrt{\gamma}\hat{X}\mathrm{d}W_t - \frac{\gamma}{2}\mathbb{1}\mathrm{d}t\right]|\psi_t\rangle \ . \tag{5.26}$$

Since $\hat{X}$ and $\mathbb{1}$ commute, the equation is analytically solvable with standard methods [20, 21, 36], and the corresponding noise gate is [43]

$$N^{\text{SPAM}}(t,t_0) = e^{i\sqrt{\gamma}\hat{X}W(t,t_0)}, \tag{5.27}$$

where $W(t,t_0) := \int_{t_0}^{t}\mathrm{d}W_s$ is a Wiener process. In this case, as $\hat{X}$ is Hermitian, the noise gate is unitary and we can interpret it as a stochastic Schrödinger evolution due to the presence of $W(t,t_0)$. The probability distribution of $W(t,t_0)$ is Gaussian with mean $\mathbb{E}[W(t,t_0)] = 0$ and variance $\mathbb{E}[W^2(t,t_0)] = t - t_0$.

The stochastic Schrödinger equation for the single-qubit amplitude and phase damping channel reads

$$\mathrm{d}|\psi_t\rangle = \left[i\sqrt{\gamma_1}\sigma^+\mathrm{d}W_{t,1} - \frac{\gamma_1}{2}\mathcal{P}_1\mathrm{d}t + i\sqrt{\frac{\gamma_{pd}}{4}}Z\mathrm{d}W_{t,2} - \frac{\gamma_{pd}}{8}\mathrm{d}t\right]|\psi_t\rangle \ . \tag{5.28}$$

Despite the fact that operators in Eq. (5.28) do not commute, the Itô equation is analytically solvable [43] and we get the following non-unitary noisy gate

$$N^{\text{relax}}(t,t_0) = \begin{pmatrix} e^{i\alpha W_2(t,t_0)} & iS(t,t_0)e^{i\alpha W_2(t,t_0)} \\ 0 & e^{-\frac{\gamma_1}{2}(t-t_0)}e^{-i\alpha W_2(t,t_0)} \end{pmatrix}, \tag{5.29}$$

where for simplicity we defined $\alpha := \sqrt{\gamma_{pd}/4}$, and

$$S(t,t_0) = \sqrt{\gamma_1}\int_{t_0}^{t} e^{-\frac{\gamma_1}{2}(s-t_0)}e^{-2i\alpha W_2(s,t_0)}\mathrm{d}W_{s,1} \tag{5.30}$$

is a complex stochastic Itô process. The sampling of this term is problematic. For instance, its real part

$$S_R(t,t_0) = \sqrt{\gamma_1}\int_{t_0}^{t} e^{-\frac{\gamma_1}{2}(s-t_0)}\cos\Big(2\alpha W_2(s,t_0)\Big)\mathrm{d}W_{s,1}; \tag{5.31}$$

is an Itô integral of a stochastic function, and, as commented in Chapter 4, its probability distribution is not known. We can avoid such a difficulty by adequately substituting $N^{\text{relax}}(t,t_0)$ with some modified noise gate, which is equivalent to the former once the average is carried out, in the sense that Eq. (5.2) still holds even if the new noise gate is not a solution of the unraveling in Eq. (5.28) anymore. For instance, it is straightforward to verify that this holds for the following choice

$$\tilde{N}^{\text{relax}}(t,t_0) = \begin{pmatrix} e^{i\alpha W_2(t,t_0)} & i\tilde{S}(t,t_0)e^{-i\alpha W_2(t,t_0)} \\ 0 & e^{-\frac{\gamma_1}{2}(t-t_0)}e^{-i\alpha W_2(t,t_0)} \end{pmatrix}, \tag{5.32}$$

with the definition

$$\tilde{S}(t,t_0) = \sqrt{\gamma_1}\int_{t_0}^{t} e^{-\frac{\gamma_1}{2}(s-t_0)}\mathrm{d}W_{s,1}; \tag{5.33}$$

i.e., one always has that

$$\mathbb{E}\left[N^{\text{relax}}\left|\psi\right\rangle\left\langle\psi\right|N^{\text{relax}\dagger}\right] = \mathbb{E}\left[\tilde{N}^{\text{relax}}\left|\psi\right\rangle\left\langle\psi\right|\tilde{N}^{\text{relax}\dagger}\right]. \tag{5.34}$$

The difference is that now the process $\tilde{S}(t,t_0)$ is the Itô integral of a deterministic function, and it has a Gaussian statistics [20], making its sampling more convenient in a simulation.

5.3 Comparison with the numerical solution of Lindblad equations

We study the performances of the noisy gates method, and compare them with the standard method. First, we test which of the two approaches is closer to the analytic solution of the full Lindblad equation as in Eq. (2.15). We run the simulations on both single and two qubit gates. In particular, we simulate repetitions of X, CR and CNOT gates modified by the standard noise model described in section 5.1. For the standard approach we used Qiskit's simulator [44], while for the noisy gates simulations we used the simulator provided by the QUANTUM-GATES package.

We compare the density matrices ρ^{ng} and ρ^{ibm}, obtained from the noisy gates simulation and from the Qiskit simulation respectively, with the target density matrix σ obtained by solving numerically the Lindblad equation with Mathematica [45]. We treat σ as the target analytic solution of the full Lindblad equation. The comparison is performed with the Hellinger distances $\mathcal{H}_\sigma^{\text{ng}} = \mathcal{H}(\rho^{\text{ng}},\sigma)$, $\mathcal{H}_\sigma^{\text{ibm}} = \mathcal{H}(\rho^{\text{ibm}},\sigma)$ where the Hellinger distance is defined by

$$\mathcal{H}(\rho,\sigma) = \frac{1}{\sqrt{2}}\sqrt{\sum_{k=1}^{N}\left(\sqrt{\rho_{kk}}-\sqrt{\sigma_{kk}}\right)^2}, \tag{5.35}$$

with ρ_{kk} (σ_{kk}) the diagonal elements of ρ (σ). The Hellinger distance is a classical measure of the distance between the readout probability distributions. It cannot be interpreted as a distance between quantum states since it does not take in account off diagonal elements of density matrices. The Hellinger distance directly compares the concrete outputs of a real device, which are the outcomes of Z measurements, i.e. classical bitstrings. Since in these simulations it is easy to get the full density matrices, we also compute the fidelities, which accounts for all the entries of density matrices, $\mathcal{F}_\sigma^{\rm ng} = \mathcal{F}(\rho^{\rm ng}, \sigma)$ and $\mathcal{F}_\sigma^{\rm ibm} = \mathcal{F}(\rho^{\rm ibm}, \sigma)$, where the fidelity is defined as

$$\mathcal{F}(\rho, \sigma) = \left(\mathrm{Tr}\sqrt{\sigma^{1/2}\rho\sigma^{1/2}}\right)^2 . \tag{5.36}$$

We notice that for the diagonal entries of density matrices, we could have used the Hellinger fidelity, related to the Hellinger distance as $\mathcal{F}_H = (1 - \mathcal{H}^2)^2$. This quantity is not a proper mathematical distance, further motivating the use of the Hellinger distance as a more reliable figure of merit.

5.3.1 Single qubit simulations

The X gates are obtained by setting $\theta = \pi$ and $\phi = 0$ in Eq. (5.13); we initialize the qubit in $|0\rangle$ and we use the qubit noise parameters of ibmq_manila. We evolve the state of the qubit for a time $T = \mathcal{N} t_g$, with $\mathcal{N} = 15000$. In panels (a), (b) and (c) of Fig. 5.1 we plot the time evolution of $\rho_{00} = \langle 0|\rho|0\rangle$, the population of the ground state, obtained with the three methods. In the noiseless case, ρ_{00} should oscillate between zero and one as at each t_g a complete X rotation is performed; the standard noise model modifies this behaviour: oscillations are damped due to amplitude and phase damping, while depolarization drives probabilities towards the asymptotic value $\rho_{00} \to 0.5$.

Both the noisy gates simulation and that obtained using Qiskit qualitatively reproduce this behaviour. In Fig. 5.1 we have also highlighted with vertical dashed lines the characteristic times of amplitude damping and depolarization; for times approaching these values the state is not a reliable quantum state anymore, as the density matrix becomes completely mixed. Given this consideration, in the plots in Fig. 5.2 we stop at $\mathcal{N} = 2000$.

To quantify the accuracy of the methods, we have run 100 independent simulations, each with 1000 samples, with both the noisy gates simulator and the Qiskit simulator, computing for each simulation the Hellinger distance $\mathcal{H}_\sigma^{\rm ng}$, $\mathcal{H}_\sigma^{\rm ibm}$. We computed the means over the 100 independent simulations, $\bar{\mathcal{H}}_\sigma^{\rm ng}$, $\bar{\mathcal{H}}_\sigma^{\rm ibm}$ and their standard deviations $\Delta\mathcal{H}_\sigma^{\rm ng}$, $\Delta\mathcal{H}_\sigma^{\rm ibm}$. These quantities are shown in panels (a), (b) and (c) of Fig. 5.2. During the relevant time interval $[0, T]$ $\bar{\mathcal{H}}_\sigma^{\rm ng}$ is closer to zero than $\bar{\mathcal{H}}_\sigma^{\rm ibm}$. Results are compatible within the error bars, however the standard deviations associated to the noisy gates simulations are significantly smaller than those associated to

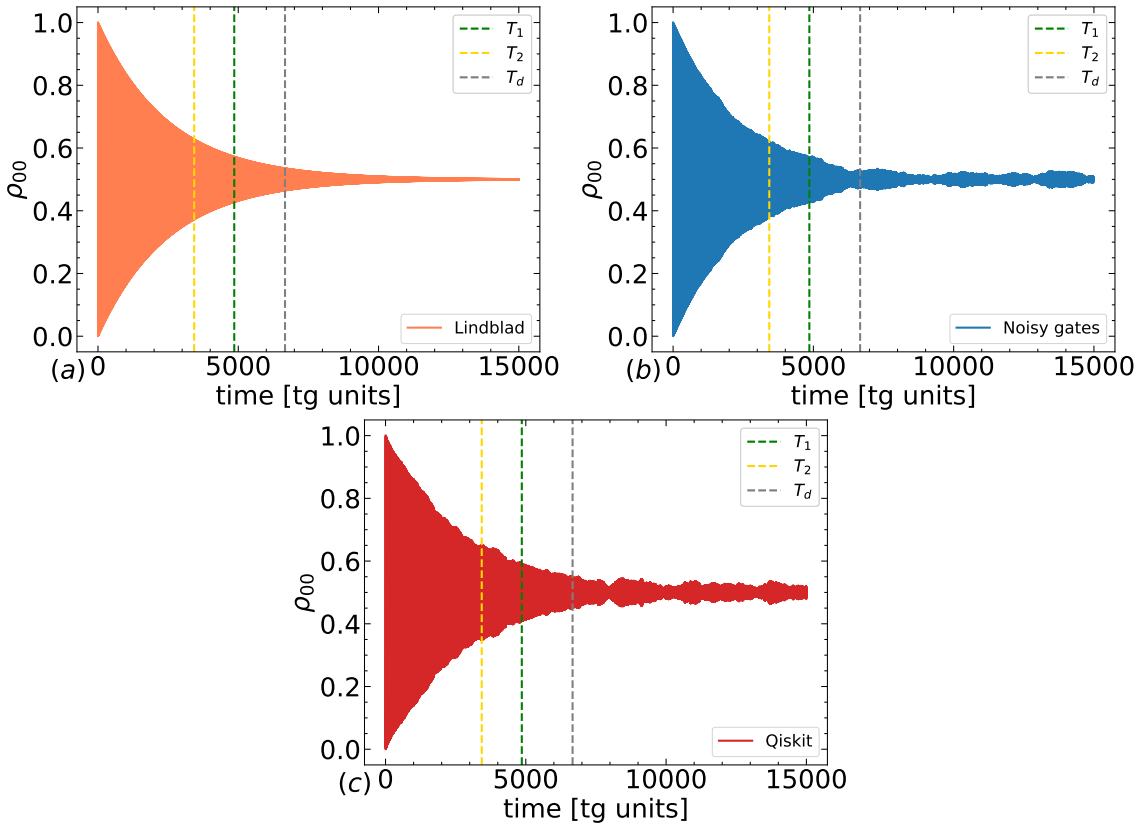

Figure 5.1: Repetition of X gates. Panels (a), (b), (c) show the time evolution of the $\rho_{00} = \langle 0|\rho|0\rangle$ entry of the density matrix. The numerical solution of the Lindblad equation is displayed in orange (a), that of the noisy gates simulation in blue (b), and that of the Qiskit simulation in red (c). The noisy gates and Qiskit simulations are obtained with 1000 samples, and qualitatively they reproduce the time evolution of the Lindblad equation. Vertical dashed lines in the three panels represent the time scales of relaxation T_1 (green), T_2 (yellow) and depolarization T_d (grey).

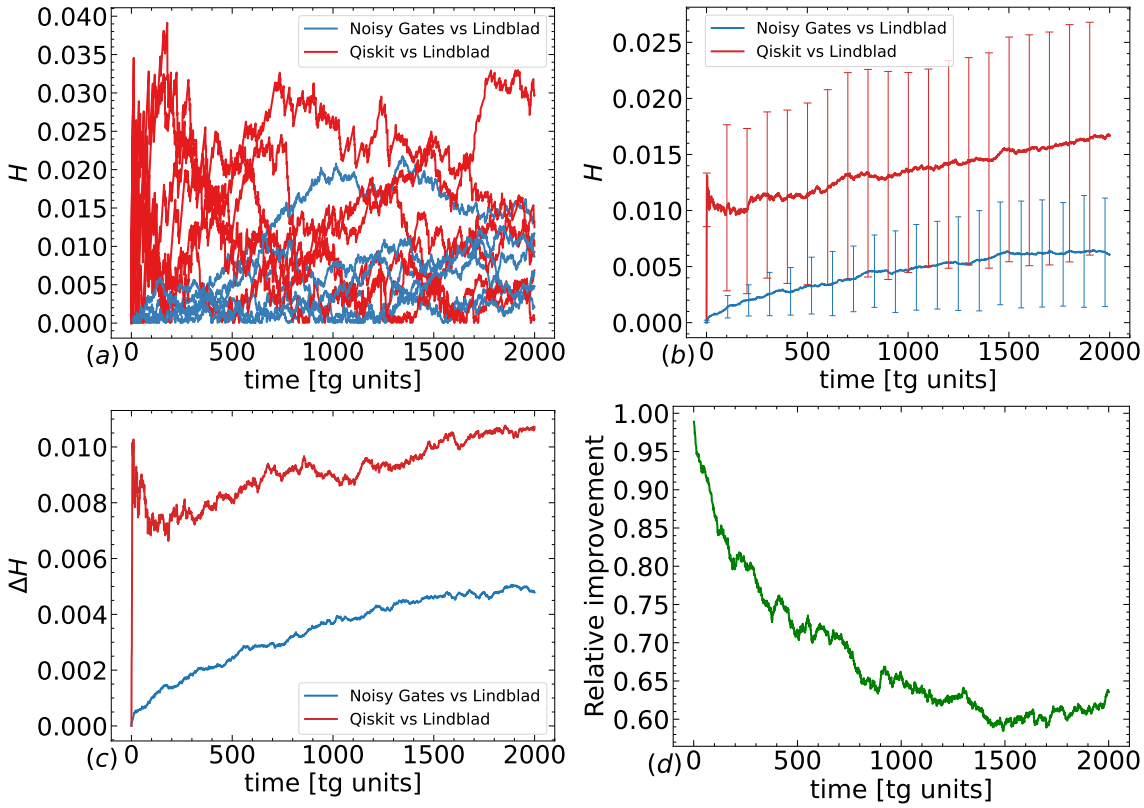

Figure 5.2: Repetition of X gates. Panel (a) shows the Hellinger distances $\mathcal{H}_\sigma^{\rm ng}$, in blue, and $\mathcal{H}_\sigma^{\rm ibm}$, in red, as a function of time. Different curves are obtained from 100 independent runs of the two methods (for better readability only five are shown), where each simulation is obtained by averaging over 1000 samples. Panel (b) shows the mean of the Hellinger distances $\bar{\mathcal{H}}_\sigma^{\rm ng}$, and $\bar{\mathcal{H}}_\sigma^{\rm ibm}$, obtained from the 100 independent runs, and vertical error bars show their standard deviations $\Delta\mathcal{H}_\sigma^{\rm ng}$, $\Delta\mathcal{H}_\sigma^{\rm ibm}$. Panel (c) displays $\Delta\mathcal{H}_\sigma^{\rm ng}$ and $\Delta\mathcal{H}_\sigma^{\rm ibm}$ as functions of time. Panel (d) shows the relative improvement of the distance $\bar{\mathcal{H}}_\sigma^{\rm ng}$ with respect to $\bar{\mathcal{H}}_\sigma^{\rm ibm}$, calculated as $|\bar{\mathcal{H}}_\sigma^{\rm ibm} - \bar{\mathcal{H}}_\sigma^{\rm ng}|/\bar{\mathcal{H}}_\sigma^{\rm ibm}$. The fact that noises drive the system towards the maximally mixed state is the reason why the improvement decreases in time. The noisy gates and the standard approaches lead to the same predictions when one is close to decoherence times, as the noise is dominant over the unitary evolution. In the interesting regime $[0, 2000 \cdot t_g]$ before deoherence dominates, the improvement is always above 60%.

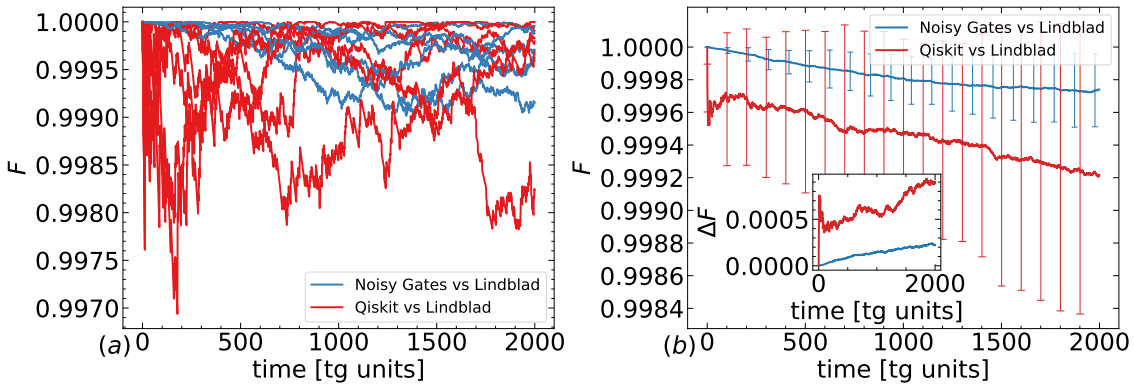

Figure 5.3: Fidelities $\mathcal{F}_\sigma^{\rm ng}$, in blue, and $\mathcal{F}_\sigma^{\rm ibm}$, in red, as a function of time, for a repetition of X gates. On panel (a), the fidelities obtained from 100 independent runs of the two methods are pictured (for better readability only five are shown), where each simulation is obtained by averaging over 1000 samples. On panel (b), the means $\bar{\mathcal{F}}_\sigma^{\rm ng}$, $\bar{\mathcal{F}}_\sigma^{\rm ibm}$ of the same simulations and their standard deviations $\Delta\mathcal{F}_\sigma^{\rm ng}$, $\Delta\mathcal{F}_\sigma^{\rm ibm}$ are displayed. The inset shows the standard deviations $\Delta\mathcal{F}_\sigma^{\rm ng}$, $\Delta\mathcal{F}_\sigma^{\rm ibm}$ as functions of time.

the Qiskit simulations, as also highlighted in Fig. 5.2 (c). This means that the noisy gates have the additional advantage that a smaller number of samples is needed to reach a target precision. We notice that the difference between $\bar{\mathcal{H}}_\sigma^{\rm ng}$ and $\bar{\mathcal{H}}_\sigma^{\rm ibm}$ is of the order $\sim 10^{-3} - 10^{-2}$, and this corresponds to a relative improvement, calculated as $|\bar{\mathcal{H}}_\sigma^{\rm ibm} - \bar{\mathcal{H}}_\sigma^{\rm ng}|/\bar{\mathcal{H}}_\sigma^{\rm ibm}$, in the range from 90% to 60% as time increases. The relative improvement is shown in Fig. 5.2 (d). The fact that noises drive the system towards the maximally mixed state is the reason why the improvement decreases over time. The noisy gates and the standard approaches lead to the same predictions when approaching decoherence times. Indeed after such times the strength of the noise is dominant over the unitary evolution, or, equivalently, the Hamiltonian contribution is negligible with respect to the Lindblad term (see Eq. (5.9)). In the interesting regime $[0, T]$ our improvement is always above 60%. We repeat the same analysis for the fidelities. Results are shown in Fig. 5.3 (a) and (b). Panel (a) shows the fidelities obtained from 100 independent simulations with the two methods (for better readability only five are shown). Panel (b) shows the means $\bar{\mathcal{F}}_\sigma^{\rm ng}$, $\bar{\mathcal{F}}_\sigma^{\rm ibm}$ of the same simulations and their standard deviations $\Delta\mathcal{F}_\sigma^{\rm ng}$,$\Delta\mathcal{F}_\sigma^{\rm ibm}$. Results on the fidelities are in accordance with those in Fig. 5.2.

5.3.2 Two qubits simulations

We simulate a repetition of CR gates in Eq. (5.22), choosing $\phi = 0$ and $\theta = \pi$. We initialize the system in the state $|10\rangle$ and we use the qubits noise parameters of ibmq_manila. In the three panels of Fig. 5.4 we show the time evolution of the entry $\rho_{22} = \langle 10|\rho|10\rangle$; the x-axis is normalized in terms of the CR gate time t_{CR}. The two-qubit state goes asymptotically towards the completely mixed state as ρ_{22} reaches the asymptotic value 0.25. The probability ρ_{22}, which in the ideal case should flip between one and zero, is damped over time by amplitude and phase damping effects. Vertical dashed lines signal the characteristic time scales of the noises. We plot only the T_1 and T_2 values of the target qubit as representative values. Depolarization is the dominant contribution, spoiling the quantum state already after ~ 100 CR gates; for this reason, in Fig. 5.5 we consider a total duration corresponding to $\mathcal{N} \sim 100$. Panels (a), (b) and (c) of Fig. 5.5 report the Hellinger distances, showing the different results of 100 independent simulations together with their means and standard deviations.

Within the relevant time interval $[0, T]$ $\bar{\mathcal{H}}_\sigma^{\rm ng}$ is closer to zero than $\bar{\mathcal{H}}_\sigma^{\rm ibm}$. Notably, the two results are not compatible within error bars: the difference between $\bar{\mathcal{H}}_\sigma^{\rm ng}$ and $\bar{\mathcal{H}}_\sigma^{\rm ibm}$ is now of the order $\sim 10^{-1}$. This corresponds to a relative improvement in the range from 90% to 88% as time increases, shown in Fig. 5.5 (d). In the interesting regime $[0, T]$ our improvement is always above 88%. As noises dominate approaching decoherence times, in Fig. 5.5 (b) the value of $\bar{\mathcal{H}}_\sigma^{\rm ibm}$ approaches that of $\bar{\mathcal{H}}_\sigma^{\rm ng}$ for times close to 100 CR gate times. We report the results of the same analysis for the fidelities in Fig. 5.6, showing accordance with the results in Fig. 5.5.

We perform a similar analysis for a repetition of CNOT gates, for an initial state given by $|10\rangle$ and qubits noise parameters of ibmq_quito. In this simulation we implement each CNOT gate directly without expressing it as a combination of single qubit gates and CR gates, as in IBM devices. We make this choice to solve numerically the target Lindblad equation more easily. Effectively, at each CNOT gate time we simulate a circuit with an increasing number of CNOT gates, where we add measurements at the end of the circuit. Thus, according to the standard noise model, we add the single-qubit bitflip channel (see 5.2.3) to model measurements errors. This allows to extend this analysis to runs on real hardware in section 5.4, that of course involve measurements. For that same reason, we do not compute the fidelities, as the output of the quantum device is a classical probability distributions for the bitstrings.

In the three panels of Fig. 5.7 we show the time evolution of the $\rho_{22} = \langle 10|\rho|10\rangle$ entry of the density matrix. The relevant time interval is given by a total duration of $\mathcal{N} \sim 100$ gates: depolarization spoils the quantum state after ~ 120 CNOT gates. Fig. 5.8 (a) shows the mean of the Hellinger distances $\bar{\mathcal{H}}_\sigma^{\rm ng}$ (in blue) and $\bar{\mathcal{H}}_\sigma^{\rm ibm}$ (in red) and their standard deviations $\Delta\mathcal{H}_\sigma^{\rm ng}$ and $\Delta\mathcal{H}_\sigma^{\rm ibm}$, also shown in Fig. 5.8 (b). In the time interval $[0, T]$ $\bar{\mathcal{H}}_\sigma^{\rm ng}$ is closer to zero than $\bar{\mathcal{H}}_\sigma^{\rm ibm}$ and their difference is of the

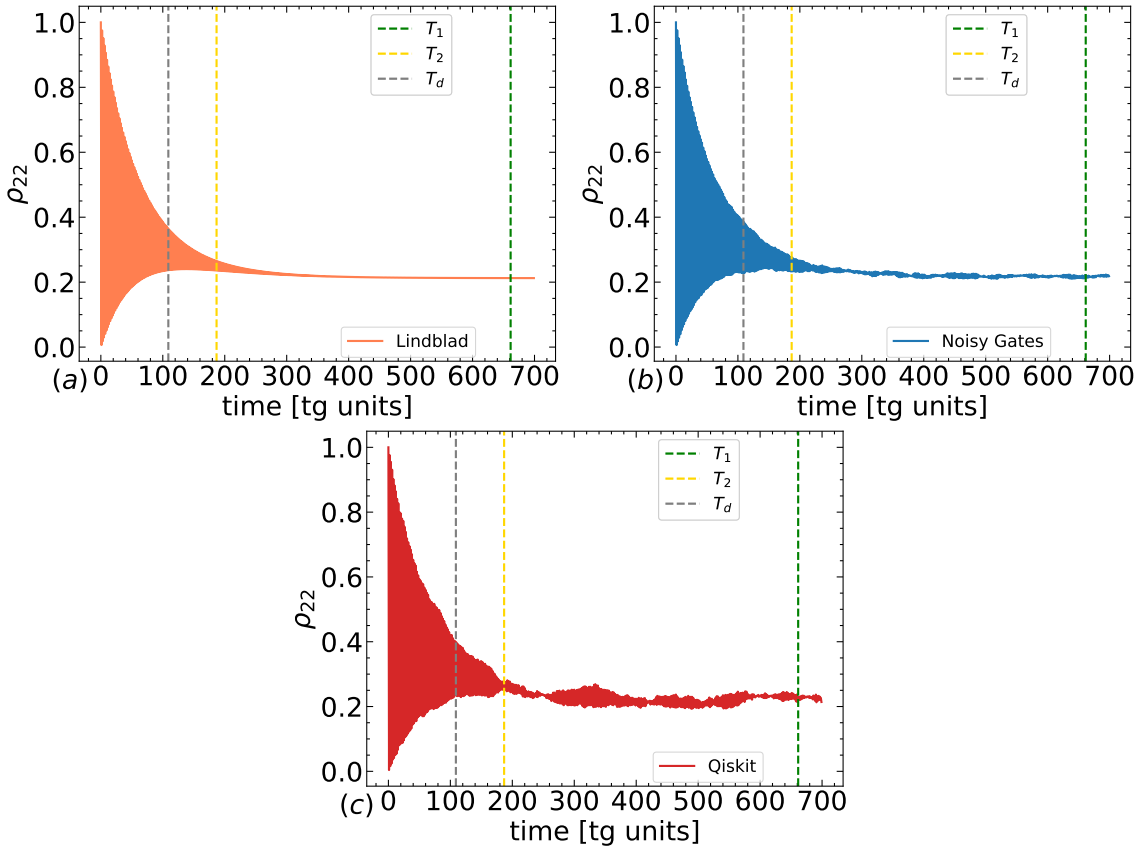

Figure 5.4: Repetition of CR gates. Panels (a), (b), (c) show the time evolution of the ρ_{22} entry of the density matrix for the CR gate with $\theta = \pi$ and $\phi = 0$. Colors have the same meaning as for Fig. 5.1. Vertical dashed lines represent the time scales of relaxation, T_1 (in green) and T_2 (in yellow) of the target qubit, and depolarization T_d (grey). The noisy gates simulations reproduce qualitatively better the time evolution obtained from the direct numerical solution of the Lindblad equation.

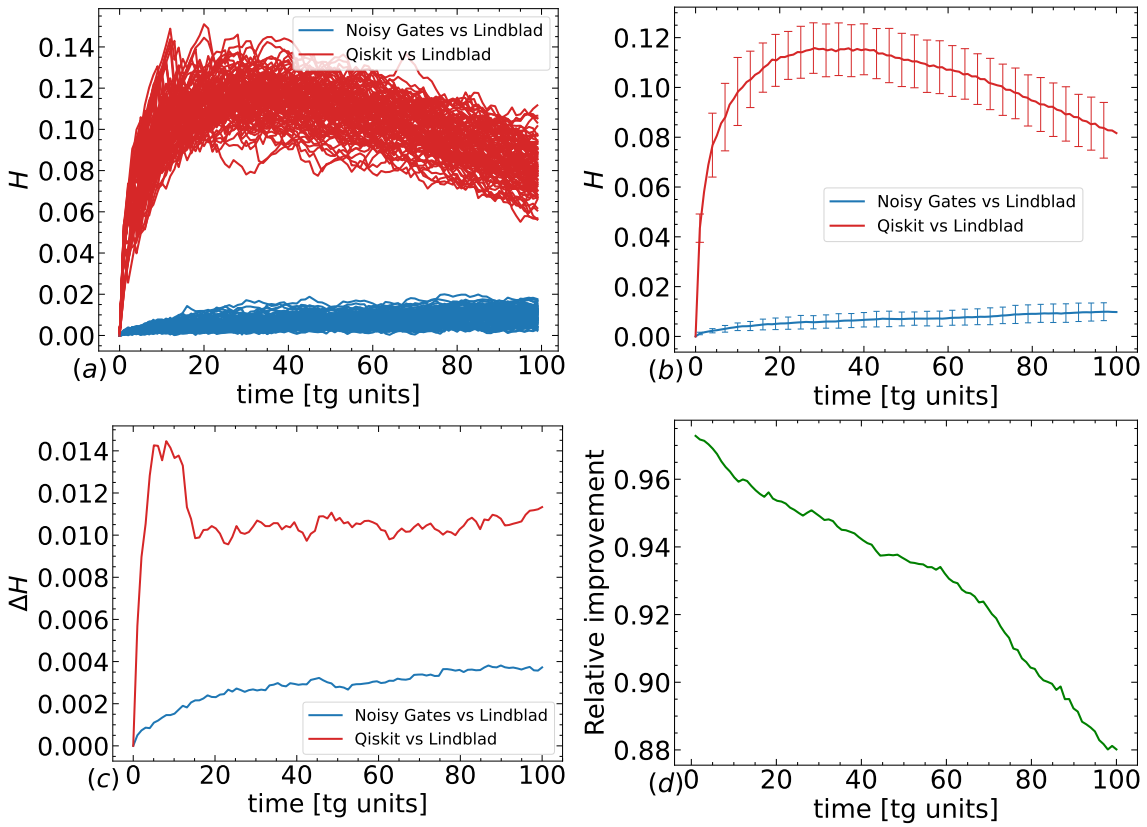

Figure 5.5: Repetition of CR gates. Panels (a) and (b) display the Hellinger distances $\mathcal{H}_\sigma^{\rm ng}$, in blue, and $\mathcal{H}_\sigma^{\rm ibm}$, in red, as a function of time. The plots have the same meaning as for Fig. 5.2. Panel (d) shows the relative improvement of the distance $\bar{\mathcal{H}}_\sigma^{\rm ng}$ with respect to $\bar{\mathcal{H}}_\sigma^{\rm ibm}$, calculated as $|\bar{\mathcal{H}}_\sigma^{\rm ibm} - \bar{\mathcal{H}}_\sigma^{\rm ng}|/\bar{\mathcal{H}}_\sigma^{\rm ibm}$. The fact that noises drive the system towards the maximally mixed state is the reason why the improvement decreases in time. The noisy gates and the standard approaches lead to the same predictions when one is close to decoherence times, as the noise is dominant over the unitary evolution. In the interesting regime $[0, 100 \cdot t_g]$ our improvement is always above 88%.

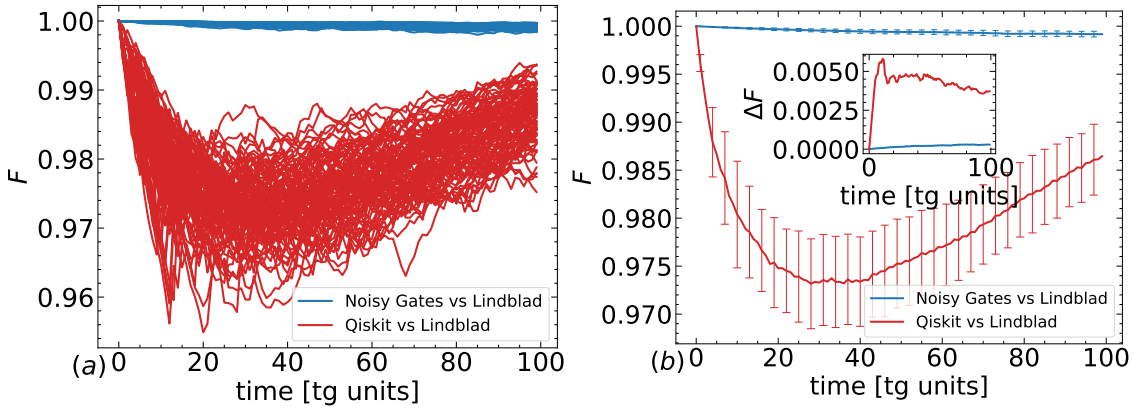

Figure 5.6: Fidelities $\mathcal{F}_\sigma^{\text{ng}}$, in blue, and $\mathcal{F}_\sigma^{\text{ibm}}$, in red, as a function of time, for a repetition of CR gates. Panels (a) and (b) have the same meaning as for Fig. 5.3.

order $\sim 10^{-2}$. This corresponds to a relative improvement in the range from 80% to 55% as time increases. This is shown in Fig. 5.8 (c).

By looking at Figs. 5.5 (d) and 5.8 (c), we notice that the improvement in the Hellinger distance gained by using the noisy gates approach is much higher for CR gates with respect to CNOT gates. We clarify this fact in Fig. 5.9. Panels (a), (b) show the time evolution of the ρ_{11} entry of the density matrix for the CR gates and panels (c) and (d) show the time evolution of ρ_{11} for the CNOT gates. Similarly to the convention used above, orange curves are obtained with the numerical solution of the Lindblad equation, blue curves are obtained with the noisy gates simulations and red curves are obtained with Qiskit simulations. The noisy gates simulations make good predictions for both gate sequences, as the blue curves follow closely the orange curves. On the other hand, the Qiskit simulation for the CR gates is visibly different from the numerical solution of the Lindblad equation. This might be due to the fact that the CR gate is a block diagonal matrix with $X(\theta)$ in the upper block and $X(-\theta)$ in the lower block while the CNOT gate is block diagonal with an identity in the upper block and $X(\theta)$ in the lower block. The identity in the CNOT might lead to a lower influence of noises on the ρ_{00} and ρ_{11} entries of the density matrix. Thus, Hellinger distances obtained with the noisy gates in different simulations are very good and similar to each other, while the Hellinger distance obtained with Qiskit is better for the CNOT with respect to the CR. Nevertheless, the noisy gates approach always significantly outperforms the standard method, as shown by the relative improvements.

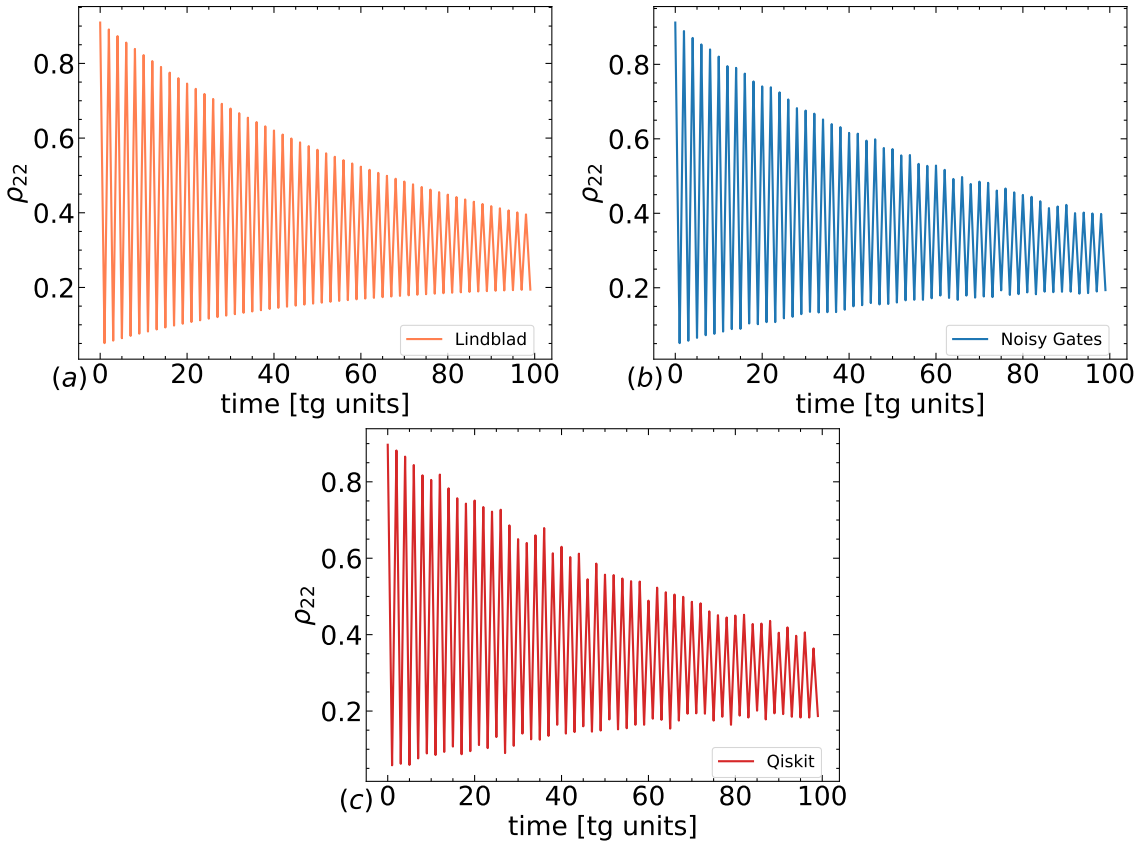

Figure 5.7: Repetition of CNOT gates. Panels (a), (b), (c) show the time evolution of the ρ_{22} entry of the density matrix for the CNOT gate. Colors have the same meaning as for Fig. 5.1. The noisy gates simulations reproduce qualitatively better the time evolution obtained from the direct numerical solution of the Lindblad equation.

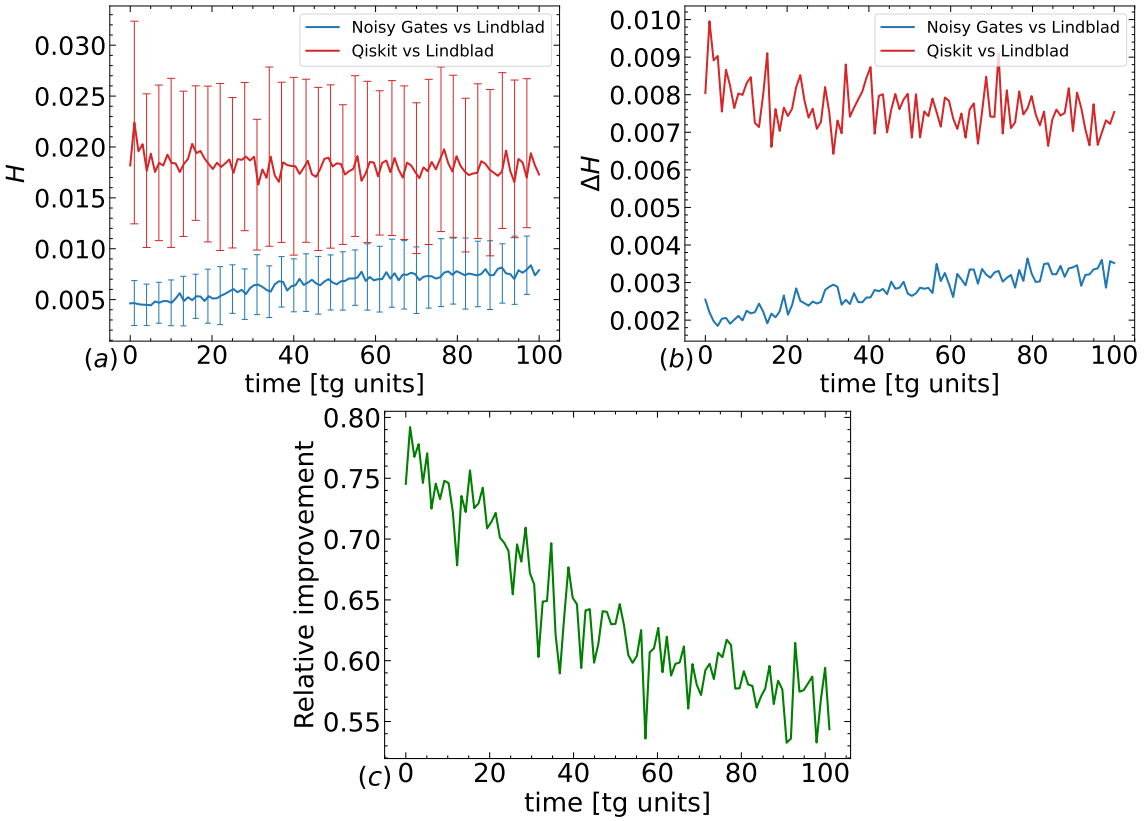

Figure 5.8: Repetition of CNOT gates. Panel (a) and (b) displays mean of the Hellinger distances $\bar{\mathcal{H}}_\sigma^{\mathrm{ng}}$, in blue, and $\bar{\mathcal{H}}_\sigma^{\mathrm{ibm}}$, in red, and their standard deviations as functions of time. Panel (c) shows the relative improvement. The fact that noises drive the system towards the maximally mixed state is again the reason why the improvement decreases in time: the noisy gates and the standard approaches lead to the same predictions when one is close to decoherence times, as the noise is dominant over the unitary evolution. In the interesting regime $[0, 100 \cdot t_g]$ our improvement is always above 55%.

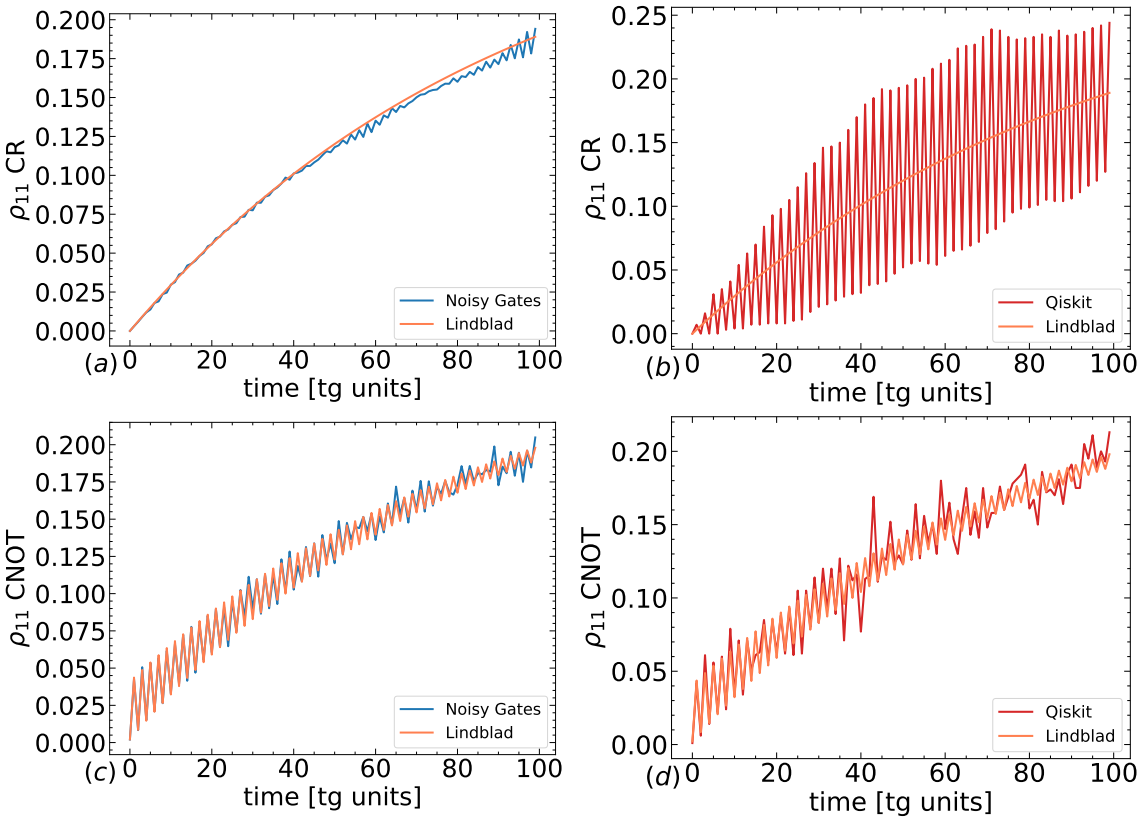

Figure 5.9: Repetition of CNOT gates. Panels (a), (b) show the time evolution of the ρ_{11} entry of the density matrix for the same sequence of CR gates in Fig. 5.5 and panels (c), (d) show the time evolution of the ρ_{11} entry of the density matrix for the sequence of CNOT gates. Colors have the same meaning as for Fig. 5.1. For the CR gates, the Qiskit simulation of ρ_{11} is visibly different from the Lindblad evolution, thus explaining the higher improvement of the noisy gates simulation in the Hellinger distance in Fig. 5.5.

5.4 Comparison with the behaviour of real quantum computers

We inspect the performances of the noisy gates approach when trying to reproduce the behaviour of a real quantum computer. To this purpose, we first extend the analysis of the CNOT gates sequence in section 5.3, and then we focus on the inverse Quantum Fourier Transform ($\mathrm{QFT}^\dagger$) algorithm. When dealing with a real hardware, we must take into account that the standard noise model we are using (see section 5.1) might not be accurate enough in describing the device, and that different quantum devices might behave very differently from one another. We show that, despite the choice of a simple noise model and the instability of ibmq devices, our approach is still able to outperform the standard one also when compared with the real hardware.

5.4.1 CNOT simulations

We run the sequence of CNOT gates of section 5.3 on ibmq_quito, available on the cloud and comprising 7 superconducting transmon qubits to get the diagonal entries of the density matrix χ of the physical device, to be compared with the diagonal entries of the density matrices ρ^{ng}, ρ^{ibm} and σ obtained for the CNOT simulations in section 5.3. We remark again that in section 5.3, we implemented each CNOT gate directly without expressing it as a combination of single qubit gates and CR gates, because in this way it is easier to solve numerically the target Lindblad equation. We create a list of circuits, each consisting of an increasing number of CNOT gates, and measure each circuit 1000 times to obtain the output probability distributions, thus deriving the evolution of the outcome probabilities as the number of gates increases. As noted above, each circuit involves measurements that add noise, explaining why in the simulations we added a single-qubit bitflip channel. The Hellinger distance $\mathcal{H}_\sigma^\chi = \mathcal{H}(\chi, \sigma)$ between the Lindblad evolution and the evolution obtained with ibmq_quito is shown in Fig. 5.10 (a). This distance is three to tens time larger with respect to $\bar{\mathcal{H}}_\sigma^{\mathrm{ng}}$ and $\bar{\mathcal{H}}_\sigma^{\mathrm{ibm}}$ in Fig. 5.8 (a). While the standard approach and the noisy gates approach have a certain level of agreement with the Lindblad equation, the latter is deviating from the quantum hardware by a significantly higher level. This is also the reason why it is not possible to appreciate the difference between the mean Hellinger distance $\bar{\mathcal{H}}_\chi^{\mathrm{ng}} = \bar{\mathcal{H}}(\rho^{\mathrm{ng}}, \chi)$ between the noisy gates and ibmq_quito, and the mean Hellinger distance $\bar{\mathcal{H}}_\chi^{\mathrm{ibm}} = \bar{\mathcal{H}}(\rho^{\mathrm{ibm}}, \chi)$ between Qiskit and ibmq_quito, as shown in Fig. 5.10 (b) and Fig. 5.10 (c). Fig. 5.10 (d) shows the relative improvement with respect to the device, calculated as $|\bar{\mathcal{H}}_\chi^{\mathrm{ibm}} - \bar{\mathcal{H}}_\chi^{\mathrm{ng}}|/\bar{\mathcal{H}}_\chi^{\mathrm{ibm}}$. The relative improvement is around 10%. The smaller relative improvement with respect to those shown in the previous section is only to a small extent due to the fact that we do not decompose

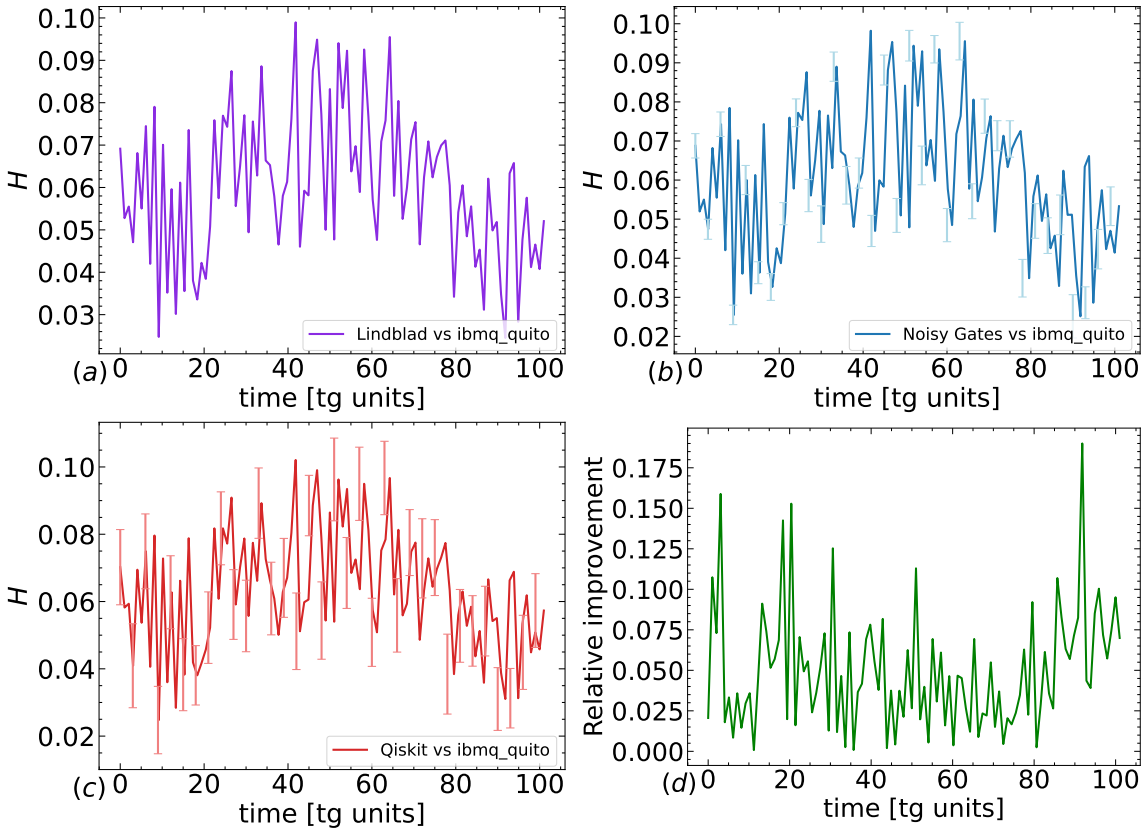

Figure 5.10: Repetition of CNOT gates. Panel (a) shows the Hellinger distance $\mathcal{H}_\sigma^\chi$ between the Lindblad evolution and ibmq_quito for the repetition of CNOT gates. Panel (b) shows the mean Hellinger distance $\bar{\mathcal{H}}_\chi^{\rm ng}$ and the standard deviations between the noisy gates simulation and ibmq_quito. Panel (c) shows the mean Hellinger distance $\bar{\mathcal{H}}_\chi^{\rm ibm}$ and the standard deviations between the Qiskit simulation and ibmq_quito. Panel (d) shows the relative improvement calculated as $|\bar{\mathcal{H}}_\chi^{\rm ibm} - \bar{\mathcal{H}}_\chi^{\rm ng}|/\bar{\mathcal{H}}_\chi^{\rm ibm}$. The relative improvement is around 10%. The smaller relative improvement with respect to those shown in the previous figures, is mainly due to additional noises present in ibmq devices, i.e. crosstalks, correlated noises and coherent errors.

CNOT gates. The main reason, as we explain when discussing the simulations of the QFT (see below), is that additional noises are present in ibmq devices, i.e. crosstalks, correlated noises and coherent errors [46,47]. The simple noise model that we consider does not take such noises into account and the Lindblad solution is far from the real quantum computer.

5.4.2 QFT simulations

The $\mathrm{QFT}^\dagger$ is a subroutine of many important quantum algorithms, such as the Shor's algorithm [48, 49] or Quantum Phase Estimation. The $\mathrm{QFT}^\dagger$ circuit for n qubits is readily extendable to $n+1$ qubits, allowing to efficiently test the robustness of the simulation approaches as the circuit's width and depth increase. We run $\mathrm{QFT}^\dagger$ for $n = 2, \ldots, 5$ on ibm_oslo and for $n = 2, \ldots, 8$ on ibmq_kolkata. These devices are available on the cloud, comprising respectively 7 and 27 superconducting transmon qubits. We set as input of $\mathrm{QFT}^\dagger$ the state $|+\rangle^{\otimes n}$, obtained by applying a layer of Hadamard gates on each qubit initialized in $|0\rangle$. In this way the ideal output of $\mathrm{QFT}^\dagger$ is $|0\rangle^{\otimes n}$. Runs on real quantum computers are performed by taking 1000 shots, i.e. measurements. The $\mathrm{QFT}^\dagger$ circuit is transpiled into the native gate set to run on ibmq devices. Now, all CNOT gates inside the circuits are decomposed in terms of single-qubit and CR gates.

The performance of different approaches in simulating the behaviour of the quantum computer are measured with the Hellinger distances from the outcomes of the real device. This allows to avoid full state tomography to reconstruct the full density matrices, which scales exponentially with the number of qubits and becomes unfeasible for the current simulations.

We have run 100 independent simulations, each including 1000 samples, for both methods and for each n. In Fig. 5.11 (a) we plot the average values of $\bar{\mathcal{H}}_\chi^{\mathrm{ng}} = \bar{\mathcal{H}}(\rho^{\mathrm{ng}}, \chi)$, $\bar{\mathcal{H}}_\chi^{\mathrm{ibm}} = \bar{\mathcal{H}}(\rho^{\mathrm{ibm}}, \chi)$ as the number of qubits n increases from 2 to 5. The diagonal elements of χ are the outcome probabilities of ibm_oslo. Fig. 5.12 (a) displays again the average values of $\bar{\mathcal{H}}_\chi^{\mathrm{ng}} = \bar{\mathcal{H}}(\rho^{\mathrm{ng}}, \chi)$, $\bar{\mathcal{H}}_\chi^{\mathrm{ibm}} = \bar{\mathcal{H}}(\rho^{\mathrm{ibm}}, \chi)$ up to 8 qubits, where the diagonal elements of χ come from ibmq_kolkata. In Fig. 5.12 (c) we compute again $\mathcal{H}_\chi^{\mathrm{ng}}$, $\mathcal{H}_\chi^{\mathrm{ibm}}$ to test the stability of ibmq_kolkata in different runs. Only for Fig. 5.12 (c) we have run a single simulation of 1000 samples, thus standard deviations are not present. We notice that for every n and device we get $\bar{\mathcal{H}}_\chi^{\mathrm{ng}} < \bar{\mathcal{H}}_\chi^{\mathrm{ibm}}$ and $\Delta\mathcal{H}_\chi^{\mathrm{ng}} < \Delta\mathcal{H}_\chi^{\mathrm{ibm}}$. The relative improvements, shown in green in Fig. 5.11 (b) and Figs. 5.12 (b), (d), changes significantly between different devices and also for the same device but in different runs, namely with different noise parameters, meaning that the performances of such devices are not very stable. For example at $n = 3$, in panel (b) of Fig. 5.11 the relative improvement is $\sim 25\%$, in panel (b) of Fig. 5.12 it is $\sim 5\%$ and in panel (d) of Fig. 5.12 it is $\sim 25\%$. The highest relative improvement

obtained with the runs on ibm_oslo is $\sim 30\%$ and for runs on ibmq_kolkata is $\sim 35\%$. As a final remark, we stress that we obtain better results with respect to Qiskit, despite the fact that we have chosen a rectangular pulse shape in the Hamiltonians (see Eqs. (5.12) and (5.13)), while gates on real hardware are realized using Gaussian pulses. We refer the reader to [41] for further analysis, including results for higher numbers of qubits and for the GHZ algorithm.

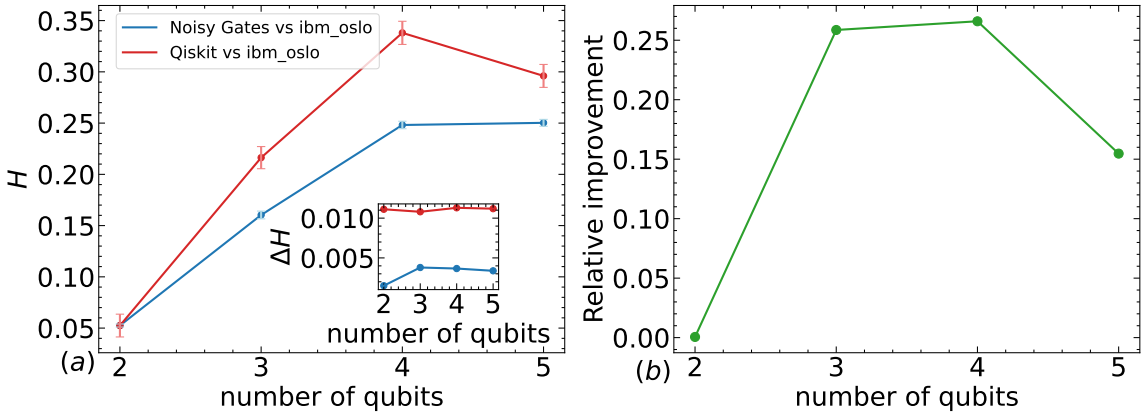

Figure 5.11: Quantum Fourier Transform. Panel (a) shows the Hellinger distances between the noisy gate approach and ibm_oslo, and between the Qiskit simulator and ibm_oslo, when executing the $\mathrm{QFT}^\dagger$ algorithm for $n = 2, \ldots, 5$ qubits. Each value is the mean of 100 independent simulations for the noisy gates, in blue, and for the Qiskit simulations, in red. The inset shows the standard deviations as functions of the number of qubits. Panel (b) shows the relative improvement, calculated as $|\bar{\mathcal{H}}_\chi^{\mathrm{ibm}} - \bar{\mathcal{H}}_\chi^{\mathrm{ng}}|/\bar{\mathcal{H}}_\chi^{\mathrm{ibm}}$.

5.5 Discussion

We have tested the noisy gates approach designed on IBM superconducting devices. We have shown that our approach is very successful in simulating the Lindblad dynamics, with a relative improvement between 50% and 90% and more, compared with the standard method, see Sec. 3.1 and Sec. 3.1.1.

When compared against real quantum devices, the improvement is lower and it fluctuates between 10% and 30%; this is largely due the underlying standard noise model being too simple to accurately represent the dynamics of the device. This is not a weakness of the noisy gate approach, but of the underlying standard noise model.

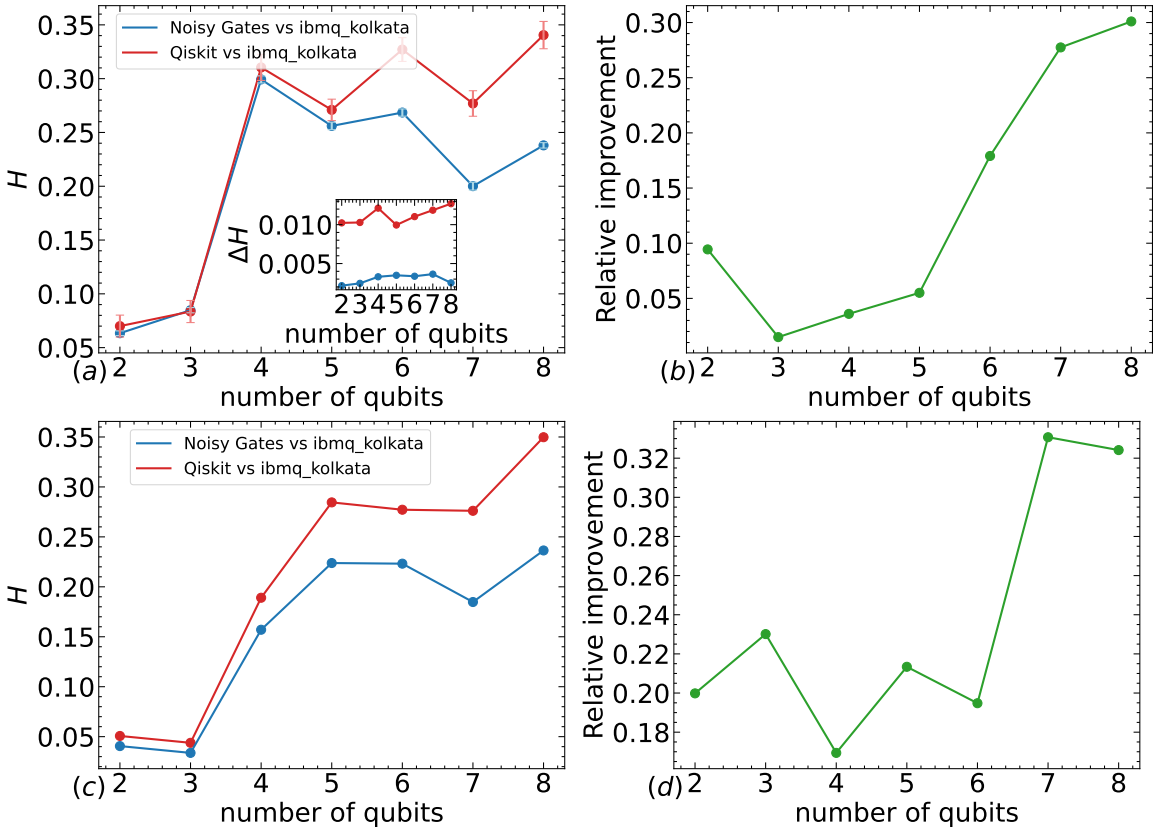

Figure 5.12: Quantum Fourier Transform. Panel (a) shows the Hellinger distances between the noisy gate approach and ibmq_kolkata, and between the Qiskit simulator and ibmq_kolkata, when executing the $\mathrm{QFT}^\dagger$ algorithm for $n = 2, \ldots, 8$ qubits. Each value is the mean of 100 independent simulations for the noisy gates, in blue, and for the Qiskit simulations, in red. The inset shows the standard deviations as functions of the number of qubits. Panel (b) shows the relative improvement, calculated as $|\bar{\mathcal{H}}_\chi^{\mathrm{ibm}} - \bar{\mathcal{H}}_\chi^{\mathrm{ng}}|/\bar{\mathcal{H}}_\chi^{\mathrm{ibm}}$. In panel (c) the comparison presented in (a) has been repeated a second time on ibmq_kolkata; in this case, only a single simulation of 1000 samples is considered. Panel (d) shows the relative improvement.

Many potential improvements can be straightforwardly implemented; most of them require an update of the noise model, not of the simulation strategy, i.e. Alg. 3, which is already very good. First of all, there are likely additional single-qubit errors which should be taken into account, for example coherent errors induced by the driving pulses. Secondly, the standard noise models considers only non-correlated single-qubit errors, but correlated two-qubits errors [46, 50] can be easily accommodated. Cross talk errors [47, 51] are included by adding small interactions between adjacent qubits.

The intentional omission of correlated errors was aimed at demonstrating the superiority of our approach in a simplified scenario, yet the analysis of the implications of correlated noise remains crucial to advance the potential application of the noisy gates approach in more realistic scenarios. From this perspective, it is noteworthy to underline the following. The thesis aligns its objective with demonstrating the utility of noisy quantum devices, coupled with scalable error mitigation techniques.

Highly non-local correlated errors prove to be significant and problematic for superconducting devices [46]. In this case, the parameters and locality of operators within the corresponding noise model would scale exponentially with the number of qubits in the devices, posing significant challenges for classical simulation and limiting the potential of the noisy gates approach and eventually of error mitigation.

Noise models with simplified correlations were introduced to address this issue, such as the "two-local Sparse Pauli Lindblad" [52]. This model considers up to two-local interactions between connected qubits. Utilizing mitigation techniques based on this model has demonstrated the utility of noisy quantum devices in experiments involving up to 100 qubits [53]. Other mitigation techniques based on the same noise model yield similar conclusions [54]. Although these results are preliminary and subject to debate they demonstrate how the most obvious complication of the standard noise model considered in the thesis, namely the addition of two-qubit interaction terms, is sufficient to effectively capture the behavior of noisy devices and to extract valuable output from the imperfect hardware.

Extending the noisy gates approach to the "two-local Sparse Pauli Lindblad" model is relatively straightforward. It implies to consider additional Lindblad operators of the form $\hat{\sigma}_i\hat{\sigma}_j$ where $\hat{\sigma}_\alpha$ are Pauli matrices acting on connected qubits. Depending on the specific connectivity of the device, this would increase the dimension and complicate the structure of the noisy gates. However it is reasonable to assume that correlated errors are mainly associated to two-qubit gates and the limited connectivity of the devices do not lead to exponential increase in the noisy gates dimensions allowing to derive their expression.

When trying to simulate with high accuracy the behaviour of a given device, the problem would then shift to the precise estimation of the noise parameters. In [52] the authors present a method to efficiently characterize the coupling rates of the

"two-local Sparse Pauli Lindblad" noise model.

Once the noise model is updated and the parameters are estimated accordingly, the expectation is to confirm the results of the analysis presented in the thesis based on the standard noise model. The noisy gates approach enhances the accuracy in describing the real device and consequently allows for more effective error mitigation.

The current version of the noisy gates approach relies on the Lindblad equation that works in the Markovian limit; this is reflected in the fact that we used stochastic equations based on white noises. The approach can be generalized to non-Markovian dynamics by using colored noises, as in [10, 16–18].

The approach is useful for other purposes that go beyond plane error analysis. As already pointed out, according to the noisy gates approach, the shape of the pulse in the driving Hamiltonians, (see Eq. (5.12) and Eq. (5.13)), affect the noise. In our work we chose for simplicity a rectangular shape, but in real devices different shapes can be used, for example Gaussian ones. A potential application of our approach is trying to suppress errors [55, 56] by optimizing the parameters of the pulse in order to minimize the effect of the noise [57–59]; the optimization can be performed for example by exploiting machine learning techniques, to find the best pulse parameters, which can then be tested on real quantum hardware. This will be the subject of future research.

Chapter 6

Noisy gates on integrated photonic devices

In this chapter we extend the formalism of noisy gates to second quantization for optical elements [60, 61], and apply it to photonic integrated devices in the dual-rail encoding. The general noisy gates derivation presented in Chapter 4 is valid for any noisy devices. However it is not trivial to extend it to the formalism of second quantization.

We successfully formulate the noisy versions of linear optical elements as phase shifters and beam splitters; we also consider the effects of imperfect single-photon sources, lossy optical guides and detectors as fictitious noisy optical elements that act on the modes at the proper step of the circuit. We apply the approach to study noise effects on the optimization loop of a variational quantum algorithm for a specific optimisation problem.

6.1 Noises in dual-rail encoding optical circuits

We focus on discrete variable quantum optics [62,63], in particular on the so called dual-rail encoding of linear optics quantum computing [64, 65], where the computational units are qubits. In this setup, optical circuits are made up of single photon sources, single-mode optical guides (also called spatial modes) in which photons propagate, linear optical elements that modify the photons state and single photon detectors. Thus, an optical circuit on N modes can be expressed as a unitary transformation with symmetry group $SU(N)$, followed by the detection. Since a qubit has a $SU(2)$ symmetry, then two spatial optical modes (dual-rail) with a single photon is a natural implementation of a qubit.

The logical states of the qubit are encoded in Fock states of the two modes $|0\rangle_L =$

$|10\rangle$, $|1\rangle_L = |01\rangle$ (with this notation we indicate that one of the two modes is occupied by the photon). Thus to represent a system of M qubits, $2M$ modes are needed with the addition of a certain number of ancillary modes used to implement the correct unitary transformation.

There are two main sources of noise affecting optical devices: photon losses and non-perfect indistinguishability of single photons [66, 67].

Photon losses are particularly daunting in the dual rail encoding, since after a loss the photon state exits from the logical computational states of the single qubit. Losses can occur at any step of the optical circuit, from the source to optical guides, optical elements and detectors. For each of these steps, one can associate a loss probability $\mathrm{p} = 1 - e^{-\Delta t/T}$, where Δt is a time interval and T is a characteristic loss time. The state of a photonic mode traveling through a lossy fiber can be expressed as [68–70]

$$\hat{\rho}(\Delta t) = \mathrm{p}\,|0\rangle\langle 0| + (1-\mathrm{p})\,|1\rangle\langle 1| \tag{6.1}$$

where now $|0\rangle$ is the state of the mode without photons and $|1\rangle$ is the state of the mode occupied by the photon. The actual value of p depends on the material used for the optical circuit as well as other experimental parameters. For the forthcoming simulations we vary p from 10^{-4} to 10^{-2}.

Photons non-perfect indistinguishability occurs when photons are generated. Single photons emitted by quantum dots [71] are indistinguishable if they have the same properties such as wavelength, polarization, temporal and spatial extent. A quantum dot sources indistinguishable photons if it emits by radiative decay only. In the presence of any other decoherence process for the quantum dot, the sourced photons are not perfectly indistinguishable. For this reason we simulate indistinguishability using decoherence models for solid state devices. Typical decoherence processes in solid state platforms are depolarization or dephasing [37, 72] (see also Sec. 5.1) and for this reason we connect photons non-perfect indistinguishability to depolarization/dephasing errors.

Photon losses and non-perfect indistinguishability lead to incoherent evolution. Coherent errors caused by imperfect calibration of optical elements are not considered here, as they can be accounted for using other existing techniques [73]. Further sources of errors, such as cross-talk effects, are beyond the scope of the thesis and can be added with further developments.

6.2 Noisy optical elements

We apply the noisy gates approach described in Chapter 4 to build the noisy version of linear optical elements. In particular we focus on phase shifters (PS) and

beam splitters (BS), showing how to write down their noisy version under the effect of photon loss errors.

We recap the noiseless expression of optical elements in order to set the main notation used in the following. A PS is an optical element that acts on a single mode by changing the phase of the photon state. The Hamiltonian of the PS is [60, 61]

$$\hat{\mathrm{H}}_{\mathrm{P}} = -\hbar\omega\hat{\mathrm{P}}, \qquad \hat{\mathrm{P}} = \hat{a}^\dagger\hat{a}, \tag{6.2}$$

where $\hat{a}$ and $\hat{a^\dagger}$ are respectively the annihilation and creation operators of a photon in the mode. The unitary evolution operator obtained by solving the Schrödinger equation is $\hat{\mathrm{U}}_{\mathrm{P}} = e^{i\theta\hat{\mathrm{P}}}$, where $\theta = \omega\cdot(t-t_0) = \omega\cdot\Delta t$. The annihilation and creation operators evolve accordingly as

$$\hat{\mathrm{U}}_{\mathrm{P}}\hat{a}^\dagger\hat{\mathrm{U}}_{\mathrm{P}}^\dagger = e^{i\theta}\hat{a}^\dagger, \qquad \hat{\mathrm{U}}_{\mathrm{P}}\hat{a}\hat{\mathrm{U}}_{\mathrm{P}}^\dagger = e^{-i\theta}\hat{a}. \tag{6.3}$$

A BS acts on two modes and can be defined through the Hamiltonian [60, 61]

$$\hat{\mathrm{H}}_{\mathrm{B}} = -\frac{\hbar\omega}{2}\hat{\mathrm{B}}(\phi), \quad \hat{\mathrm{B}}(\phi) = e^{-i\phi}\hat{a}_0\hat{a}_1^\dagger + e^{i\phi}\hat{a}_0^\dagger\hat{a}_1, \tag{6.4}$$

where we label the two modes with zero and one. The resulting unitary evolution operator is $\hat{\mathrm{U}}_{\mathrm{B}} = e^{i\frac{\theta}{2}\hat{\mathrm{B}}(\phi)}$, with $\theta = \omega\Delta t$ and, consequently, the annihilation/creation operators evolve as

$$\hat{\mathrm{U}}_{\mathrm{B}}\hat{a}_0^\dagger\hat{\mathrm{U}}_{\mathrm{B}}^\dagger = \cos(\theta/2)\hat{a}_0^\dagger + ie^{-i\phi}\sin(\theta/2)\hat{a}_1^\dagger, \tag{6.5}$$

$$\hat{\mathrm{U}}_{\mathrm{B}}\hat{a}_1^\dagger\hat{\mathrm{U}}_{\mathrm{B}}^\dagger = ie^{i\phi}\sin(\theta/2)\hat{a}_0^\dagger + \cos(\theta/2)\hat{a}_1^\dagger, \tag{6.6}$$

$$\hat{\mathrm{U}}_{\mathrm{B}}\hat{a}_0\hat{\mathrm{U}}_{\mathrm{B}}^\dagger = \cos(\theta/2)\hat{a}_0 - ie^{i\phi}\sin(\theta/2)\hat{a}_1, \tag{6.7}$$

$$\hat{\mathrm{U}}_{\mathrm{B}}\hat{a}_1\hat{\mathrm{U}}_{\mathrm{B}}^\dagger = -ie^{-i\phi}\sin(\theta/2)\hat{a}_0 + \cos(\theta/2)\hat{a}_1. \tag{6.8}$$

These transformations define a unitary matrix that act on the vectors of creation operators $(\hat{a}_0^\dagger, \hat{a}_1^\dagger)^T$ or annihilation operators $(\hat{a}_0, \hat{a}_1)^T$. The matrix evolving creation operators reads

$$\hat{\mathcal{U}}_{\mathrm{B}} = \begin{pmatrix} \cos(\theta/2) & ie^{-i\phi}\sin(\theta/2) \\ ie^{i\phi}\sin(\theta/2) & \cos(\theta/2) \end{pmatrix}, \tag{6.9}$$

while that for annihilation operators is $\hat{\mathcal{U}}_{\mathrm{B}}^\dagger$. This is the differentiating feature of linear optics: an optical circuit acting on M modes is expressed as a $M\times M$ unitary matrix $\hat{\mathcal{U}}$ that evolve creation operators on the modes rather than Fock states. The amplitudes (or probabilities) of all the possible output Fock states are computed through a suitable expression involving permanents of matrices build up from rows and columns of $\hat{\mathcal{U}}$ [74]. This makes the adaptation of the noisy gates approach not straightforward. In the next section we start by showing an example of the cause of the issues and then we successfully derive the expressions of noisy phase shifters and beam splitters.

6.2.1 Noisy phase shifter

The obvious way to model photon losses on a given mode 0 is to consider the system in contact with an environment that absorbs photons. By following the protocol described in Sec. 4.1.2 we have to specify the operators in Eq. (4.1): the Hamiltonian operator is the PS Hamiltonian in Eq. (6.2) on mode 0, i.e. $\hat{\mathrm{P}}_0 = \hat{a}_0^\dagger \hat{a}_0$, and the Lindblad operator is $\hat{\mathrm{L}} = \hat{a}_0$, modeling the absorption of photons from the mode. The corresponding expression for the noisy gate reads

$$\hat{\mathrm{N}}_0 = \hat{\mathrm{U}}_0 e^{-\frac{\epsilon_0^2}{2}\hat{\mathrm{D}}_0} e^{i\epsilon_0 \hat{\mathrm{S}}_0}, \tag{6.10}$$

where $\hat{\mathrm{U}}_0 = e^{i\theta\hat{\mathrm{P}}_0}$, $\hat{\mathrm{D}}_0 = \int_{t_0}^t \mathrm{ds}(\hat{a}_0^\dagger(s)\hat{a}_0(s) - \hat{a}_0^2(s))$ and $\hat{\mathrm{S}}_0 = \int_{t_0}^t \mathrm{dW(s)}\hat{a}_0(s)$. The second step of the noisy gates protocol requires to compute the time dependent Lindblad operator, that reads

$$\hat{a}_0^\dagger(s) = \hat{\mathrm{U}}_0^\dagger(s,t_0)\hat{a}_0^\dagger\hat{\mathrm{U}}_0(s,t_0) = e^{-i\theta(s,t_0)}\hat{a}_0^\dagger \tag{6.11}$$

where the last equality holds because of Eq. (6.3). Thus we can write

$$\hat{\mathrm{D}}_0 = \Delta t \hat{a}_0^\dagger \hat{a}_0 + (\mathrm{D}_C - i\mathrm{D}_S)\hat{a}_0^2\,, \quad \hat{\mathrm{S}}_0 = (\mathrm{I}_C - i\mathrm{I}_S)\hat{a}_0 \tag{6.12}$$

where

$$\mathrm{D}_C = \int_{t_0}^t \mathrm{ds}\cos 2\theta(s,t_0) \qquad \mathrm{D}_S = \int_{t_0}^t \mathrm{ds}\sin 2\theta(s,t_0) \tag{6.13}$$

$$\mathrm{I}_C = \int_{t_0}^t \mathrm{dW(s)}\cos\theta(s,t_0) \qquad \mathrm{I}_S = \int_{t_0}^t \mathrm{dW(s)}\sin\theta(s,t_0)\,. \tag{6.14}$$

The latter are Gaussian stochastic processes with means $\mathbb{E}\big[\mathrm{I}_C\big] = \mathbb{E}\big[\mathrm{I}_S\big] = 0$, variances and covariances

$$\mathbb{V}\big[\mathrm{I}_C\big] = \int_{t_0}^t \mathrm{d}s\cos^2\theta(s,t_0) \qquad \mathbb{V}\big[\mathrm{I}_S\big] = \int_{t_0}^t \mathrm{d}s\sin^2\theta(s,t_0) \tag{6.15}$$

$$\mathbb{E}\big[\mathrm{I}_C\mathrm{I}_S\big] = \int_{t_0}^t \mathrm{d}s\cos\theta(s,t_0)\sin\theta(s,t_0)\,. \tag{6.16}$$

When trying to calculate $\hat{\mathrm{N}}_0\hat{a}_0^\dagger\hat{\mathrm{N}}_0^\dagger$ it is not possible to write down the evolution of the creation operator via the action of a linear matrix acting on it.

In order to avoid such problem we consider a larger physical system consisting of two photon modes: mode 0 is the physical mode where the PS acts, while mode 1 is a virtual mode that acts as a reservoir for photon losses. The idea is to model the interaction with the environment as a fictitious BS between the two modes, tracing

out the virtual mode. In this way, the effective action on the system is that the photon is absorbed with some probability. Thus, we choose $\hat{\mathrm{B}}_{01} = \hat{a}_0\hat{a}_1^\dagger + \hat{a}_0^\dagger\hat{a}_1$ as Lindblad operator; the latter can be obtained from the expression for $\hat{\mathrm{B}}(\phi)$ in Eq. (6.4) by setting $\phi = 0$. This Lindblad operator acts as a virtual BS that can shift photons from mode 0 to the virtual mode 1 (and viceversa).

Following Sec. 4.1, the resulting expression for the noisy PS is

$$\hat{\mathrm{N}}_{01} = \hat{\mathrm{U}}_0 e^{i\epsilon_0 \hat{\mathrm{S}}_{01}}, \tag{6.17}$$

where $\hat{\mathrm{U}}_0 = e^{i\theta\hat{\mathrm{P}}_0}$ and $\hat{\mathrm{S}}_{01} = \int_{t_0}^{t} \mathrm{dW(s)}\hat{\mathrm{B}}_{01}(s)$ and the deterministic term is not present since the Lindblad operator is Hermitian.

To compute the form of the stochastic operator $\hat{\mathrm{S}}_{01}$, we notice that

$$\begin{aligned}
&\hat{\mathrm{B}}_{01}(s) = \hat{\mathrm{U}}_0^\dagger(s,t_0)\hat{\mathrm{B}}_{01}\hat{\mathrm{U}}_0(s,t_0) \\
&= e^{-i\theta(s,t_0)\hat{\mathrm{P}}_0}\hat{a}_0 e^{i\theta(s,t_0)\hat{\mathrm{P}}_0}\hat{a}_1^\dagger + e^{-i\theta(s,t_0)\hat{\mathrm{P}}_0}\hat{a}_0^\dagger e^{i\theta(s,t_0)\hat{\mathrm{P}}_0}\hat{a}_1 \\
&= e^{i\theta(s,t_0)}\hat{a}_0\hat{a}_1^\dagger + e^{-i\theta(s,t_0)}\hat{a}_0^\dagger\hat{a}_1 \\
&= \cos\theta(s,t_0)(\hat{a}_0\hat{a}_1^\dagger + \hat{a}_0^\dagger\hat{a}_1) + i\sin\theta(s,t_0)(\hat{a}_0\hat{a}_1^\dagger - \hat{a}_0^\dagger\hat{a}_1) \\
&= \cos\theta(s,t_0)\hat{\mathrm{B}}_{01} - \sin\theta(s,t_0)\hat{\mathrm{C}}_{01}
\end{aligned} \tag{6.18}$$

where in the third line we used Eq.(6.3) with the adjoint unitary evolution and we defined $\hat{\mathrm{C}}_{01} = i(\hat{a}_0^\dagger\hat{a}_1 - \hat{a}_0\hat{a}_1^\dagger)$, which can be obtained from $\hat{\mathrm{B}}(\phi)$ in Eq.(6.4) by choosing $\phi = \pi/2$.

Then the stochastic operator reads

$$\hat{\mathrm{S}}_{01} = \mathrm{I}_C\hat{\mathrm{B}}_{01} - \mathrm{I}_S\hat{\mathrm{C}}_{01}, \tag{6.19}$$

where $\mathrm{I}_C = \int_{t_0}^{t} \mathrm{dW(s)}\cos\theta(s,t_0)$ and $\mathrm{I}_S = \int_{t_0}^{t} \mathrm{dW(s)}\sin\theta(s,t_0)$ are the same stochastic integrals in Eq. (6.14) and their variances and covariances are those in Eq. (6.15).

Finally, since to second order in ϵ one has that $e^{\epsilon(\hat{\mathrm{A}}+\hat{\mathrm{B}})} = e^{\epsilon\hat{\mathrm{A}}}e^{\epsilon\hat{\mathrm{B}}}$, Eq. (6.17) implies that

$$\hat{\mathrm{N}}_{01} = \hat{\mathrm{U}}_0 e^{i\epsilon_0\mathrm{I}_C\hat{\mathrm{B}}_{01}} e^{-i\epsilon_0\mathrm{I}_S\hat{\mathrm{C}}_{01}}. \tag{6.20}$$

Eq. (6.20) defines the evolution of creation and annihilation operators under the action of a noisy PS, eventually dictating the matrix that act on vectors of creation operators. In the case of the noisy PS we have

$$\hat{\mathcal{N}}_{01} = \begin{pmatrix} e^{i\theta} & 0 \\ 0 & 1 \end{pmatrix} \cdot \begin{pmatrix} \cos(\epsilon_0\mathrm{I_C}) & i\sin(\epsilon_0\mathrm{I_C}) \\ i\sin(\epsilon_0\mathrm{I_C}) & \cos(\epsilon_0\mathrm{I_C}) \end{pmatrix} \cdot \begin{pmatrix} \cos(\epsilon_0\mathrm{I_S}) & -\sin(\epsilon_0\mathrm{I_S}) \\ \sin(\epsilon_0\mathrm{I_S}) & \cos(\epsilon_0\mathrm{I_S}) \end{pmatrix}, \tag{6.21}$$

whereas $\hat{\mathcal{N}}_{01}^\dagger$ acts on annihilation operators. In Eq. (6.21) the parameter ϵ_0 is connected to photon loss probability p_0 on mode 0 as $\epsilon_0 = \sqrt{-\log(1-2\mathrm{p}_0)/2}$ where

$\mathrm{p}_0 = (1 - e^{-2\Delta t/T})/2$ and $\epsilon_0^2 = \Delta t/T$, with T the characteristic time of photon losses. We choose such time dependence for p_0 because by taking the average over the processes I_C and I_S one has $\mathbb{E}[\sin^2(\epsilon \mathrm{I}_k)] = (1 - e^{-2\epsilon_0^2})/2 = \mathrm{p}_0$ with $k = C, S$. Moreover, we are not interested in the regime in which there is more than 50% of loss probability.

By tracing out the virtual mode, we get the final expression for the noisy PS on mode 0

$$\hat{\mathcal{N}}_0 = e^{i\theta} \cos(\epsilon_0 \mathrm{I_C}) \cos(\epsilon_0 \mathrm{I_S}) \tag{6.22}$$

while Eq. (6.21) is unitary on the total system of physical plus virtual modes, the final expression for the noisy PS acting on the physical mode only is not unitary anymore.

6.2.2 Noisy beam splitter

The derivation of the noisy BS exploits the same idea of coupling the physical modes with a virtual mode. In particular, we label modes 0 and 1 as physical modes and mode 2 as the virtual mode. The Hamiltonian operator is that in Eq. (6.2) with $\phi = 0$, i.e. $\hat{\mathrm{B}}_{01} = \hat{a}_0 \hat{a}_1^\dagger + \hat{a}_0^\dagger \hat{a}_1$. This choice is in accordance with the standard Reck decomposition of optical circuits, also employed in [75]. As Lindblad operators we choose $\hat{\mathrm{B}}_{02} = \hat{a}_0 \hat{a}_2^\dagger + \hat{a}_0^\dagger \hat{a}_2$ and $\hat{\mathrm{B}}_{12} = \hat{a}_1 \hat{a}_2^\dagger + \hat{a}_1^\dagger \hat{a}_2$ modeling photon shifts from mode 0 to 2 and from mode 1 to 2 respectively. The corresponding noisy BS reads

$$\hat{\mathrm{N}}_{012} = \hat{\mathrm{U}}_{01} e^{i\epsilon_0 \hat{\mathrm{S}}_{02} + i\epsilon_1 \hat{\mathrm{S}}_{12}}, \tag{6.23}$$

where $\hat{\mathrm{U}}_{01} = e^{i\frac{\theta}{2}\hat{\mathrm{B}}_{01}}$ and $\hat{\mathrm{S}}_{j2} = \int_{t_0}^t \mathrm{dW_j(s)} \hat{\mathrm{B}}_{j2}(s)$ with $j = 0, 1$. In Eq. (6.23) the parameters ϵ_j are defined as $\epsilon_j = \sqrt{-\log(1 - 2\mathrm{p}_j)/2}$ as for the noisy PS. By performing a similar calculation to Eq. (6.18) where now one uses the BS relations in Eqs. (6.5), (6.6), (6.7) and (6.8) with the adjoint unitary evolution, the expressions for $\hat{\mathrm{B}}_{j2}(s)$ are

$$\hat{\mathrm{B}}_{02}(s) = \cos\left(\frac{\theta(s,t_0)}{2}\right)\hat{\mathrm{B}}_{02} - \sin\left(\frac{\theta(s,t_0)}{2}\right)\hat{\mathrm{C}}_{12}, \tag{6.24}$$

$$\hat{\mathrm{B}}_{12}(s) = \cos\left(\frac{\theta(s,t_0)}{2}\right)\hat{\mathrm{B}}_{12} - \sin\left(\frac{\theta(s,t_0)}{2}\right)\hat{\mathrm{C}}_{02}, \tag{6.25}$$

where $\hat{\mathrm{C}}_{j2} = i(\hat{a}_j^\dagger \hat{a}_2 - \hat{a}_j \hat{a}_2^\dagger)$. The stochastic operators are

$$\hat{\mathrm{S}}_{02} = \mathrm{I}_{C0}\hat{\mathrm{B}}_{02} - \mathrm{I}_{S0}\hat{\mathrm{C}}_{12}, \tag{6.26}$$

$$\hat{\mathrm{S}}_{12} = \mathrm{I}_{C1}\hat{\mathrm{B}}_{12} - \mathrm{I}_{S1}\hat{\mathrm{C}}_{02}, \tag{6.27}$$

where $\mathrm{I}_{Cj} = \int_{t_0}^t \mathrm{dW_j(s)} \cos\theta(s,t_0)$ and $\mathrm{I}_{Sj} = \int_{t_0}^t \mathrm{dW_j(s)} \sin\theta(s,t_0)$. The latter Gaussian processes have the same variances and covariances in Eq. (6.15). Finally we can

express Eq. (6.23) as

$$\hat{\mathrm{N}}_{012} = \hat{\mathrm{U}}_{01} e^{i\epsilon_0 \mathrm{I}_{C0} \hat{\mathrm{B}}_{02}} e^{-i\epsilon_0 \mathrm{I}_{S0} \hat{\mathrm{C}}_{12}} e^{i\epsilon_1 \mathrm{I}_{C1} \hat{\mathrm{B}}_{12}} e^{-i\epsilon_1 \mathrm{I}_{S1} \hat{\mathrm{C}}_{02}} , \tag{6.28}$$

and the corresponding action on creation operators is given by

$$\begin{aligned} \hat{\mathcal{N}}_{012} = & \begin{pmatrix} \cos\theta/2 & i\sin\theta/2 & 0 \\ i\sin\theta/2 & \cos\theta/2 & 0 \\ 0 & 0 & 1 \end{pmatrix} \cdot \begin{pmatrix} \cos(\epsilon_0 \mathrm{I}_{\mathrm{C0}}) & 0 & i\sin(\epsilon_0 \mathrm{I}_{\mathrm{C0}}) \\ 0 & 1 & 0 \\ i\sin(\epsilon_0 \mathrm{I}_{\mathrm{C0}}) & 0 & \cos(\epsilon_0 \mathrm{I}_{\mathrm{C0}}) \end{pmatrix} \cdot \\ & \begin{pmatrix} 1 & 0 & 0 \\ 0 & \cos(\epsilon_0 \mathrm{I}_{\mathrm{S0}}) & -\sin(\epsilon_0 \mathrm{I}_{\mathrm{S0}}) \\ 0 & \sin(\epsilon_0 \mathrm{I}_{\mathrm{S0}}) & \cos(\epsilon_0 \mathrm{I}_{\mathrm{S0}}) \end{pmatrix} \cdot \begin{pmatrix} 1 & 0 & 0 \\ 0 & \cos(\epsilon_1 \mathrm{I}_{\mathrm{C1}}) & i\sin(\epsilon_1 \mathrm{I}_{\mathrm{C1}}) \\ 0 & i\sin(\epsilon_1 \mathrm{I}_{\mathrm{C1}}) & \cos(\epsilon_1 \mathrm{I}_{\mathrm{C1}}) \end{pmatrix} \cdot \\ & \begin{pmatrix} \cos(\epsilon_1 \mathrm{I}_{\mathrm{S1}}) & 0 & -\sin(\epsilon_1 \mathrm{I}_{\mathrm{S1}}) \\ 0 & 1 & 0 \\ \sin(\epsilon_1 \mathrm{I}_{\mathrm{S1}}) & 0 & \cos(\epsilon_1 \mathrm{I}_{\mathrm{S1}}) \end{pmatrix} . \end{aligned} \tag{6.29}$$

By tracing out the virtual mode, the final non unitary expression for the noisy BS reads

$$\begin{aligned} \hat{\mathcal{N}}_{01} = & \begin{pmatrix} \cos\theta/2 & i\sin\theta/2 \\ i\sin\theta/2 & \cos\theta/2 \end{pmatrix} \cdot \begin{pmatrix} \cos(\epsilon_0 \mathrm{I}_{\mathrm{C0}}) & 0 \\ 0 & 1 \end{pmatrix} \cdot \\ & \begin{pmatrix} 1 & 0 \\ 0 & \cos(\epsilon_0 \mathrm{I}_{\mathrm{S0}}) \end{pmatrix} \cdot \begin{pmatrix} 1 & 0 \\ 0 & \cos(\epsilon_1 \mathrm{I}_{\mathrm{C1}}) \end{pmatrix} \cdot \begin{pmatrix} \cos(\epsilon_1 \mathrm{I}_{\mathrm{S1}}) & 0 \\ 0 & 1 \end{pmatrix} . \end{aligned} \tag{6.30}$$

6.2.3 Other noises

As explained in section 6.1, photon generation, propagation of photons inside optical guides and detection are also affected by errors. We now describe how to account for such errors with the noisy gates approach.

A quantum dot undergoing decoherence processes generates non perfect indistinguishable photons. In the case of dual rail encoding, the only relevant property is the photon path, i.e. through which of the optical guides, or modes, a photon is traveling. In this setup, the only way to distinguish two photons, if we consider only incoherent errors, is to mix the associated qubit state. This can be modelled by considering depolarization errors arising at the sources and inherited by the photons.

To model imperfect single-photon sources we insert at the beginning of the optical circuit a layer of fictitious optical elements to each couple of modes that simulate single-qubit depolarizing errors. Such optical elements are built within the noisy gates framework. The choice of focusing on single-qubit depolarizing channel can be generalized to account for depolarization on multiple qubits.

Single-qubit depolarization has Lindblad operators $\hat{\mathrm{X}}$,$\hat{\mathrm{Y}}$ and $\hat{\mathrm{Z}}$. We can map such operators to operators defined in terms of creation and annihilation operators on the

physical modes, thus acting on photons of the circuit. For example when solving the Schrödinger equation with the BS Hamiltonian in Eq. (6.4) with $\phi = 0$ and $\theta = \pi$, the corresponding unitary on the creation operators acts as an $\hat{\mathrm{X}}$ gate on a qubit in the dual rail encoding (see Eq.(6.9)). Similarly a $\hat{\mathrm{Y}}$ operator is obtained with the BS Hamiltionan with $\phi = \pi/2$ and $\theta = \pi$. The operator $\hat{\mathrm{Z}}$ is obtained by solving the Schrödinger equation with the PS Hamiltonian in Eq. (6.2) with $\theta = \pi$ applied to mode 1. For these reasons, to describe depolarizing errors, we can use Eq. (4.1) without Hamiltonian operator and with Lindblad operators $\hat{\mathrm{B}}_{01}$, $\hat{\mathrm{C}}_{01}$ and $\hat{\mathrm{P}}_1$. The resulting noisy gate is

$$\hat{\mathrm{N}}_{01}^{(\mathrm{dep})} = e^{i\epsilon_d \hat{\mathrm{S}}_{01}^{(x)}} e^{i\epsilon_d \hat{\mathrm{S}}_{01}^{(y)}} e^{i\epsilon_d \hat{\mathrm{S}}_{01}^{(z)}}, \tag{6.31}$$

where $\hat{\mathrm{S}}_{01}^{(x)} = \hat{\mathrm{B}}_{01}\mathrm{W}_x(t,t_0)$, $\hat{\mathrm{S}}_{01}^{(y)} = \hat{\mathrm{C}}_{01}\mathrm{W}_y(t,t_0)$ and $\hat{\mathrm{S}}_{01}^{(z)} = \hat{\mathrm{P}}_1\mathrm{W}_z(t,t_0)$. The corresponding unitary acting on the creation operators becomes

$$\hat{\mathcal{N}}_{01}^{(\mathrm{dep})} = \begin{pmatrix} \cos(\epsilon_d \mathrm{W}_x) & i\sin(\epsilon_d \mathrm{W}_x) \\ i\sin(\epsilon_d \mathrm{W}_x) & \cos(\epsilon_d \mathrm{W}_x) \end{pmatrix} \cdot \begin{pmatrix} \cos(\epsilon_d \mathrm{W}_y) & -\sin(\epsilon_d \mathrm{W}_y) \\ \sin(\epsilon_d \mathrm{W}_y) & \cos(\epsilon_d \mathrm{W}_y) \end{pmatrix} \cdot \begin{pmatrix} 1 & 0 \\ 0 & e^{i\epsilon_d \mathrm{W}_z} \end{pmatrix}. \tag{6.32}$$

Here the parameter ϵ_d has the same definition of the loss parameter but now it is related to depolarizing probability p_d. Moreover we stress that, despite the similarity with the expression of noisy optical elements, the effects of Eqs. (6.31), (6.32) are different because modes 0 and 1 are both physical modes.

In Sec. 6.2 we have dealt with optical elements affected by photon losses, however photons are lost also while traveling through optical guides or when being measured by detectors. To model such losses, similarly to noisy optical elements, we consider two photon modes 0, 1, respectively the physical and virtual modes, with Lindblad operator $\hat{\mathrm{B}}_{01}$ but this time we use Eq. (4.1) without Hamiltonian operator. A straightforward calculation leads to

$$\hat{\mathrm{N}}_{01}^{(\mathrm{loss})} = e^{i\epsilon \hat{\mathrm{S}}_{01}}, \tag{6.33}$$

where $\hat{\mathrm{S}}_{01} = \hat{\mathrm{B}}_{01}\mathrm{W}(t,t_0)$ and $\epsilon = \sqrt{-\log(1-2\mathrm{p})/2}$ with p the loss probability inside the optical guide or in the detector. Consequentially we have

$$\hat{\mathcal{N}}_{01}^{(\mathrm{loss})} = \begin{pmatrix} \cos(\epsilon \mathrm{W}) & i\sin(\epsilon \mathrm{W}) \\ i\sin(\epsilon \mathrm{W}) & \cos(\epsilon \mathrm{W}) \end{pmatrix}. \tag{6.34}$$

and by tracing out the virtual mode one gets

$$\hat{\mathcal{N}}_{0}^{(\mathrm{loss})} = \cos(\epsilon \mathrm{W}). \tag{6.35}$$

6.3 Comparison with other approaches

In this section we list other methods to simulate noises in optical devices. The latter generally differ from the standard simulations methods for the evolution of

qubit states presented in Chapter 3.

There are two main approaches for simulating photon losses: the fixed-loss model [76–78] and the beam splitter loss model [27, 78–80]. The former assumes that the number of lost particles is a controlled quantity; indeed it is based on the assumption that initially there are n photons and exactly $n-l$ of them are lost. Based on this assumption, losses are simulated by tracing out $n-l$ of the n photons $\hat{\rho}' = \mathrm{Tr}_{n-l}(\hat{\rho})$ and by using the fact that $\mathrm{Tr}_{n-l}(\hat{\mathrm{U}}^{\otimes n}\hat{\rho}\hat{\mathrm{U}}^{\dagger\otimes n}) = \hat{\mathrm{U}}^{\otimes n}\,\mathrm{Tr}_{n-l}(\hat{\rho})\hat{\mathrm{U}}^{\dagger\otimes n}$. Thus, it is not important whether losses occurred before or after the implemented ideal linear transformation. This approach is limited since experimentally the number of lost photons is random.

The beam splitter loss model, which inspired the derivation of noisy optical elements in the noisy gates approach in Sec. 6.2, is based on the idea of adding a virtual mode to the physical modes and to model losses as a BS (see Eq. (6.9) with $\phi = 0$) with reflectance equal to the loss probability: $\mathrm{R} = \mathrm{p}$. Since the relation between reflectance and the angle θ of a BS is $\cos(\theta/2) = \sqrt{1-\mathrm{R}}$ and $\sin(\theta/2) = \sqrt{\mathrm{R}}$, then one gets

$$\begin{pmatrix} \sqrt{1-\mathrm{p}} & i\sqrt{\mathrm{p}} \\ i\sqrt{\mathrm{p}} & \sqrt{1-\mathrm{p}} \end{pmatrix}, \tag{6.36}$$

where the probability of losing a photon is exactly $|{}_{\text{out}}\langle 01|10\rangle_{\text{in}}|^2 = \mathrm{p}$. Eq. (6.36) is equivalent to the expression for the lossy optical guides and detection derived in Sec. 6.2.3: in fact Eq. (6.34) is the stochastic version of Eq. (6.36). Indeed, for the noisy gates approach the probability of losing a photon is $|{}_{\text{out}}\langle 01|10\rangle_{\text{in}}|^2 = \sin^2(\epsilon \mathrm{W})$ and by taking the average over the Wiener process one has $\mathbb{E}[\sin^2(\epsilon \mathrm{W})] = (1 - e^{-2\epsilon^2})/2 = \mathrm{p}$.

The equivalence applies only to lossy optical guides and detectors. The stochastic processes appearing in the expressions for noisy optical elements in Eqs. (6.21) and (6.29) are not independent from the parameters, such as the angle of rotation, of the corresponding optical elements. Therefore our approach is not reducible to the standard beam splitter loss model. The latter is actually more closer to the second quantization version of the standard noise gate approach described in Sec. 3.1, where the unitary evolution and the noise one are decoupled. In our approach, by including the noise into the gates, each noisy optical elements has its own behaviour due to losses (even if the loss parameter p is the same for all elements). Experimentally, the dependence of photon losses on the parameters of optical elements is small and the general assumption is that photon loss is independent from the angles of BS and PS [66], motivating the usage of the standard beam splitter loss model. However, we already proved in Chapter 5 (see also [41]), that, for IBM devices, relaxing this assumption, namely that of separating the noise and unitary evolution, provides a more accurate simulation method.

Different approaches exist in the literature for the treatment of imperfect photon

sources. In [81], the authors considered a parametrized quantum dot able to simulate the creation of pairs of entangled photon in a mixed state. Another example is the modeling used in [75] where an imperfect quantum-dot single-photon source is modeled by a statistical mixture of Fock states. In this work we deal with single-photon sources thus, following the latter approach, we implemented the stochastic unraveling of a single-qubit depolarizing Lindblad equation as shown in Eq. (6.32), that equivalently outputs a mixed Fock state of the encoded qubits. This can be generalized to multiple qubit depolarizing channels, taking into account multi photon distinguishability [67].

6.4 Variational quantum algorithm simulations

In this section we test the performances of the noisy gates method adapted to integrated photonic circuits. We build a noisy variational quantum algorithm (VQA) [82, 83] to solve the MAX 2-CUT problem [84–86] and we study its performances in different noise scenarios.

The computational backend used for the simulations is the SLOS backend [74] provided by Perceval [75]. In particular we input to SLOS the final matrix of the full optical circuit calculated by suitably composing the expression of all different optical elements. Then, SLOS handles the calculations of permanents to get the output probability amplitudes of the Fock states [74]. To simulate the effect of imperfect

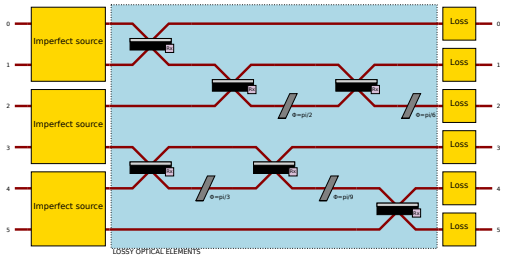

Figure 6.1: Schematic depiction of the simulation of a generic noisy optical circuit. On the left in yellow, a layer of fictitious optical elements models depolarization for each couple of modes. In the blue area, each optical element of the original circuit is replaced with the corresponding noisy one and for lost photons during detection we add a layer of lossy channel for each mode, shown here in yellow on the right.

photon sources, we add to the optical circuit a layer of fictitious optical elements modeling depolarization, see Eq. (6.32), for each couple of modes. To simulate photon losses, each optical element of the original circuit is replaced with the corresponding

noisy one, see Eqs. (6.22) and (6.30), and for losses at detection we add a layer of lossy channel to each mode as in Eq. (6.35). The corresponding noisy optical circuit is schematically depicted in Fig. 6.1.

We focus on the VQA algorithm applied to the MAX 2-CUT problem. The MAX 2-CUT problem is a well known optimization problem that requires to find a cut dividing the vertices of a graph in two complementary subsets, such that the number of edges crossed by the cut is maximized. Given a graph $G = (V, E)$, with $V = \{1, \dots, N\}$ and $E = \{\langle i, j\rangle\}$ the sets of vertices i and edges $\langle i, j\rangle$, the goal is to maximize the following cost function

$$\hat{\mathrm{H}}_C = \sum_{\langle i,j\rangle} \frac{1}{2}(1 - \hat{\mathrm{Z}}_i \hat{\mathrm{Z}}_j). \tag{6.37}$$

We focus on a square graph with four nodes

$$V = \{1, 2, 3, 4\} \qquad E = \{\langle 1, 2\rangle \langle 2, 3\rangle \langle 3, 4\rangle \langle 4, 1\rangle\}. \tag{6.38}$$

Finding the optimal cut is equivalent to minimizing the following cost Hamiltonian

$$\hat{\mathrm{H}}_C = \sum_{\langle i,j\rangle} \hat{\mathrm{Z}}_i \hat{\mathrm{Z}}_j; \tag{6.39}$$

for which the optimal, or exact, energy is $E_0 = -4$, corresponding to cuts giving $V_1 = \{1, 3\}$ and $V_2 = \{2, 4\}$ as complementary subsets of V. This is the target energy of the optimization of the VQA.

We use a specific ansatz $\hat{\mathrm{U}}_{ansatz}(\theta)$ for the optimization loop of VQA, which is shown in Fig. 6.2. The output of each simulation is a density matrix $\hat{\rho}$. The cost function for the optimization is the energy calculated as $E = \mathrm{Tr}\Big(\hat{\rho}(\theta)\hat{\mathrm{H}}_C\Big)$, where $\hat{\rho}(\theta) = |\psi(\theta)\rangle \langle\psi(\theta)|$ and $|\psi(\theta)\rangle = \hat{\mathrm{U}}_{ansatz}(\theta)\,|0\rangle^{\otimes 4}$. We choose a number of samples $\mathrm{N}_{samples} = 500$ and random initial parameters. The classical optimizer method used to update the parameters is the gradient-free method COBYLA [87].

We study the convergence of the optimization in the noiseless case, in the presence of depolarization with $\mathrm{p} = 10^{-4}, 10^{-3}, 10^{-2}$, in the presence of losses with $\mathrm{p} = 10^{-4}, 10^{-3}, 10^{-2}$ and under the combined action of depolarization and losses for $\mathrm{p} = 10^{-4}, 10^{-3}, 10^{-2}$. We restrict the analysis to such orders of magnitude of the error probability, because for $\mathrm{p} < 10^{-4}$ the effects of noises on the optimization are negligible and for $\mathrm{p} > 10^{-2}$ results might not be reliable since our approach is based on a perturbative expansion, as explained in Sec. 4.1.

The results of simulations are displayed in Fig. 6.3. The noiseless optimization, shown in blue, converges to the optimal value with high precision, validating the ansatz. Panels (a) and (b) show the simulations with the effects of depolarization

only: as expected, the higher the error probability, the higher the deviation from the exact energy. Notably, when $p = 10^{-4}$, the estimate of E has a $\sim 1\%$ relative error. In panels (c) and (d) we show the effets of photon losses. The ansatz seem to be more resilient to this type of noise: for p $= 10^{-4}$ and p $= 10^{-3}$ the relative error is below 0.1% and for p $= 10^{-2}$ the relative error is below 1%. The combination of photon losses and depolarization, shown in panels (e) and (f), has the effect of further decreasing the accuracy of the optimization as all relative errors are above 1%.

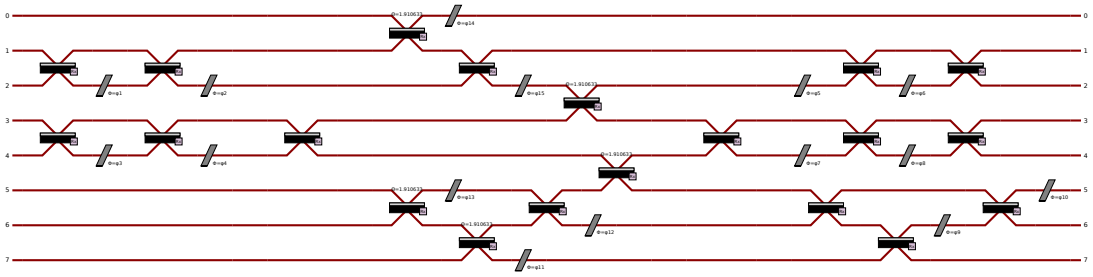

Figure 6.2: Optical circuit ansatz for the VQA solving the MAX 2-CUT on a square graph.

Table 6.1 reports the approximation ratios, defined as $R = E_f/E_0$ where E_f is the final energy of the optimization, for different type of noises and for different orders of magnitude of the error probabilities. The best approximation ratios are obtained with the simulations considering photon losses only.

The choice of an appropriate ansatz is a critical factor in determining the VQA performance [82]. The motivation behind opting for a carefully balanced ansatz lies in avoiding excessive expressivity, which can potentially lead to challenges during the classical optimization process. An ansatz with overly complex representations may be able to effectively capture the features of the problem's Hamiltonian. However, this increased expressivity could introduce a large number of parameters and intricate interactions. As a consequence, the gradients of cost function may vanish exponentially during classical optimization [88]. This phenomenon hinders the optimization process, making it difficult to converge efficiently and find satisfactory solutions. In the circuit model of quantum computing, several ansatz designs have been developed to construct parameterized quantum circuits tailored to different tasks and applications [82]. We finally mention that in [89] we have performed further simulations of optical circuits realizing the X gate in both the gate based (GBQC) and measurement based quantum computing (MBQC) framework, as well as the optical circuit preparing the Bell state in the presence of noises.

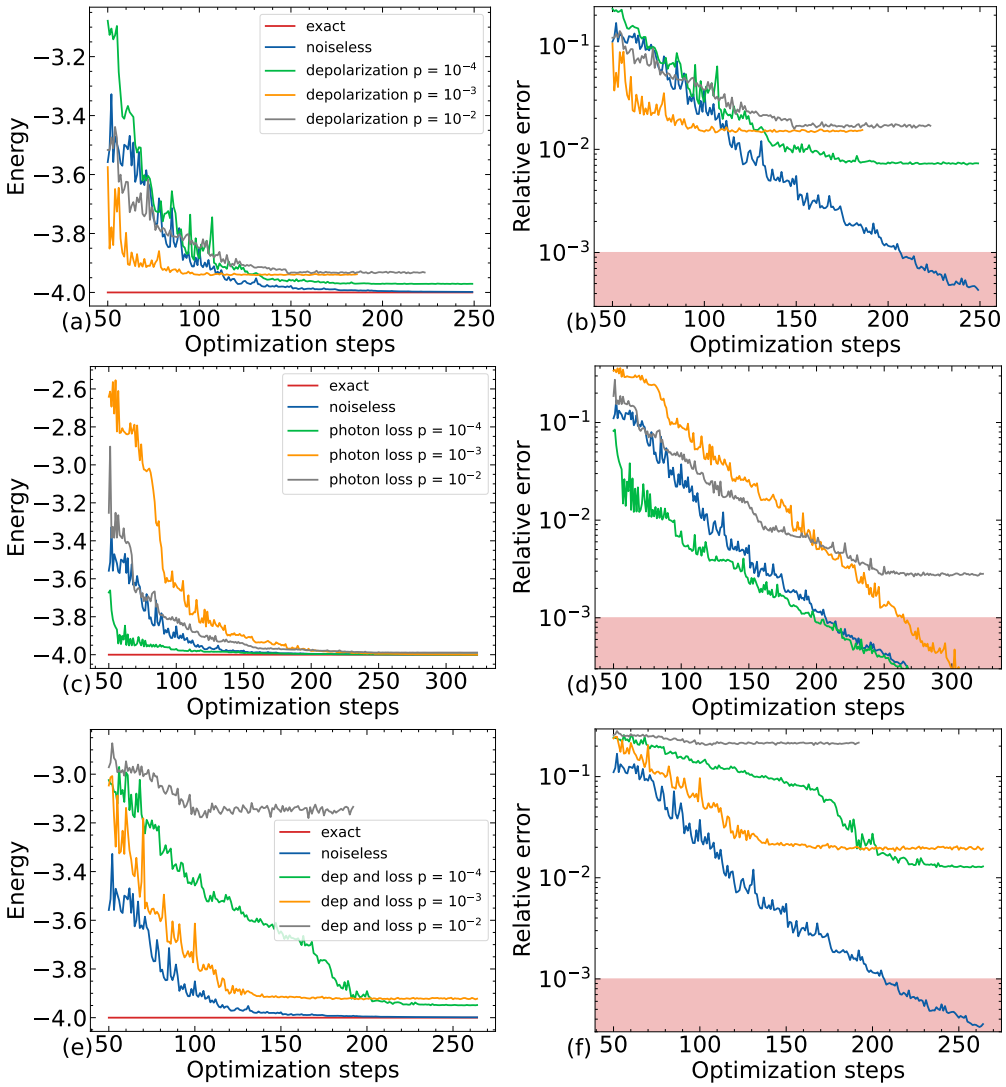

Figure 6.3: Panels (a), (c), and (e) show the optimization of the variational energy as a function of the number of optimization steps obtained with the simulations. Each curve is obtained by simulating the variational ansatz starting from random parameters. For visualization purposes, all panels start from the 50th optimization step. In each (a), (c) and (e) panels the red line is the exact energy $E_0 = -4$, the blue curve is the optimization in the noiseless case (which is the same curve in all plots), the orange, green and grey curves are obtained with an error probability of 10^{-4}, 10^{-3}, 10^{-2} respectively. Figures (b), (d), and (f) show the relative errors $|(E_0 - E)/E_0|$ as a function of the training steps. Colors of the curves have the same meaning of the upper panels. A 0.1% relative error threshold is here highlighted with a red shaded region for better visualization.

	$p = 10^{-4}$	$p = 10^{-3}$	$p = 10^{-2}$
Depolarization	0.9927	0.9846	0.9831
Photon Loss	0.999998	0.999985	0.997180
Dep and Loss	0.9875	0.9808	0.7835

Table 6.1: Values of the approximation ratio for different types of noises and for increasing order of magnitude of the error probability.

6.5 Discussion

We have extended the noisy gates approach derived in Chapter 4 to simulate noisy optical circuits, within the second quantization framework (see sections 6.2 and 6.2.3), which is used to perform classical simulations in the dual rail encoding for linear optics quantum computing.

We have shown that the simulations are suitable to describe variational problems in the presence of noises. The next target is to extend the analysis to the Quantum Approximate Optimization Algorithm (QAOA) [90] for the max K-cut problem developed in [86] in order to understand the practical applicability of a noisy algorithm on optical circuits.

Differently from Chapter 5, we did not compare our simulations with the output of optical devices available in the cloud, for example the one recently provided by Quandela [91]. This will be the subject of further investigations.

Finally the developed techniques can be used to mitigate more effectively noises on photonic circuits where the practical application of error mitigation is currently less explored with respect to solid state devices.

Chapter 7

Quantum algorithm to simulate open systems

In this chapter we apply the unitary unraveling introduced in Sec. 3.1.4 devising a quantum algorithm to simulate open quantum system evolution. We show how linearity and most importantly unitarity of Eq. (3.34) allow to drive the system evolution on a quantum computer.

The proposed algorithm presents two advancements. First and most notably, we show that it is always possible to drive the open system dynamics via a repetition of unitary gates applied to a set of n system qubits and a single ancillary bath qubit, representing the environment. This marks a significant reduction in the total width, i.e. total number of circuit qubits, with respect to similar approaches [92–97] where the ancilla overhead is at best polynomial in the system size n. Second, building upon the results of the noisy gates approach, the algorithm reproduces a perturbative approximation of the full Lindblad equation as in Eq. (3.6). This approximation allows to reach a target accuracy while reducing the depth of the circuit as a smaller number of total steps is needed.

7.1 Approximate solution of the unitary unraveling

In this section we first define a suitable finite representation of the bath operators $\mathrm{d}\hat{B}_k(t)$ and $\mathrm{d}\hat{B}_k^\dagger(t)$ and then we derive the approximate expression of the unitary evolution in Eq. (3.37).

7.1.1 Finite representation of the bath operators

As already pointed out, the unravelling in Eq. (3.34) acts on the full system-environment space and it is linear: for a given state at time t, the state at time $t+\Delta t$ is obtained as

$$|\Psi(t+\Delta t)\rangle = \hat{\mathrm{N}}_g(\Delta t)\,|\Psi(t)\rangle\,, \tag{7.1}$$

where $\hat{\mathrm{N}}_g(\Delta t)$ is also a unitary operator. Unitarity makes $\hat{\mathrm{N}}_g(\Delta t)$ implementable on a quantum computer. To do so, as explained in Sec. 3.1.4, one must find a suitable finite representation for the operators $\mathrm{d}\hat{B}_k(t)$ and $\mathrm{d}\hat{B}_k^\dagger(t)$, which are, in principle, operators acting on the infinite dimensional Hilbert space of the thermal baths representing the environment. We proceed as follows. Given a time interval over which we are interested in evaluating the dynamics, we divide it in time steps Δt assuming that during each step the system interacts only with a small portion of the bath, and being the bath of infinite dimension, the portion with which the system is interacting changes at each time step. Effectively we couple the system to a single ancillary qubit initialized in the ground state, representing a part of the bath, evolve the full system-bath qubit state for Δt and then reset the bath qubit to its ground state as if in the following time step the system is interacting with another portion of the bath. This idea leads to the following choice for the finite representation of the bath operators

$$\mathrm{d}\hat{B}_k(t) = \hat{\sigma}_E^-\mathrm{d}W_k(t), \quad \mathrm{d}\hat{B}_k^\dagger(t) = \hat{\sigma}_E^+\mathrm{d}W_k(t), \tag{7.2}$$

where $\hat{\sigma}_E^- = |0\rangle_E\langle 1|_E$, $\hat{\sigma}_E^+ = |1\rangle_E\langle 0|_E$ and $\mathrm{d}W_k(t)$ are classical Wiener processes. These definitions have to be complemented with the following prescriptions

1. Substitute $\mathbb{E}_{\mathrm{Q}}[\,\cdot\,]$ with $\mathbb{E}_{\mathrm{C}}[\mathrm{Tr}_{\mathrm{E}}(\hat{\rho}_{\mathrm{in}}\,\cdot\,)]$, where $\mathbb{E}_C[\,\cdot\,]$ is the average over classical stochastic processes $\mathrm{d}W_k(t)$ and $\hat{\rho}_{\mathrm{in}} = |0\rangle_E\langle 0|_E$ is the ground state of the bath qubit;

2. At each time step Δt the state is factorized as $|\Psi\rangle = |\psi\rangle_S\,|0\rangle_{\mathrm{E}}$;

3. The density matrix of the system has to be computed as $\hat{\rho}_S = \mathbb{E}_C[\mathrm{Tr}_{\mathrm{E}}(|\Psi\rangle\langle\Psi|)]$.

In this way, not only the statistical properties of quantum Wiener increments in Eq. (3.33) are satisfied but also, $\hat{\rho}_S = \mathbb{E}_C[\mathrm{Tr}_{\mathrm{E}}(|\Psi\rangle\langle\Psi|)]$ is a solution of the Lindblad equation in Eq. (3.36). Prescription two follows directly from the fact that in the finite dimensional representation the bath qubit has to be reset after each time step to preserve Markovianity; the first and the third prescriptions are due to the necessity to average over classical stochastic processes. To check the equivalence with the Lindblad equation, we substitute the finite representation of the bath operators in

Eq. (7.2) inside the first line of Eq. (3.36) and we apply the third prescription to get

$$\begin{aligned}
\mathrm{d}\hat{\rho}_S =& \mathbb{E}_C\Bigg[-\frac{i}{\hbar}[\hat{H}_{\mathrm{S}},\hat{\rho}_S]\mathrm{d}t - \frac{\gamma}{2}\{\hat{L}^\dagger\hat{L},\hat{\rho}_S\}\mathrm{d}t + \sqrt{\gamma}\hat{L}\mathrm{d}W\,\mathrm{Tr}_{\mathrm{E}}\big(\hat{\sigma}_E^+ |\Psi\rangle\langle\Psi|\big) \\
&- \sqrt{\gamma}\hat{L}^\dagger\mathrm{d}W\,\mathrm{Tr}_{\mathrm{E}}\big(\hat{\sigma}_E^- |\Psi\rangle\langle\Psi|\big) + \sqrt{\gamma}\,\mathrm{Tr}_{\mathrm{E}}\big(|\Psi\rangle\langle\Psi|\,\hat{\sigma}_E^-\big)\hat{L}^\dagger\mathrm{d}W \\
&- \sqrt{\gamma}\,\mathrm{Tr}_{\mathrm{E}}\big(|\Psi\rangle\langle\Psi|\,\hat{\sigma}_E^+\big)\hat{L}\mathrm{d}W + \gamma\hat{L}\,\mathrm{Tr}_{\mathrm{E}}\big(|\Psi\rangle\langle\Psi|\,\hat{\sigma}_E^-\hat{\sigma}_E^+\big)\hat{L}^\dagger\mathrm{d}t \\
&- \gamma\hat{L}\,\mathrm{Tr}_{\mathrm{E}}\big(|\Psi\rangle\langle\Psi|\,\hat{\sigma}_E^+\hat{\sigma}_E^+\big)\hat{L}\mathrm{d}t - \gamma\hat{L}^\dagger\,\mathrm{Tr}_{\mathrm{E}}\big(|\Psi\rangle\langle\Psi|\,\hat{\sigma}_E^-\hat{\sigma}_E^-\big)\hat{L}^\dagger\mathrm{d}t \\
&+ \gamma\hat{L}^\dagger\,\mathrm{Tr}_{\mathrm{E}}\big(|\Psi\rangle\langle\Psi|\,\hat{\sigma}_E^+\hat{\sigma}_E^-\big)\hat{L}\mathrm{d}t\Bigg].
\end{aligned} \tag{7.3}$$

By using the fact that $(\hat{\sigma}_E^\pm)^2 = 0$, $\hat{P}_0 = |0\rangle_E\langle 0|_E = \hat{\sigma}_E^-\hat{\sigma}_E^+$ and $\hat{P}_1 = |1\rangle_E\langle 1|_E = \hat{\sigma}_E^+\hat{\sigma}_E^-$ and that $\mathbb{E}_C[\mathrm{d}W] = 0$, Eq. (7.3) becomes

$$\begin{aligned}
\mathrm{d}\hat{\rho}_S =& -\frac{i}{\hbar}[\hat{H}_{\mathrm{S}},\hat{\rho}_S]\mathrm{d}t - \frac{\gamma}{2}\{\hat{L}^\dagger\hat{L},\hat{\rho}_S\}\mathrm{d}t \\
&+ \gamma\hat{L}\,\mathrm{Tr}_{\mathrm{E}}\big(|\Psi\rangle\langle\Psi|\,\hat{P}_0\big)\hat{L}^\dagger\mathrm{d}t + \gamma\hat{L}^\dagger\,\mathrm{Tr}_{\mathrm{E}}\big(|\Psi\rangle\langle\Psi|\,\hat{P}_1\big)\hat{L}\mathrm{d}t\,.
\end{aligned} \tag{7.4}$$

This is the Lindblad equation. Indeed, since we are assuming that $|\Psi\rangle = |\psi\rangle_S|0\rangle_{\mathrm{E}}$ is always valid, the $\hat{P}_1$ term contribution is zero and

$$\mathrm{Tr}_{\mathrm{E}}\big(|\Psi\rangle\langle\Psi|\,\hat{P}_0\big) = |\psi\rangle_S\langle\psi|_S\langle 0|_E\,\hat{P}_0\,|0\rangle_E = |\psi\rangle_S\langle\psi|_S = \hat{\rho}_S\,. \tag{7.5}$$

We mention that in principle it is possible to introduce non-Markovian effects by relaxing the second prescription, without resetting the bath qubit after each time step.

7.1.2 Derivation

Given the finite representation of the bath operators, we derive the approximate expression for the unitary evolution $\hat{\mathrm{N}}_g(\Delta t)$.

The derivation uses the *small noise expansion* [20] method introduced in Chapter 4, adapted and generalized to the rules of quantum Itô calculus, see Sec. 3.1.4 and also [19,22]. For simplicity the following derivation is performed by using the generic expression for $\mathrm{d}\hat{B}_t$ and $\mathrm{d}\hat{B}_t^\dagger$; the same results apply when substituting their finite expression in Eq. (7.2) and by applying the three prescriptions in Sec. 7.1.1.

We consider the QSDE in Eq. (3.34) with one single Lindblad operator, the generalization to $2^{2n}-1$ Lindblad operators being straightforward

$$\mathrm{d}|\Psi_t\rangle = \Big[-\frac{i}{\hbar}\hat{H}\mathrm{d}t + \epsilon\big(\hat{L}\mathrm{d}\hat{B}_t^\dagger - \hat{L}^\dagger\mathrm{d}\hat{B}_t\big) - \frac{\epsilon^2}{2}\hat{L}^\dagger\hat{L}\mathrm{d}t\Big]\,|\Psi_t\rangle\,, \tag{7.6}$$

and we set $\epsilon := \sqrt{\gamma}$. We assume the following perturbative expansion up to order ϵ^2

$$|\Psi_t\rangle = \left|\Psi_t^0\right\rangle + \epsilon \left|\Psi_t^1\right\rangle + \epsilon^2 \left|\Psi_t^2\right\rangle + \mathcal{O}(\epsilon^3)\,. \tag{7.7}$$

Substituting this expression into Eq. (7.6) and equating terms with the same power of ϵ, we obtain the following system of QSDEs

$$\begin{aligned}
\mathrm{d}\left|\Psi_t^0\right\rangle &= -\frac{i}{\hbar}\hat{H}\left|\Psi_t^0\right\rangle \mathrm{d}t \\
\mathrm{d}\left|\Psi_t^1\right\rangle &= -\frac{i}{\hbar}\hat{H}\left|\Psi_t^1\right\rangle \mathrm{d}t + \left(\hat{L}\mathrm{d}\hat{B}_t^\dagger - \hat{L}^\dagger \mathrm{d}\hat{B}_t\right)\left|\Psi_t^0\right\rangle \\
\mathrm{d}\left|\Psi_t^2\right\rangle &= -\frac{i}{\hbar}\hat{H}\left|\Psi_t^2\right\rangle \mathrm{d}t + \left(\hat{L}\mathrm{d}\hat{B}_t^\dagger - \hat{L}^\dagger \mathrm{d}\hat{B}_t\right)\left|\Psi_t^1\right\rangle - \frac{1}{2}\hat{L}^\dagger\hat{L}\left|\Psi_t^0\right\rangle \mathrm{d}s,
\end{aligned}$$

which has to be solved with the initial conditions $|\Psi_0^0\rangle = |\Psi_0\rangle$. The zero-th order differential equation is the deterministic equation given by the system Hamiltonian evolution, with solution $|\Psi_t^0\rangle = \hat{U}(t-t_0)\,|\Psi_{t_0}\rangle$. The solution of the first order QSDE is

$$\left|\Psi_t^1\right\rangle = \hat{U}(t-t_0)\hat{\mathrm{S}}(t-t_0)\,|\Psi_{t_0}\rangle\,, \tag{7.8}$$

where we introduced the stochastic term $\hat{\mathrm{S}}(t-t_0) := \int_{t_0}^t (\hat{L}(s-t_0)\mathrm{d}\hat{B}_s^\dagger - \hat{L}^\dagger(s-t_0)\mathrm{d}\hat{B}_s)$ with $\hat{L}(s-t_0) = \hat{U}^\dagger(s-t_0)\hat{L}\hat{U}(s-t_0)$. The solution to the second order QSDE is

$$\left|\Psi_t^2\right\rangle = -\hat{U}(t-t_0)\int_{t_0}^t \left[\frac{1}{2}\hat{L}^\dagger(s-t_0)\hat{L}(s-t_0)\mathrm{d}s - (\hat{L}(s-t_0)\mathrm{d}\hat{B}_s^\dagger - \hat{L}^\dagger(s-t_0)\mathrm{d}\hat{B}_s)\hat{\mathrm{S}}(s-t_0)\right]|\Psi_{t_0}\rangle\,. \tag{7.9}$$

Then, up to order ϵ^2, $|\Psi_{t+\Delta t}\rangle = \hat{\mathrm{N}}_g(\Delta t)\,|\Psi_t\rangle + \mathcal{O}(\epsilon^3)$, where the evolution operator is $\hat{\mathrm{N}}_g(\Delta t) = \hat{U}(\Delta t)\hat{\mathrm{N}}(\Delta t)$, with

$$\begin{aligned}
\hat{\mathrm{N}}(\Delta t) = \mathbb{1} + \epsilon\hat{\mathrm{S}}(\Delta t) - \frac{\epsilon^2}{2}\int_t^{t+\Delta t} \hat{L}^\dagger(s-t)\hat{L}(s-t)\mathrm{d}s \\
+ \epsilon^2 \int_t^{t+\Delta t} \left(\hat{L}(s-t)\mathrm{d}\hat{B}_s^\dagger - \hat{L}^\dagger(s-t)\mathrm{d}\hat{B}_s\right)\hat{\mathrm{S}}(s-t).
\end{aligned} \tag{7.10}$$

To simplify this expression, we make use of the following equality, which is the generalization of Eq. (4.9) to the rules of quantum Itô calculus [19, 20]

$$\int_{t_0}^t \left(\hat{L}(s-t_0)\mathrm{d}\hat{B}_s^\dagger - \hat{L}^\dagger(s-t_0)\mathrm{d}\hat{B}_s\right)\hat{\mathrm{S}}(s-t_0) = \frac{1}{2}\left[\hat{\mathrm{S}}^2(t-t_0) + \int_{t_0}^t \mathrm{d}s\hat{L}^\dagger(s-t_0)\hat{L}(s-t_0) - \hat{\mathrm{C}}(t-t_0)\right], \tag{7.11}$$

where $\hat{\mathrm{C}}(t-t_0) = \frac{1}{2}\int_{t_0}^t \left[\hat{\mathrm{S}}(s-t_0), \hat{L}(s-t)\mathrm{d}\hat{B}_s^\dagger - \hat{L}^\dagger(s-t)\mathrm{d}\hat{B}_s\right]$. By substituting this expression into Eq. (7.10), we have to order ϵ^2

$$\hat{\mathrm{N}}(\Delta t) = \mathbb{1} + \epsilon\hat{\mathrm{S}}(\Delta t) + \frac{\epsilon^2}{2}\hat{\mathrm{S}}(\Delta t)^2 - \epsilon^2\hat{\mathrm{C}}(\Delta t) \tag{7.12}$$

We can drop the term $\epsilon^2\hat{\mathrm{C}}(\Delta t)$, which in principle contributes to order ϵ^2 to the final density matrix, because it is a nested Itô integral of non anticipating functions [19,20] (see also Sec. 4.1.1), and hence its stochastic average is zero.

Generalizing to the case of multiple Lindblad operators $\hat{L}_k$, reinserting the coefficients γ_k and approximating the series expansion in $\hat{S}$ to an exponential, the final expression for $\hat{\mathrm{N}}_g(\Delta t)$ is

$$\hat{\mathrm{N}}_g(\Delta t) \simeq \hat{U}(\Delta t)\exp\left(\sum_k \sqrt{\gamma_k}\hat{\mathrm{S}}_k(\Delta t)\right) \simeq \hat{U}(\Delta t)\prod_k \exp\left(\sqrt{\gamma_k}\hat{S}_k(\Delta t)\right), \tag{7.13}$$

where $\hat{U}(\Delta t)$ is the closed system evolution operator and the stochastic terms $\hat{\mathrm{S}}_k(\Delta t)$ read

$$\hat{\mathrm{S}}_k(\Delta t) = \int_t^{t+\Delta t}\left(\hat{L}_k(s-t)d\hat{B}_k^\dagger(s) - \hat{L}_k^\dagger(s-t)d\hat{B}_k(s)\right), \tag{7.14}$$

where $\hat{L}_k(s-t) = \hat{U}^\dagger(s-t)\hat{L}_k\hat{U}(s-t)$ are the Lindblad operators in the interaction picture. Eq. (7.13) is equivalent to the following approximate density matrix of the system

$$\begin{aligned}&\hat{\rho}_S(t+\Delta t) = \mathrm{Tr}_E(\hat{N}(\Delta t)\hat{\rho}_S(t)\hat{N}^\dagger(\Delta t)) = \\ &\hat{U}(\Delta t)\left(\hat{\rho}_S(t) + \int_t^{t+\Delta t}\mathrm{d}s\mathcal{L}_D(s)\hat{\rho}_S(t)\right)\hat{U}^\dagger(\Delta t)\end{aligned} \tag{7.15}$$

where

$$\mathcal{L}_D(s)\hat{\rho}_S(t) = \sum_k \gamma_k\left(\hat{L}_k(s)\hat{\rho}_S(t)\hat{L}_k^\dagger(s) - \frac{1}{2}\left\{\hat{L}_k^\dagger(s)\hat{L}_k(s), \hat{\rho}_S(t)\right\}\right). \tag{7.16}$$

Notably, this is the same approximate expression in Eq. (3.6).

We remark that the second approximation in Eq. (7.13) is legitimate since on

average

$$\mathbb{E}_C\Big[\mathrm{Tr}_E\Big(\prod_k e^{\sqrt{\gamma_k}\hat{S}_k(\Delta t)}\hat{\rho}_S(0)\,|0\rangle\,\langle 0|\prod_j e^{\sqrt{\gamma_j}\hat{S}_j^\dagger(\Delta t)}\Big)\Big] =$$

$$\mathbb{E}_C\big[\mathrm{Tr}_E\Big(\prod_k\big(\mathbb{1}+\sqrt{\gamma_k}\hat{S}_k(\Delta t)+\frac{1}{2}\gamma_k\hat{S}_k^2(\Delta t)\big)\hat{\rho}_S(0)\,|0\rangle\,\langle 0|$$

$$\prod_j\big(\mathbb{1}+\sqrt{\gamma_j}\hat{S}_j^\dagger(\Delta t)+\frac{1}{2}\gamma_j\hat{S}_j^{\dagger 2}(\Delta t)\big)\Big)\Big] =$$

$$\mathbb{E}_C\big[\mathrm{Tr}_E\Big(\big(\mathbb{1}+\sum_k\sqrt{\gamma_k}\hat{S}_k(\Delta t)+\frac{1}{2}\sum_k\gamma_k\hat{S}_k^2(\Delta t)+\sum_{k<k'}\sqrt{\gamma_k}\sqrt{\gamma_{k'}}\hat{S}_k(\Delta t)\hat{S}_{k'}(\Delta t)\big)\hat{\rho}_S(0)\,|0\rangle\,\langle 0|$$

$$(\mathbb{1}+\sum_j\sqrt{\gamma_j}\hat{S}_j^\dagger(\Delta t)+\frac{1}{2}\sum_j\gamma_j\hat{S}_j^{2\dagger}(\Delta t)+\sum_{j<j'}\sqrt{\gamma_j}\sqrt{\gamma_{j'}}\hat{S}_j^\dagger(\Delta t)\hat{S}_{j'}^\dagger(\Delta t))\Big)\Big] =$$

$$\hat{\rho}_S(t)+\int_t^{t+\Delta t}\mathrm{d}s\mathcal{L}_D(s)\hat{\rho}_S(t) \tag{7.17}$$

where $\mathcal{L}_D(s)\hat{\rho}_S(t)$ is the same term in Eq. (7.16) and we use the fact that

$$\begin{aligned}&\mathbb{E}_C\big[\mathrm{Tr}_E\Big(\sqrt{\gamma_k}\sqrt{\gamma_{k'}}\hat{S}_k(\Delta t)\hat{S}_{k'}(\Delta t)\hat{\rho}_S(0)\,|0\rangle\,\langle 0|\Big)\big]\\&=\mathbb{E}_C\big[\mathrm{Tr}_E\Big(\sqrt{\gamma_k}\sqrt{\gamma_{k'}}\hat{\rho}_S(0)\,|0\rangle\,\langle 0|\,\hat{S}_k(\Delta t)\hat{S}_{k'}(\Delta t)\Big)\big]=0.\end{aligned} \tag{7.18}$$

since Wiener processes associated to different k are statistically independent. Thus, instead of computing $\exp\Big(\sum_k\sqrt{\gamma_k}\hat{\mathrm{S}}_k(\Delta t)\Big)$, we compute a matrix for each Lindblad operator and then multiply them as $\prod_k\exp\Big(\sqrt{\gamma_k}\hat{\mathrm{S}}_k(\Delta t)\Big)$. Each matrix $\exp\Big(\sqrt{\gamma_k}\hat{S}_k(\Delta t)\Big)$ has dimension $2\times\max(d_U,d_L)$ with d_U and d_L the dimensions of the unitary evolution and of the Lindblad operators respectively. The factor "2" accounts for the bath qubit while the second term is a consequence of the fact that each $\hat{\mathrm{S}}_k(\Delta t)$ contains $\hat{L}_k(s-t)=\hat{U}^\dagger(s-t)\hat{L}_k\hat{U}(s-t)$. Remarkably, all matrices in the product are implemented by using the same unique ancillary bath qubit that, according to the second prescription, has to be reset after the application of all operators in $\prod_k\exp\Big(\sqrt{\gamma_k}\hat{\mathrm{S}}_k(\Delta t)\Big)$.

Inserting the finite representation (7.2) of the bath operators inside the stochastic terms in Eq. (7.14) they become

$$\hat{\mathrm{S}}_k(\Delta t)=\int_t^{t+\Delta t}\Big(\hat{L}_k(s-t)\hat{\sigma}_E^+-\hat{L}_k^\dagger(s-t)\hat{\sigma}_E^-\Big)\mathrm{d}W_k(s). \tag{7.19}$$

For convenience we define $\hat{J}_k(s-t)\equiv\hat{L}_k(s-t)\hat{\sigma}_E^+-\hat{L}_k^\dagger(s-t)\hat{\sigma}_E^-$. The real $[\hat{\mathrm{S}}_k(\Delta t)]_{ij}^R$ and imaginary part $[\hat{\mathrm{S}}_k(\Delta t)]_{ij}^I$ of the entries of the operators $\hat{\mathrm{S}}_k(\Delta t)$ in Eq. (7.19)

are Itô integrals of deterministic functions $[\hat{\mathrm{S}}_k(\Delta t)]^{\lambda}_{ij} = \int_t^{t+\Delta t} \mathrm{d}W_k(s)[\hat{J}_k(s-t)]^{\lambda}_{ij}$ for $\lambda = R, I$, that represent Gaussian stochastic processes with means zero

$$\mathbb{E}\big[[\hat{\mathrm{S}}_k(\Delta t)]^{\lambda}_{ij}\big] = 0 \tag{7.20}$$

and variances and covariances

$$\mathbb{V}\big[[\hat{\mathrm{S}}_k(\Delta t)]^{\lambda}_{ij}\big] = \int_t^{t+\Delta t} \mathrm{d}s([\hat{J}_k(s-t)]^{\lambda}_{ij})^2 \tag{7.21}$$

$$\mathbb{E}\big[[\hat{\mathrm{S}}_k(\Delta t)]^{\lambda}_{ij}[\hat{\mathrm{S}}_k(\Delta t)]^{\lambda'}_{i'j'}\big] = \int_t^{t+\Delta t} \mathrm{d}s[\hat{J}_k(s-t)]^{\lambda}_{ij}[\hat{J}_k(s-t)]^{\lambda'}_{i'j'} \tag{7.22}$$

Once all the variances and covariances are computed, the stochastic processes can be sampled to get a single realization of the evolution operator $\hat{\mathrm{N}}_g(\Delta t)$. Finally by averaging over all the realizations of the final state $|\Psi(t+\Delta t)\rangle = \hat{\mathrm{N}}_g(\Delta t)\,|\Psi(t)\rangle$, in accordance with the prescriptions, one obtains the final density matrix in Eq. (7.15).

7.2 The quantum algorithm

In this section we describe the quantum algorithm driving the open system evolution and we upper bound the error associated to the approximate solution, evaluating the resources needed to reach a target accuracy.

7.2.1 Implementation

The approximate expression of the unitary evolution of system qubits plus the ancillary qubit in Eq. (7.13) is not directly implementable on a quantum computer when $\hat{U}$ is the unitary of a full many body system and for noises acting long range over many qubits. In this setup, the dimension $2 \times \max(d_U, d_L)$ of $\hat{\mathrm{N}}_g(\Delta t)$ scales exponentially with the number of system qubits n, as both d_L and d_U do. This makes the computation of such matrices, and the consequent characterization of their stochastic processes, unfeasible computationally as the system size n increases. To avoid this problem, from now on we assume that the noises have a defined m locality, meaning that d_L is at most $m < n$ and m is independent on n. To further reduce the dimension of the gates to be computed, we decompose the ideal many body system evolution into the native gates $\hat{U}^{\sigma}$ of a given device and apply Eq. (7.13) to each $\hat{U}^{\sigma}$. In this case calculations are straightforward since $\hat{U}^{\sigma}$ act on a very limited number of system qubits and $\hat{L}$ have a fixed dimension. This results in the algorithmic implementation of the approach, presented in Alg. 4.

Algorithm 4

Input: A Lindblad equation and a certain number n_g of native gates of the quantum device $\{\hat{U}^{(1)}, ..., \hat{U}^{(n_g)}\}$.

Protocol:

1. For each $\hat{U}^{(\sigma)}$ compute $\hat{\mathrm{N}}^{(\sigma)}$ by using equation (7.13) in its finite representation, getting $\{\hat{\mathrm{N}}^{(1)}, ..., \hat{\mathrm{N}}^{(n_g)}\}$

2. Trotterize the unitary evolution of the system in $\Delta\tau$ time steps as $\hat{\mathcal{U}}(T,0) \simeq \prod_j^{N_{\text{step}}} \hat{\mathcal{U}}_j(\Delta\tau)$ where $T = N_{\text{step}}\Delta\tau$.

3. Decompose the quantum circuit corresponding to $\prod_j^{N_{\text{step}}} \hat{\mathcal{U}}_j(\Delta\tau)$ into the native gates.

4. Substitute each gate in the circuit with the corresponding $\hat{\mathrm{N}}^{(\sigma)}(\Delta t)$ where $\Delta t = \Delta\tau/N_{gates}$ and N_{gates} is the total number of native gates in the trotter step.

5. Apply all the trotter steps making sure to reset the ancilla qubit after the application of each $\hat{\mathrm{N}}^{(\sigma)}$.

6. Repeat the resulting circuit by sampling the stochastic processes inside $\hat{\mathrm{N}}^{(\sigma)}$ for each measurement shot.

Output: Compute the final probabilities by taking the average over all circuit realizations.

In general the operators $\hat{\mathrm{N}}^{(\sigma)}$ obtained after step 1 are not anymore native gates but they are further decomposed into native gates when the circuit runs. The choice of time step Δt in the fourth step of Alg. 4 is made such that the time step $\Delta\tau$ is reached after the N_{gates}, i.e. $\Delta\tau = N_{gates}\Delta t$.

7.2.2 Resources estimation

We now estimate the resources needed for the implementation of Alg. 4. To do so, we compute an upper bound on the approximation error between the approximate density matrix in Eq. (7.13) and the full solution of the Lindblad equation (see also Eq. (2.15))

$$\hat{\rho}_S(t+\Delta t) = \hat{U}(\Delta t)\mathrm{T}\Big[e^{\int_t^{t+\Delta t}\mathrm{d}s\mathcal{L}_D(s)}\Big]\hat{\rho}_S(t)\hat{U}^\dagger(\Delta t)\,. \tag{7.23}$$

The approximation error is quantified by

$$\varepsilon_a = \Big\|\mathrm{T}\big[e^{\int_t^{t+\Delta t}\mathrm{d}s\mathcal{L}_D(s)}\big] - (\mathbb{1} + \int_t^{t+\Delta t}\mathrm{d}s\mathcal{L}_D(s))\Big\|_{1\to 1} \tag{7.24}$$

where we use the $1 \to 1$ superoperator norm $\|\mathcal{E}\|_{1\to 1} \equiv \sup_{\|\hat{O}\|_1=1} \left\|\mathcal{E}(\hat{O})\right\|_1$ [92, 98] where $\left\|\hat{O}\right\|_1 \equiv \mathrm{Tr}\left(\sqrt{\hat{O}^\dagger \hat{O}}\right)$ and $\mathcal{E}(\,\cdot\,)$ is a generic superoperator. We quantify this error by assuming m-locality, for which the Lindbladian can be expressed as $\mathcal{L}_D(s) = \sum_j^K \mathcal{L}_j(s)$ where each $\mathcal{L}_j(s)$ acts non trivially on a subset of $m < n$ qubits. Each $\mathcal{L}_j(s)$ has a maximum number $2^{2m} - 1$ of Lindblad operators. For simplicity we assume that all noise parameters γ_k have the same order of magnitude $\gamma_k = \gamma$. By using the fact that $\gamma \Delta t \ll 1$, thus $\int_t^{t+\Delta t} \mathrm{d}s \|\mathcal{L}_D(s)\|_{1\to 1} < 1$ and the inequalities $\|\mathcal{E}_1 + \mathcal{E}_2\|_{1\to 1} \leq \|\mathcal{E}_1\|_{1\to 1} + \|\mathcal{E}_2\|_{1\to 1}$, $\|\mathcal{E}_1 \mathcal{E}_2\|_{1\to 1} \leq \|\mathcal{E}_1\|_{1\to 1} \|\mathcal{E}_2\|_{1\to 1}$ the approximation error is upper bounded as

$$
\begin{aligned}
\varepsilon_a &= \left\| \mathrm{T}\left[e^{\int_t^{t+\Delta t} \mathrm{d}s \mathcal{L}_D(s)} \right] - \left(\mathbb{1} + \int_t^{t+\Delta t} \mathrm{d}s \mathcal{L}_D(s) \right) \right\|_{1\to 1} \\
&= \left\| \sum_{k=2}^{\infty} \frac{1}{k!} \int_t^{t+\Delta t} \cdots \int_t^{t+\Delta t} \mathrm{d}t_1 \ldots \mathrm{d}t_k \mathrm{T}\Big[\mathcal{L}_D(t_1) \ldots \mathcal{L}_D(t_k) \Big] \right\|_{1\to 1} \\
&\leq \sum_{k=2}^{\infty} \frac{1}{k!} \left\| \int_t^{t+\Delta t} \cdots \int_t^{t+\Delta t} \mathrm{d}t_1 \ldots \mathrm{d}t_k \mathrm{T}\Big[\mathcal{L}_D(t_1) \ldots \mathcal{L}_D(t_k) \Big] \right\|_{1\to 1} \\
&= \sum_{k=2}^{\infty} \frac{1}{k!} \left\| \mathrm{T}\left[\left(\int_t^{t+\Delta t} \mathrm{d}s \mathcal{L}_D(s) \right)^k \right] \right\|_{1\to 1} \leq \sum_{k=2}^{\infty} \frac{1}{k!} \left(\int_t^{t+\Delta t} \mathrm{d}s \|\mathcal{L}_D(s)\|_{1\to 1} \right)^k \\
&\leq \frac{1}{2} \left(\int_t^{t+\Delta t} \mathrm{d}s \|\mathcal{L}_D(s)\|_{1\to 1} \right)^2 \sum_{k=0}^{\infty} \frac{1}{k!} \left(\int_t^{t+\Delta t} \mathrm{d}s \|\mathcal{L}_D(s)\|_{1\to 1} \right)^k \\
&= \frac{1}{2} \left(\int_t^{t+\Delta t} \mathrm{d}s \|\mathcal{L}_D(s)\|_{1\to 1} \right)^2 e^{\int_t^{t+\Delta t} \mathrm{d}s \|\mathcal{L}_D(s)\|_{1\to 1}} \leq \frac{e}{2} \left(\int_t^{t+\Delta t} \mathrm{d}s \|\mathcal{L}_D(s)\|_{1\to 1} \right)^2,
\end{aligned}
\tag{7.25}
$$

where e is the Euler number.

Since $\mathcal{L}_D(s)$ is m-local, then $\|\mathcal{L}_D(s)\|_{1\to 1} \leq K \max_j \|\mathcal{L}_j(s)\|_{1\to 1}$, and $\|\mathcal{L}_j(s)\|_{1\to 1}$

can be expressed as

$$
\begin{aligned}
\|\mathcal{L}_j(s)\|_{1\to 1} &= \sup_{\|\hat{O}\|_1=1} \Big\| \sum_{k=1}^{2^{2m}-1} \gamma\Big((\hat{L}_{k,j}(s)\hat{O}\hat{L}^\dagger_{k,j}(s) - \frac{1}{2}\{\hat{L}^\dagger_{k,j}(s)\hat{L}_{k,j}(s),\hat{O}\}\Big)\Big\|_1 \\
&\leq \gamma \sum_{k=1}^{2^{2m}-1}\Big(\sup_{\|\hat{O}\|_1=1}\Big\|\hat{L}_{k,j}(s)\hat{O}\hat{L}^\dagger_{k,j}(s)\Big\|_1 + \frac{1}{2}\sup_{\|\hat{O}\|_1=1}\Big\|\{\hat{L}^\dagger_{k,j}(s)\hat{L}_{k,j}(s),\hat{O}\}\Big\|_1\Big) \\
&\leq 2\gamma \sum_{k=1}^{2^{2m}-1}\sup_{\|\hat{O}\|_1=1}\Big\|\hat{O}\Big\|_1\Big\|\hat{L}^\dagger_{k,j}(s)\Big\|_\infty\Big\|\hat{L}_{k,j}(s)\Big\|_\infty \leq 2\gamma \sum_{k=1}^{2^{2m}-1}\Big\|\hat{L}^\dagger_{k,j}(s)\Big\|_\infty\Big\|\hat{L}_{k,j}(s)\Big\|_\infty \\
&= 2\gamma \sum_{k=1}^{2^{2m}-1}\Big\|\hat{L}_{k,j}(s)\Big\|^2_\infty \leq 2\gamma(2^{2m}-1)\max_k\Big(\Big\|\hat{L}_{k,j}(s)\Big\|^2_\infty\Big) \\
&= 2\gamma(2^{2m}-1)\max_k\Big(\Big\|\hat{L}_{k,j}\Big\|^2_\infty\Big),
\end{aligned}
\tag{7.26}
$$

where we use the inequalities $\Big\|\hat{A}\hat{B}\Big\|_1 \leq \Big\|\hat{A}\Big\|_1\Big\|\hat{B}\Big\|_\infty$, $\Big\|\hat{A}\hat{B}\Big\|_1 \leq \Big\|\hat{A}\Big\|_\infty\Big\|\hat{B}\Big\|_1$ and $\Big\|\hat{A}\Big\|_\infty = \sup_{\||\psi\rangle\|=1}\Big\|\hat{A}\,|\psi\rangle\Big\| = \sup_{\||\psi\rangle\|=1}\sqrt{\langle\psi|\,\hat{A}^\dagger\hat{A}\,|\psi\rangle}$. Moreover we exploit the fact that $\Big\|\hat{L}_{k,j}(s)\Big\|^2_\infty = \sup_{\||\psi\rangle\|=1}\langle\psi|\,\hat{U}^\dagger(s,t)\hat{L}^\dagger_{k,j}\hat{L}_{k,j}\hat{U}(s,t)\,|\psi\rangle = \sup_{\||\psi'\rangle\|=1}\langle\psi'|\,\hat{L}^\dagger_{k,j}\hat{L}_{k,j}\,|\psi'\rangle = \Big\|\hat{L}_{k,j}\Big\|^2_\infty$. Finally by inserting Eq. (7.26) in Eq. (7.25) one finds

$$
\varepsilon_a \leq 2e\Big(K(2^{2m}-1)\max_k\Big\|\hat{L}_{k,j}\Big\|^2_\infty\gamma\Delta t\Big)^2. \tag{7.27}
$$

where $K(2^{2m}-1)$ is the total number of Lindblad operators. This number scales polynomially with n. Indeed K in general takes the value $n!/m!(n-m)!$, that for m-local Lindbladians and for n going to infinity, scales as

$$
K \sim \frac{n^m}{m!e^m}, \tag{7.28}
$$

where we use the Stirling formula.

Given Alg. 4, each $\hat{N}^{(\sigma)}$ contributes to the single trotter step error with ε_a. Then if in the trotter step there are N_{gates} and, according to the m-locality condition, the total number of Lindblad operators is $\sim n^m$, the single trotter step error is bounded by $\varepsilon_{step} \leq N_{gates}\varepsilon_a$. Consequently, the global approximation error associated to a total evolution time T is $\varepsilon_{global} \leq N_{step}\varepsilon_{step} \leq N_{step}N_{gates}\varepsilon_a \sim \frac{T^2}{N_{step}}N_{gates}n^{2m}\gamma^2$. Notably, this bound is polynomial in the system qubits number n.

Alg. 4 is based on the perturbative expression in Eq. (7.13), that, in principle, is valid when noises are small perturbations of the system unitary evolution. In this setup Δt is not restricted to be infinitesimal and our approach provides the approximate solution of the Lindblad equation in Eq. (7.15) which is more accurate in the non infinitesimal interval Δt than the more immediate and most commonly employed approximation given by $\hat{\rho}_S(t+\Delta t) = \hat{\rho}_S(t) + \left(-\frac{i}{\hbar}[\hat{H}_S, \hat{\rho}_S(t)] + \mathcal{L}_D\hat{\rho}_S(t)\right)\Delta t$, which is a first order approximation in Δt. This fact implies a huge advancement in terms of quantum resources. Given a target accuracy, the total number of time steps to reach a final evolution time T is greatly reduced, effectively reducing the total depth of the circuit. Since $\varepsilon_{tot} \leq N_{step}N_{gates}\varepsilon_a \sim \frac{T^2}{N_{step}}N_{gates}n^{2m}\gamma^2$ then less N_{step} are needed leading to a bigger Δt as long as $\gamma\Delta t \ll 1$. This is also confirmed by Fig. 7.1 (a).

When approaching the strong coupling regime, the perturbative expression is not valid anymore. However, the approach does not break down as long as the value of Δt is suitably decreased, becoming infinitesimal. In fact, in this limit Eq. (7.15) reduces to $\hat{\rho}_S(t+\Delta t) = \hat{\rho}_S(t) + \left(-\frac{i}{\hbar}[\hat{H}_S, \hat{\rho}_S(t)] + \mathcal{L}_D\hat{\rho}_S(t)\right)\Delta t$ and the stochastic terms in Eq. (7.14) become $\hat{\mathrm{S}}_k(\Delta t) = \sqrt{\gamma}_k\hat{J}_k W_k(\Delta t)$. The Wiener processes $W_k(\Delta t)$ have variances Δt, and for this reason in this regime the algorithm resembles a stochastic implementation of the algorithm proposed in [94, 95]. The significant difference is that in our case the system-environment interaction is mediated by a single ancillary qubit regardless of the total number of the system Lindblad operators.

Regarding the width of the resulting circuit, in general Alg. 4 needs a single environmental qubit, thus a constant ancilla overhead of order $\mathcal{O}(1)$. State of the art implementations [92–97] have ancilla overheads proportional to the number of Lindblad operators, which is generally of order $\mathcal{O}(2^{2n}-1)$ where n is the number of system qubits. For m-local Lindbladians, the order reduces to $\mathcal{O}(n^m)$, while for algorithms based on the vectorization of the density matrix, the ancilla overhead is of order $\mathcal{O}(n)$. This constitutes a huge advancement for our protocol: the total number of qubits to run the simulation is reduced polynomially and at most exponentially.

Our approach needs to evaluate multiple circuits due to the sampling of the stochastic processes. This leads to a sampling error on the evaluation of observables

$$\eta = \mathcal{O}(\sqrt{N_{step}\gamma\Delta t/\mathcal{N}_r}) \tag{7.29}$$

where $\mathcal{N}_r$ is the total number of realizations of the classical stochastic processes, γ is the system-environment coupling constant (for simplicity $\gamma_k = \gamma$ for all k) and $N_{step}\Delta t = T$ is the time duration of the evolution. η is independent on n and it scales with the square root of the depth of the circuit $d \sim \mathcal{O}(N_{step}\Delta t)$. This does not increase drastically the computational resources with respect to deterministic methods. This fact is checked in Fig. 7.1 (b).

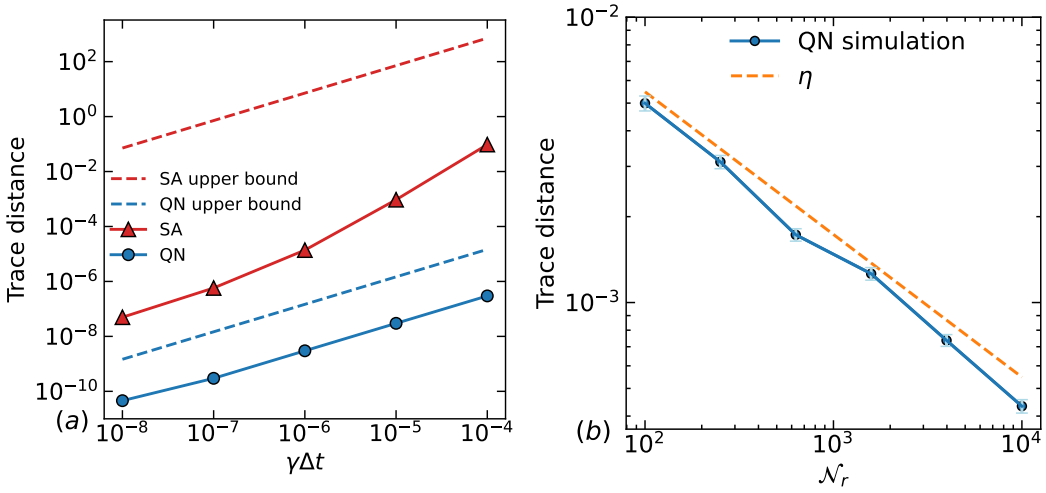

Figure 7.1: Evolution of a single spin under external magnetic field and in contact with a thermal bath with coupling constant $\gamma = 0.1\,\text{kHz}$, for a total time $T = 30\,\mu\text{s}$. Panel (a) displays in blue the trace distance $\mathcal{T}^{(QN)}(T)$ between the exact solution of the Lindblad equation and the quantum noise (QN) approximation in Eq. (7.15) as a function of $\gamma\Delta t$ and in red the trace distance $\mathcal{T}^{(SA)}(T)$ between the exact solution of the Lindblad equation and the standard approximation (SA). As one can see, to reach the same precision of QN, the SA needs $N_{step}^{(SA)} \sim 10^5$ against $N_{step}^{(QN)} \sim 10^1$, implying that the resulting depth for SA is four orders magnitude larger than for QN. The blue dashed line reports the theoretical upper bound for QN computed in Sec. 7.2.2, while the red dashed line is the theoretical upper bound for SA, computed by using the formula of [94]. Panel (b) plots in blue the trace distance $\mathcal{T}_{sampled}^{(QN)} = \mathcal{T}(\hat{\chi}(T), \hat{\rho}_{sampled}^{(QN)}(T))$ with fixed $\Delta t = 10^{-6}$ where $\hat{\rho}_{sampled}^{(QN)}(T)$ is obtained by simulating Alg. 4 for an increasing number N_r of realizations. Each point is the mean over 100 independent simulations, and the vertical bars show the standard deviations of the means. The orange dashed line is the sampling error $\eta = \mathcal{O}(\sqrt{\gamma N_{step}\Delta t/\mathcal{N}_r})$. By taking larger $\mathcal{N}_r$ one can reach the same precision of the rightmost point of the blue curve in (a); this requires a very large number of samples, but it is a consequence of the simple toy model we are considering, as explained in the main text.

Fig. 7.1 reports the results of the simulations of a single spin under external magnetic field. The system Hamiltonian is $H_S = \frac{\hbar\Omega}{2}\hat{X}$ with $\Omega = \pi/6\,\mathrm{MHZ}$ and the Lindblad operators are $\hat{L}_1 = \hat{\sigma}^+$, $\hat{L}_2 = \hat{\sigma}^-$ and $\hat{L}_3 = \hat{Z}$ driven by the same fixed noise parameter $\gamma = 0.1\,\mathrm{KHZ}$. The isolated dynamics of the system can be implemented by a single-qubit x-rotation $\hat{R}_x(\theta)$ in time steps Δt where $\theta = \Omega\Delta t$. We fix the total evolution time $T = 30\,\mu\mathrm{s}$ and we vary the value of Δt. In Fig. 7.1 (a) the solid blue line is the trace distance [2] $\mathcal{T}^{(QN)} = \mathcal{T}(\hat{\chi}(T), \hat{\rho}^{(QN)}(T))$ between $\hat{\rho}^{(QN)}(T)$, which is the density matrix obtained with the approximate expression in Eq. (7.15), and $\hat{\chi}(T)$, which is the analytic solution of the full Lindblad equation. The global upper bound coming from Eq. (7.27) is reported with the blue dashed line. The values of $\mathcal{T}^{(QN)}$ are always below the upper bound, confirming its validity. The solid red line displays the behaviour of $\mathcal{T}^{(SA)} = \mathcal{T}(\hat{\chi}(T), \hat{\rho}^{(SA)}(T))$ where $\hat{\rho}^{(SA)}(T)$ is obtained using the approximation $\hat{\rho}_S(t+\Delta t) = \hat{\rho}_S(t) + \big(-\frac{i}{\hbar}[\hat{H}_S, \hat{\rho}_S(t)] + \mathcal{L}_D\hat{\rho}_S(t)\big)\Delta t$. The associated upper bound, computed using the formulas in [94], is displayed with the red dashed line. Notably, for $\gamma\Delta t \sim 10^{-4}$, $\mathcal{T}^{(QN)} \sim 10^{-7}$ while $\mathcal{T}^{(SA)} \sim 10^{-1}$. This means that to reach the same precision of our approach a standard approximation method would need $\gamma\Delta t \sim 10^{-8}$. Even for this simple example, Δt has to be reduced by four orders of magnitude and consequently the depth of the resulting circuit is greatly reduced, as $N_{step}^{(SA)} \sim 10^5$ against $N_{step}^{(QN)} \sim 10^1$.

In Fig. 7.1 (b) we focus on the same toy model with fixed $\Delta t = 10^{-6}$ and we simulate Alg. 4 for different number of realizations $\mathcal{N}_r$. The solid blue line is the trace distance $\mathcal{T}_{sampled}^{(QN)} = \mathcal{T}(\hat{\chi}(T), \hat{\rho}_{sampled}^{(QN)}(T))$ as a function of $\mathcal{N}_r$. Each point is the mean over 100 independent simulations and vertical bars are the standard deviations of the means. The orange dashed line is the sampling error η in Eq. (7.29). The behaviour of $\mathcal{T}_{sampled}^{(QN)}$ follows with good agreement the behaviour of η. By taking larger $\mathcal{N}_r$ one can reach the same precision of the corresponding point in Fig. 7.1 (a), which is the rightmost point of the solid blue curve (for that point $\Delta t = 10^{-6}$). This requires a huge number of samples, but it is a consequence of the simple toy model here considered for which the approximation error is very small. For systems with higher n, since the approximation error scales as $\sim n^{2m}$, a limited number of realizations $\mathcal{N}_r$ is required to reach the accuracy set by the approximation error.

7.3 Discussion

We have presented an algorithm based on the unitary unraveling of the Lindblad equation tailored for the efficient simulation of open quantum systems on quantum devices. The system evolution is driven with the addition of a single ancillary qubit, independently of the system size. This substantially reduces the total number of circuit qubits. The reproduced perturbative solution of the Lindblad equation, for small

environment coupling constants, permits a larger time step Δt while maintaining the desired accuracy, thereby reducing the total number of steps, i.e. the depth of the circuit. The algorithm does not break down in the strong coupling regime. In this case the approximation converges to the first order solution in Δt, thus maintaining the same performances of other proposals but keeping the advantage of using a single bath qubit.

The algorithm can be tested on real quantum computers paired with error mitigation to reduce the impact of the inherent noise of the devices. The possibility of introducing non-Markovian effects can be explored by relaxing the prescription of resetting the bath qubit after each time step.

Chapter 8

Fundamental decoherence of a transmon qubit

The aim of this chapter is to quantify the limit set by collapse models on the performance of a superconducting transmon qubit, one of the most advanced and promising building block for a quantum processing unit. The CSL model (more generally, collapse models [13]) is an alternative formulation of quantum mechanics developed in order to solve the tension between the quantum superposition principle and the wave packet reduction postulate. At the core of the model there is a classical noise, suitably coupled to the wave function of particles accounting for its collapse, which now becomes part of the dynamics, not a separate postulate. The CSL state vector reduction of quantum states becomes more effective as the difference in mass density of the states in superposition increases [99]. In this way the model is consistent with quantum mechanics in the microscopic regime, where the standard theory gives extremely accurate predictions, at the same time justifying why macroscopic objects are always localized in space.

We start by reviewing the key elements of the Bardeen-Cooper-Schrieffer (BCS) theory of superconductors needed for the subsequent analysis, highlighting the role played by the excited states of a superconductor, the quasiparticles. Then we discuss how to treat CSL noise in the BCS formalism, outlining the key elements needed to compute CSL effects on transmon qubits. We compute the reduction rate of CSL, i.e. the rate at which CSL localizes a superposition of the computational basis states of transmon qubits. We estimate that this effect is at date negligibly small to be detected. We then characterize the effects of the CSL dissipation on transmon devices. We show how the CSL noise perturbs the superconducting materials in transmon qubits, by generating additional quasiparticles. These excited states accumulate over time in the devices' volume leading to a non equilibrium steady state quasiparticle density larger than the thermal one. Notably, it is a well known fact that the re-

laxation rate of transmon qubits depends linearly on the quasiparticle density, and that the latter has unexplained high values at operating temperatures of transmon qubits. Many physical processes contribute to such excess of quasiparticles, which already makes an experimental test to detect CSL very challenging. Still, the established dependence of the relaxation rate on the quasiparticle density allows for a direct comparison with experimental data. In particular, we exclude CSL to be the leading contribution to quasiparticle generation.

8.1 Theoretical background

8.1.1 BCS theory

This section recaps the key concepts and quantities of the microscopic theory of conventional superconductors, the BCS theory. Some metals display distinctive physical features below a critical temperature T_c: it is energetically favoured for electrons to attract and to bind in pairs, called Cooper pairs. The attraction is mediated by phonons, and the two electrons in a Cooper pair have opposite momenta and spins. Since the total spin of a Cooper pair is zero, different pairs behave coherently similarly to (but not exactly as) boson condensates.

The BCS Hamiltonian of the system of electrons is given by [100, 101]

$$\hat{H}_{BCS} = \sum_{\mathbf{k}\sigma} \xi_{\mathbf{k}} \hat{c}^{\dagger}_{\mathbf{k}\sigma} \hat{c}_{\mathbf{k}\sigma} + \sum_{\mathbf{k}\mathbf{k}'} U_{\mathbf{k}\mathbf{k}'} \hat{c}^{\dagger}_{\mathbf{k}\uparrow} \hat{c}^{\dagger}_{-\mathbf{k}\downarrow} \hat{c}_{-\mathbf{k}'\downarrow} \hat{c}_{\mathbf{k}'\uparrow} \,, \tag{8.1}$$

where $\xi_{\mathbf{k}} = \hbar^2 k^2/2m - \epsilon_F$ is the energy measured with respect to the Fermi energy ϵ_F, and $U_{\mathbf{k}\mathbf{k}'}$ are the matrix elements of the interaction potential. The first term in Eq. (8.1) is the kinetic energy while the second term is the potential energy, coupling Cooper pairs of different momenta k and k'.

The BCS Hamiltonian contains terms with four fermionic operators that are difficult to work with. Its expression is simplified through the mean field procedure. One defines

$$a_{\mathbf{k}} = \langle \hat{c}^{\dagger}_{\mathbf{k}\uparrow} \hat{c}^{\dagger}_{-\mathbf{k}\downarrow} \rangle \,, \tag{8.2}$$

and assumes that the fluctuations $(\hat{c}^{\dagger}_{\mathbf{k}\uparrow} \hat{c}^{\dagger}_{-\mathbf{k}\downarrow} - a_{\mathbf{k}})$ are negligible. Then by substituting

$$\hat{c}^{\dagger}_{\mathbf{k}\uparrow} \hat{c}^{\dagger}_{-\mathbf{k}\downarrow} = a_{\mathbf{k}} + \left(\hat{c}^{\dagger}_{\mathbf{k}\uparrow} \hat{c}^{\dagger}_{-\mathbf{k}\downarrow} - a_{\mathbf{k}} \right) , \tag{8.3}$$

(and its conjugate) in the BCS Hamiltonian and by keeping terms up to first order in the fluctuations, one obtains the Bogoliubov Hamiltonian [102]

$$\hat{H}_B = \sum_{\mathbf{k}\sigma} \xi_{\mathbf{k}} \hat{c}^{\dagger}_{\mathbf{k}\sigma} \hat{c}_{\mathbf{k}\sigma} + \sum_{\mathbf{k}\mathbf{k}'} U_{\mathbf{k}\mathbf{k}'} [a_{\mathbf{k}'} \hat{c}^{\dagger}_{\mathbf{k}\uparrow} \hat{c}^{\dagger}_{\mathbf{k}\downarrow} + a_{\mathbf{k}} \hat{c}_{\mathbf{k}'\downarrow} \hat{c}_{\mathbf{k}'\uparrow} - a_{\mathbf{k}} a_{\mathbf{k}'}] \,. \tag{8.4}$$

By defining $\Delta_{\mathbf{k}} = \sum_{\mathbf{k}'} U_{\mathbf{k}\mathbf{k}'} a_{\mathbf{k}'}$, which are called the superconducting gap parameters, the Hamiltonian becomes

$$\hat{H}_B = \sum_{\mathbf{k}\sigma} \xi_{\mathbf{k}} \hat{c}^\dagger_{\mathbf{k}\sigma} \hat{c}_{\mathbf{k}\sigma} - \sum_{\mathbf{k}} \Delta_{\mathbf{k}} [\hat{c}^\dagger_{\mathbf{k}\uparrow} \hat{c}^\dagger_{-\mathbf{k}\downarrow} + \hat{c}_{-\mathbf{k}\downarrow} \hat{c}_{\mathbf{k}\uparrow} + a_{\mathbf{k}}] \,. \tag{8.5}$$

The ground state of a superconductor is given by the BCS ground state [102]

$$|\psi_S\rangle = \prod_{\mathbf{k}} (u_{\mathbf{k}} + e^{i\phi} v_{\mathbf{k}} \hat{c}^\dagger_{\mathbf{k}\uparrow} \hat{c}^\dagger_{-\mathbf{k}\downarrow}) \, |0\rangle \ , \tag{8.6}$$

where $|0\rangle$ is the vacuum state of the electrons, ϕ is the phase of the superconductor and the real coefficients $u_{\mathbf{k}}$ and $v_{\mathbf{k}}$ satisfy the normalization conditions $u^2_{\mathbf{k}} + v^2_{\mathbf{k}} = 1$. In particular, $v^2_{\mathbf{k}}$ ($u^2_{\mathbf{k}}$) is the probability that a Cooper pair of momentum k is occupied (unoccupied). The excited states of a superconductor are found with the Bogoliubov transformation, that diagonalizes the Hamiltonian in Eq. (8.4) by introducing new canonical fermionic operators $\hat{\gamma}_{\mathbf{k}\sigma}$

$$\begin{aligned} \hat{\gamma}_{\mathbf{k}\uparrow} &= u_{\mathbf{k}} \hat{c}_{\mathbf{k}\uparrow} - v_{\mathbf{k}} e^{i\phi} \hat{c}^\dagger_{-\mathbf{k}\downarrow} \quad \hat{\gamma}_{-\mathbf{k}\downarrow} = v_{\mathbf{k}} e^{i\phi} \hat{c}^\dagger_{\mathbf{k}\uparrow} + u_{\mathbf{k}} \hat{c}_{-\mathbf{k}\downarrow} \\ \hat{\gamma}^\dagger_{\mathbf{k}\uparrow} &= u_{\mathbf{k}} \hat{c}^\dagger_{\mathbf{k}\uparrow} - v_{\mathbf{k}} e^{-i\phi} \hat{c}_{-\mathbf{k}\downarrow} \quad \hat{\gamma}^\dagger_{-\mathbf{k}\downarrow} = v_{\mathbf{k}} e^{-i\phi} \hat{c}_{\mathbf{k}\uparrow} + u_{\mathbf{k}} \hat{c}^\dagger_{-\mathbf{k}\downarrow} \,. \end{aligned} \tag{8.7}$$

The inverse Bogoliubov transformation is given by

$$\begin{aligned} \hat{c}_{\mathbf{k}\uparrow} &= u_{\mathbf{k}} \hat{\gamma}_{\mathbf{k}\uparrow} + v_{\mathbf{k}} e^{i\phi} \hat{\gamma}^\dagger_{-\mathbf{k}\downarrow} \quad \hat{c}_{-\mathbf{k}\downarrow} = u_{\mathbf{k}} \hat{\gamma}_{-\mathbf{k}\downarrow} - v_{\mathbf{k}} e^{i\phi} \hat{\gamma}^\dagger_{\mathbf{k}\uparrow} \\ \hat{c}^\dagger_{\mathbf{k}\uparrow} &= u_{\mathbf{k}} \hat{\gamma}^\dagger_{\mathbf{k}\uparrow} + v_{\mathbf{k}} e^{-i\phi} \hat{\gamma}_{-\mathbf{k}\downarrow} \quad \hat{c}^\dagger_{-\mathbf{k}\downarrow} = u_{\mathbf{k}} \hat{\gamma}^\dagger_{-\mathbf{k}\downarrow} - v_{\mathbf{k}} e^{-i\phi} \hat{\gamma}_{\mathbf{k}\uparrow} \,. \end{aligned} \tag{8.8}$$

Substituting Eqs. (8.8) in the Bogoliubov Hamiltonian in Eq. (8.5) one finds

$$\begin{aligned} \hat{H}_B = &\sum_{\mathbf{k}} \left[\xi_{\mathbf{k}} (u^2_{\mathbf{k}} - v^2_{\mathbf{k}}) + 2\Delta_{\mathbf{k}} u_{\mathbf{k}} v_{\mathbf{k}} \right] \left[\hat{\gamma}^\dagger_{\mathbf{k}\uparrow} \hat{\gamma}_{\mathbf{k}\uparrow} + \hat{\gamma}^\dagger_{-\mathbf{k}\downarrow} \hat{\gamma}_{-\mathbf{k}\downarrow} \right] \\ &+ \sum_{\mathbf{k}} \left[2\xi_{\mathbf{k}} u_{\mathbf{k}} v_{\mathbf{k}} - \Delta_{\mathbf{k}} (u^2_{\mathbf{k}} - v^2_{\mathbf{k}}) \right] \left[\hat{\gamma}^\dagger_{\mathbf{k}\uparrow} \hat{\gamma}^\dagger_{-\mathbf{k}\downarrow} + \hat{\gamma}_{-\mathbf{k}\downarrow} \hat{\gamma}_{\mathbf{k}\uparrow} \right] \\ &+ \sum_{\mathbf{k}} \left[2\xi_{\mathbf{k}} v^2_{\mathbf{k}} - 2\Delta_{\mathbf{k}} u_{\mathbf{k}} v_{\mathbf{k}} + \Delta_{\mathbf{k}} a_{\mathbf{k}} \right] . \end{aligned} \tag{8.9}$$

This expression contains undesired terms of the type $\hat{\gamma}\hat{\gamma}$ and $\hat{\gamma}^\dagger\hat{\gamma}^\dagger$ so their coefficients are set to zero [101, 102]

$$2\xi_{\mathbf{k}} u_{\mathbf{k}} v_{\mathbf{k}} - \Delta_{\mathbf{k}} (u^2_{\mathbf{k}} - v^2_{\mathbf{k}}) = 0 \,. \tag{8.10}$$

This condition together with the normalization condition $u^2_{\mathbf{k}} + v^2_{\mathbf{k}} = 1$ gives

$$u^2_{\mathbf{k}} = \frac{1}{2}\left(1 + \frac{\xi_{\mathbf{k}}}{E_{\mathbf{k}}}\right) \qquad\qquad v^2_{\mathbf{k}} = \frac{1}{2}\left(1 - \frac{\xi_{\mathbf{k}}}{E_{\mathbf{k}}}\right) \tag{8.11}$$

where $E_{\mathbf{k}}$ are given by

$$E_{\mathbf{k}} = \xi_{\mathbf{k}}(u_{\mathbf{k}}^2 - v_{\mathbf{k}}^2) + 2\Delta_{\mathbf{k}} u_{\mathbf{k}} v_{\mathbf{k}} = \sqrt{\xi_{\mathbf{k}}^2 + \Delta_{\mathbf{k}}^2}\,. \tag{8.12}$$

One can see that, as k varies from values well below the Fermi surface to values well above it, $v_{\mathbf{k}}^2$ goes from one to zero (and analogously $u_{\mathbf{k}}^2$ goes from zero to one), i.e. Cooper pairs of momentum k well below the Fermi surface are occupied in the ground state with probability one. As the momentum of the Cooper pairs increases above the Fermi surface, the occupation probability decreases to 0.

The Bogoliubov Hamiltionian in diagonal form is

$$\hat{H}_B = \sum_{\mathbf{k}} E_{\mathbf{k}} \left[\hat{\gamma}_{\mathbf{k}\uparrow}^\dagger \hat{\gamma}_{\mathbf{k}\uparrow} + \hat{\gamma}_{-\mathbf{k}\downarrow}^\dagger \hat{\gamma}_{-\mathbf{k}\downarrow}\right] + W_S\,, \tag{8.13}$$

with $E_{\mathbf{k}} = \sqrt{\xi_{\mathbf{k}}^2 + \Delta_{\mathbf{k}}^2}$ the energy associated to excitations, and $W_S = \sum_{\mathbf{k}} \left[2\xi_{\mathbf{k}} v_{\mathbf{k}}^2 - 2\Delta_{\mathbf{k}} u_{\mathbf{k}} v_{\mathbf{k}} + \Delta_{\mathbf{k}} a_{\mathbf{k}}\right]$ an energy shift.

The BCS ground state is the vacuum state of the operators $\hat{\gamma}_{\mathbf{k}\sigma}$, i.e. $\hat{\gamma}_{\mathbf{k}\sigma} |\Psi_S\rangle = 0$. Acting with $\hat{\gamma}_{\mathbf{k}\sigma}^\dagger$ on the BCS ground state gives an excited state, called quasiparticle. The excited states in terms of $\hat{c}_{\mathbf{k}\sigma}^\dagger$ read

$$|\psi_1\rangle = \hat{\gamma}_{\mathbf{k}\uparrow}^\dagger |\psi_S\rangle = \hat{c}_{\mathbf{k}\uparrow}^\dagger \prod_{\mathbf{l}\neq\mathbf{k}} (u_{\mathbf{l}} + v_{\mathbf{l}} \hat{c}_{\mathbf{l}\uparrow}^\dagger \hat{c}_{-\mathbf{l}\downarrow}^\dagger) |0\rangle \tag{8.14}$$

$$|\psi_2\rangle = \hat{\gamma}_{-\mathbf{k}\downarrow}^\dagger |\psi_S\rangle = \hat{c}_{-\mathbf{k}\downarrow}^\dagger \prod_{\mathbf{l}\neq\mathbf{k}} (u_{\mathbf{l}} + v_{\mathbf{l}} c_{\mathbf{l}\uparrow}^\dagger c_{-\mathbf{l}\downarrow}^\dagger) |0\rangle\ , \tag{8.15}$$

meaning that for given momentum k there is an electron with probability one and the other state of the pair is empty. Quasiparticles are then interpreted as fermions created by $\hat{\gamma}_{\mathbf{k}\sigma}^\dagger$ in one-to-one correspondence with the $\hat{c}_{\mathbf{k}\sigma}^\dagger$.

At a temperature of absolute zero a superconductor sits in its ground state without any excitations. For a non vanishing temperature T, some quasiparticle will be thermally excited, and they will be distributed according to some occupation function $f(E,T)$, E being the energy of quasiparticles. For a superconductor at thermal equilibrium it is generally assumed that the occupation function is a Fermi-Dirac distribution

$$f_{FD}(E,T) = \frac{1}{e^{E/k_B T} + 1}\,. \tag{8.16}$$

The normalized quasiparticle density x_{qp}, i.e. the ratio between the number of quasiparticles and the number of Cooper pairs, quantifies the number of excitations in a superconducting device. Its expression is given by

$$x_{qp} = \int_\Delta^\infty f(E)\rho(E)dE\,, \tag{8.17}$$

where $\rho(E)$ is the normalized superconducting density of states

$$\rho(E) = \frac{E}{\sqrt{E^2 - \Delta^2}}\,. \tag{8.18}$$

Notably, the superconducting density of states in Eq. (8.18) contains a single gap parameter Δ which is independent of k. Indeed, in general the superconducting gap parameters should be different for different values of k

$$\begin{aligned}\Delta_{\mathbf{k}} &= \sum_{\mathbf{k}'} U_{\mathbf{k}\mathbf{k}'} a_{\mathbf{k}'} = \sum_{\mathbf{k}'} U_{\mathbf{k}\mathbf{k}'} \langle \hat{c}^\dagger_{\mathbf{k}'\uparrow} \hat{c}^\dagger_{-\mathbf{k}'\downarrow} \rangle \\ &= \sum_{\mathbf{k}'} U_{\mathbf{k}\mathbf{k}'} u_{\mathbf{k}'} v_{\mathbf{k}'} \langle 1 - \hat{\gamma}^\dagger_{\mathbf{k}'\uparrow} \hat{\gamma}_{\mathbf{k}'\uparrow} - \hat{\gamma}^\dagger_{-\mathbf{k}'\downarrow} \hat{\gamma}_{-\mathbf{k}'\downarrow} \rangle \\ &= \sum_{\mathbf{k}'} U_{\mathbf{k}\mathbf{k}'} u_{\mathbf{k}'} v_{\mathbf{k}'} (1 - f(E_{\mathbf{k}'}))\,.\end{aligned} \tag{8.19}$$

By substituting the expression of $u_{\mathbf{k}}$ and $v_{\mathbf{k}}$ in Eq. (8.11) one finds the self consistent equations

$$\Delta_{\mathbf{k}} = -\frac{1}{2} \sum_{\mathbf{k}'} U_{\mathbf{k}\mathbf{k}'} \frac{\Delta_{\mathbf{k}'}}{E_{\mathbf{k}'}} (1 - f(E_{\mathbf{k}'}))\,. \tag{8.20}$$

The BCS assumption is that $U_{\mathbf{k}\mathbf{k}'} = -V$ is a negative constant (leading to an attractive interaction) for all k such that $|\xi_{\mathbf{k}}| < \hbar\omega_D$, and $U_{\mathbf{k}\mathbf{k}'} = 0$ otherwise. In this way one has

$$\Delta_{\mathbf{k}} = \begin{cases} \Delta \text{ for } |\xi_{\mathbf{k}}| < \hbar\omega_D \\ 0 \text{ for } |\xi_{\mathbf{k}}| > \hbar\omega_D\,, \end{cases} \tag{8.21}$$

where Δ is the superconducting gap. Its meaning has a direct interpretation when looking at the quasiparticle energies $E_{\mathbf{k}}$ as function of $\xi_{\mathbf{k}}$ in Eq. (8.12). They have a minimum at $\xi_{\mathbf{k}} = 0$ and the value of the excitation energy at this point is Δ, the minimum energy amount needed to generate an excited state.

Δ is a function of temperature T, but at sufficiently low temperatures (we will make this assumption hereafter) its value is $\Delta(T) \approx \Delta(0) = 1.76 k_B T_c$, where T_c is the critical temperature and k_B is the Boltzmann constant. This assumption is well justified for small enough temperatures T. Indeed the self consistent equation for the gap (see Eq. (8.20)) becomes

$$\Delta = \frac{V}{2} \sum_{\mathbf{k}'} \frac{\Delta}{E_{\mathbf{k}'}} (1 - 2 f(E_{\mathbf{k}'}))\,, \tag{8.22}$$

simplifying the common Δ factor we are left with

$$\begin{aligned} 1 &= \frac{V}{2}\sum_{\mathbf{k}'}\frac{1}{E_{\mathbf{k}'}}(1-2f(E_{\mathbf{k}'})) \\ 1 &= g(\epsilon_F)V\left(\int_{\Delta}^{\hbar\omega_D}\frac{dE}{\sqrt{E^2-\Delta^2}} - \int_{\Delta}^{\hbar\omega_D} dE\rho(E)\frac{1}{E}2f(E)\right) \\ 1 &\approx g(\epsilon_F)V\left(\ln\frac{2\hbar\omega_D}{\Delta} - x_{qp}\right), \end{aligned} \tag{8.23}$$

where in the third line we switched to an integration over the quasiparticle energies E and $g(\epsilon_F)$ is the density of states for electrons of one spin orientation calculated at the Fermi energy. Eq. (8.23) can be solved for the gap

$$\Delta = 2\hbar\omega_D e^{-1/g(\epsilon_F)V - x_{qp}} = \Delta(0)e^{-x_{qp}} \approx \Delta(0)(1-x_{qp}) \tag{8.24}$$

where $\Delta(0) = 2\hbar\omega_D e^{-1/g(\epsilon_F)} = 1.76k_BT_c$ is the superconducting gap without quasiparticles, so at absolute zero. The gap depends on the normalized quasiparticle density and therefore on the occupation function of quasiparticles. However for small occupation function, i.e. for small enough temperatures, it is reasonable to approximate $\Delta = \Delta(0)$.

Making the assumptions that $f(E)$ is a Fermi-Dirac distribution and that x_{qp} is small, so that most of the excited states are close to the gap, one can find the following expression for x_{qp} [103]

$$x_{qp} = \sqrt{2\pi k_B T/\Delta}e^{-\Delta/k_BT}\,. \tag{8.25}$$

Inserting in this equation a realistic experimental value for transmon qubits of $T = 20mK$ and the parameters of aluminum (a typical superconductor used in transmon qubits), the quasiparticle density should be exponentially suppressed: $x_{qp} \sim 10^{-52}$ [104]. Notably, experiments on superconducting qubits and superconducting resonators show significanlty higher density values, $x_{qp}^{exp} \sim 10^{-9} - 10^{-6}$ [105]. Thermal equilibrium is not able to explain such an excess of quasiparticles, that are termed non-equilibrium quasiparticles.

8.1.2 CSL model in the BCS framework

The CSL model is an alternative formulation of quantum mechanics devised to solve the problem of the quantum-to-classical transition in quantum theory. CSL provides a unified description for the Schrödinger evolution, which is linear and deterministic, and the non-linear and stochastic dynamics giving wave packet reduction. This is done by modifying the Schrödinger equation, adding stochastic and non-linear

terms that implement the collapse of the wave function. The modification is consistent with quantum mechanics in the microscopic regime, where the standard theory gives extremely accurate predictions, at the same time justifying why macroscopic objects are always localized in space. The strength and spatial extension of the collapse (which is white in time) are dictated respectively by two parameters of the theory, λ and r_c. Theoretical arguments suggest that $r_c \sim 10^{-7}$ m [13, 106] and λ in the range $\sim 10^{-8} - 10^{-16}\mathrm{s}^{-1}$ [13, 107]. From now on, to fix a possible value we set $\lambda = 10^{-10}\mathrm{s}^{-1}$.

The CSL model is usually formulated in position space. The collapse of the wave function is described by a non-linear and stochastic interaction with a classical noise through the Itô equation

$$\begin{aligned} d\,|\psi\rangle = \Bigg[& -\frac{i}{\hbar}\hat{H}dt + \frac{\sqrt{\lambda}}{m_0}\int d^3x \big(\hat{M}(\mathbf{x}) - \langle \hat{M}(\mathbf{x})\rangle\big) dW_t(\mathbf{x}) \\ & - \frac{\lambda}{2m_0^2}\int d^3x\, d^3y \big(\hat{M}(\mathbf{x}) - \langle \hat{M}(\mathbf{x})\rangle\big) G(\mathbf{x}-\mathbf{y}) \times \\ & \big(\hat{M}(\mathbf{y}) - \langle \hat{M}(\mathbf{y})\rangle\big) dt \Bigg] |\psi\rangle \end{aligned} \tag{8.26}$$

where m_0 is the nucleon mass, $\langle\,\cdot\,\rangle$ denotes the expectation value on the state $|\psi\rangle$ and $\hat{M}(\mathbf{x})$ is the mass density operator defined by

$$\hat{M}(\mathbf{x}) = \sum_j m_j \hat{a}_j^\dagger(\mathbf{x})\hat{a}_j(\mathbf{x})\,. \tag{8.27}$$

The operators $\hat{a}_j^\dagger(\mathbf{x})$ and $\hat{a}_j(\mathbf{x})$ are the creation and annihilation operators at position $\mathbf{x}$ of a particle of type j with mass m_j. In our case we will have a single m given by the mass of electrons. The $G(\mathbf{x}-\mathbf{y})$ in (8.26) are Gaussian functions of the form

$$G(\mathbf{x}-\mathbf{y}) = \frac{1}{(4\pi r_c^2)^{3/2}} e^{-\frac{1}{4r_c^2}(x-y)^2}\,, \tag{8.28}$$

that characterize the statistical properties of the noise $W_t(\mathbf{x})$. Indeed, by calling $\xi_t(\mathbf{x}) = dW_t(\mathbf{x})/dt$, one has that $\mathbb{E}[\xi_t(\mathbf{x})] = 0$, and the two point correlator $\mathbb{E}[\xi_t(\mathbf{x}), \xi_s(\mathbf{y})] = G(\mathbf{x}-\mathbf{y})\delta(t-s)$ where $\mathbb{E}[\cdot]$ denotes the stochastic average. These properties together with the mass proportionality of $\hat{M}$ guarantee respectively localization in space and the amplification mechanism: the collapse rate of a body of N constituents gets amplified linearly in N. It is generally difficult to work directly with Eq. (8.26), mainly because of its non-linearity. Since we are interested in expectation values we can use the simplified linear, but still stochastic, dynamic given by

$$i\hbar\frac{d\,|\psi(t)\rangle}{dt} = (\hat{H} + \hat{H}_{\mathrm{CSL}})\,|\psi(t)\rangle\,, \tag{8.29}$$

where $\hat{H}$ is the Hamiltonian of the system ($\hat{H}_B$ in Eq. (8.13) in the present case) and $\hat{H}_{\rm CSL}$ is the CSL contribution

$$\hat{H}_{\rm CSL} = -\frac{\hbar\sqrt{\lambda}}{m_0}\int d^3x\, \xi_t(\mathbf{x})\hat{M}(\mathbf{x})\,. \tag{8.30}$$

This Hamiltonian, expressed in position space and in the Stratonovich form, is related to the second term in equation (8.26). Eq. (8.29) is linear because it does not contain $\langle\hat{M}(\mathbf{x})\rangle$. These simplifications are possible because of the equivalence of Eqs. (8.26) and (8.30) at the statistical level: non-linear effects are washed away when expectation values are computed. We mention that expressing Eq. (8.30) in its Itô form one gets an equation of the form as in Eq. (3.22).

In order to compute expectation values for superconductors we switch from position to momentum variables. The term in Eq. (8.30) is Fourier transformed in a normalization volume V (to avoid any divergences) and the position representation of the field operators is related to the momentum operators via

$$\hat{a}(\mathbf{x},s) = \frac{1}{\sqrt{V}}\sum_{\mathbf{k}} e^{i\mathbf{k}\mathbf{x}}\hat{c}_{\mathbf{k}s} \tag{8.31}$$

$$\hat{a}^\dagger(\mathbf{x},s) = \frac{1}{\sqrt{V}}\sum_{\mathbf{k}} e^{-i\mathbf{k}\mathbf{x}}\hat{c}^\dagger_{\mathbf{k}s}\,. \tag{8.32}$$

By performing such Fourier transform to momentum space, $\hat{H}_{\rm CSL}$ takes the following expression

$$\hat{H}_{\rm CSL} = -\frac{m\hbar\sqrt{\lambda}}{m_0 V}\sum_{\mathbf{k_1}\mathbf{k_2},s}\widetilde{W}_{\mathbf{k_1}-\mathbf{k_2}}(t)\,\widetilde{G}_{\mathbf{k_1}-\mathbf{k_2}}\,\hat{c}^\dagger_{\mathbf{k}_1 s}\hat{c}_{\mathbf{k}_2 s}\,. \tag{8.33}$$

The stochastic processes $\widetilde{W}_{\mathbf{k}}(t)$ have expectation values and two-point correlators given by

$$\mathbb{E}[\widetilde{W}_{\mathbf{k_1}}(t)] = 0 \tag{8.34}$$

$$\mathbb{E}[\widetilde{W}_{\mathbf{k_1}}(t)\widetilde{W}_{\mathbf{k_2}}(s)] = V\delta_{(\mathbf{k_1}+\mathbf{k_2})}\delta(t-s)\,, \tag{8.35}$$

and they are weighted by the Gaussian function

$$\widetilde{G}_{\mathbf{k}} = (4\pi r_c^2)^{3/4}e^{-\frac{r_c^2k^2}{2}}\,. \tag{8.36}$$

Eq. (8.33) shows that the CSL noise scatters electrons, effectively acting as a kick which injects energy to the system. We want to quantify the main effect of those

kicks on the BCS ground state of a superconductor, which amounts to the breaking of Cooper pairs into quasiparticles. To do so, we use perturbation theory: the diagonal Bogoliubov Hamiltonian $\hat{H}_B$ is the free term and the CSL Hamiltonian (8.33) is a perturbation.

The transition probability from an initial state $|i\rangle$ to a final state $|f\rangle$ is given by

$$P_{fi} = \mathbb{E}[|T_{fi}|^2] = \mathbb{E}[|\langle f|\,\hat{U}_I(t,t_i)\,|i\rangle\,|^2]\,, \tag{8.37}$$

where T_{fi} is the transition amplitude from $|i\rangle$ to a state $|f\rangle$ and $\hat{U}_I(t,t_i)$ is the time evolution operator in the interaction picture

$$\hat{U}_I(t,t_i) = e^{\frac{i}{\hbar}\hat{H}_B t}\hat{U}(t,t_i)e^{-\frac{i}{\hbar}\hat{H}_B t}\,. \tag{8.38}$$

The operator $\hat{U}_I(t,t_i)$ is expanded the Dyson series, which at first order reads

$$\hat{U}(t,t_i) = \mathbb{1} + \int_{t_i}^{t} ds\,\hat{H}^{(I)}_{\rm CSL}(s)\,. \tag{8.39}$$

where $\hat{H}^{(I)}_{\rm CSL}(t) = e^{\frac{i}{\hbar}\hat{H}_B t}\hat{H}_{\rm CSL}e^{-\frac{i}{\hbar}\hat{H}_B t}$ is the Hamiltonian in Eq. (8.33) in the interaction picture. The second order term of the Dyson series is not shown because to order λ it gives zero contribution in the transition probability Eq. (8.51).

Using the inverse Bogoliubov transformation [see Eq. (8.8)], we can transform the CSL Hamiltonian in terms of the operators $\hat{\gamma}_{\mathbf{k}s}$ and then find its expression in the interaction picture, that reads

$$\begin{aligned}
\hat{H}^{(I)}_{\rm CSL} = &-\frac{\hbar\sqrt{\lambda}m}{m_0 V}\sum_{\mathbf{k_1}\mathbf{k_2}}\widetilde{G}_{\mathbf{k_1}-\mathbf{k_2}}\times \\
&\Big[\widetilde{W}_{\mathbf{k_1}-\mathbf{k_2}}(t)L(k_1,k_2)e^{\frac{i}{\hbar}(E_{\mathbf{k}_1}-E_{\mathbf{k}_2})t}\hat{\gamma}^\dagger_{\mathbf{k}_1\uparrow}\hat{\gamma}_{\mathbf{k}_2\uparrow} \\
&+\widetilde{W}_{\mathbf{k_2}-\mathbf{k_1}}(t)L(k_1,k_2)e^{\frac{i}{\hbar}(E_{\mathbf{k}_2}-E_{\mathbf{k}_1})t}\hat{\gamma}^\dagger_{-\mathbf{k}_2\downarrow}\hat{\gamma}_{-\mathbf{k}_1\downarrow} \\
&+\widetilde{W}_{\mathbf{k_2}-\mathbf{k_1}}(t)M(k_1,k_2)e^{-i\phi}e^{-\frac{i}{\hbar}(E_{\mathbf{k}_1}+E_{\mathbf{k}_2})t}\hat{\gamma}_{\mathbf{k}_2\uparrow}\hat{\gamma}_{-\mathbf{k}_1\downarrow} \\
&+\widetilde{W}_{\mathbf{k_1}-\mathbf{k_2}}(t)M(k_1,k_2)e^{i\phi}e^{\frac{i}{\hbar}(E_{\mathbf{k}_1}+E_{\mathbf{k}_2})t}\hat{\gamma}^\dagger_{\mathbf{k}_1\uparrow}\hat{\gamma}^\dagger_{-\mathbf{k}_2\downarrow}\Big]\,.
\end{aligned} \tag{8.40}$$

The first two terms in the square brackets are associated to quasiparticle scattering: a quasiparticle of momentum k_1 is annihilated and another one of momentum k_2 is created. The third term is associated to quasiparticle recombination: two quasiparticles of different momenta are annihilated. The fourth term is the inverse process,

i.e. quasiparticle generation: two quasiparticle of different momenta are created. The functions M and L, usually called coherence factors, are given by

$$L(k_1, k_2) = (u_{\mathbf{k}_1} u_{\mathbf{k}_2} - v_{\mathbf{k}_1} v_{\mathbf{k}_2}) \tag{8.41}$$

$$M(k_1, k_2) = (u_{\mathbf{k}_1} v_{\mathbf{k}_2} + v_{\mathbf{k}_1} u_{\mathbf{k}_2}) \,. \tag{8.42}$$

Substituting Eqs. (8.11) we have that:

$$L^2(E_1, E_2) = \frac{1}{2}\left(1 - \frac{\Delta^2 - \xi_1 \xi_2}{E_1 E_2}\right) \tag{8.43}$$

$$M^2(E_1, E_2) = \frac{1}{2}\left(1 + \frac{\Delta^2 - \xi_1 \xi_2}{E_1 E_2}\right), \tag{8.44}$$

where according to Eq. (8.12), $\xi_{\mathbf{k}} = \sqrt{E_{\mathbf{k}}^2 - \Delta_{\mathbf{k}}^2}$.

8.2 Effects of CSL on transmon qubits

In this section we evaluate the two main effects of CSL on transmon qubits: the reduction rate of a superposition of the computational basis and the steady state quasiparticle density due to CSL dissipation.

8.2.1 CSL reduction rate

As anticipated, the direct effect of CSL on superconducting qubits is to destroy their superposition states. We estimate the CSL reduction rate of the computational basis states, labeled by $|0\rangle$ and $|1\rangle$, of a transmon qubit. To estimate the reduction rate, we use a qualitative microscopic description of $|0\rangle$ and $|1\rangle$, keeping in mind that the CSL collapse mechanism is sensitive only to superposition in space of different masses.

A transmon qubit is an electrical circuit consisting of a superconducting island (usually made of aluminum) of volume $V \sim 10^2 \mu\text{m}^3$ linked to a superconducting reservoir (of approximately the same size) through an insulating barrier of width $d \sim 1 - 10^2$ nm [108], forming a Josephson junction. By applying a gate voltage, Cooper pairs can tunnel through the Josephson junction from the reservoir into the island and viceversa. The size of the transmon circuit allows to treat the number of excess Cooper pairs in the island as a quantum number, and the tunneling of a single Cooper pair can be controlled by manipulating the gate voltage.

The states $|0\rangle$ and $|1\rangle$ are characterized by the number of excess Cooper pairs that have tunneled from the reservoir into the island. In fact, for transmon qubits $|0\rangle$ and $|1\rangle$ are not exactly eigenstates of the number of extra Cooper pairs operator,

but rather both $|0\rangle$ and $|1\rangle$ are superposition of states with different number of extra Cooper pairs on the island. Nevertheless, for our estimation we can assume that, for a typical device, the difference in the number of pairs of the two computational basis states is of the order of 4 [109]. We can then effectively identify $|0\rangle$ as the state with four Cooper pairs on one side of the Josephson junction, the reservoir, and $|1\rangle$ as the state with four Cooper pairs on the other side of the junction, the island. We can think of these four Cooper pairs as two groups of four electrons. The two groups are separated by the BCS coherence length ξ_c (a measure of the average distance between the two electrons in a Cooper pair) which for aluminum, the superconducting material used for transmon circuits, is $\sim 10^{-6}$ m [101]. The reduction rate is computed with the formula [107]

$$\Gamma_R = \lambda n^2 N \left(\frac{m_e}{m_0}\right)^2 \tag{8.45}$$

for n particles within a radius smaller than the correlation length r_c, N groups of particles separated by more than the correlation length r_c, and with m_e the mass of electrons. In our effective model, if we substitute $n = 4$ and $N = 2$ into Eq.(8.45), meaning that we are considering a configuration with four electrons packed within a distance smaller than r_c in each of the $N = 2$ groups of electrons separated by a distance $\xi_c > r_c$, the reduction rate is $\Gamma = 32\lambda(m_e/m_0)^2 \approx 10^{-16}\text{s}^{-1}$. We chose the value for n that gives the highest value for Γ_R, to estimate the strongest theoretical CSL effect. Nevertheless, the CSL reduction rate is negligibly weak, as the lifetime of a single qubit would be of the orders of billions of years. Even a large quantum computer composed by millions or even billions of such qubits, would be safe against the localization of superposition dictated by collapse models.

8.2.2 CSL steady state quasiparticle density

CSL is ineffective in directly suppressing superposition states of superconducting qubits, mainly because too few electrons are involved in the superposition, which moreover have a very small mass. However, CSL impacts decoherence of superconducting qubits also indirectly. As discussed in section 8.1.2, the CSL noise couples to the Cooper pairs inside a superconductor, generating its excited states, the quasiparticles. Notably, quasiparticles contribute to the relaxation rate of transmon qubits, and such contribution is proportional to their density [103]. In this section we quantify the steady state quasiparticle density due to CSL, to infer a limit on the coherence time of transmon qubits.

We start by computing the transition probability in Eq. (8.37) with $|i\rangle = |\psi_S\rangle$, by using the time evolution operator expanded to first order as in Eq. (8.39), where the perturbation is the CSL Hamiltonian in Eq. (8.40). By recalling that $|\psi_S\rangle$ is

the vacuum state for the operators $\hat{\gamma}_{\mathbf{k}s}$, only the fourth term of the Hamiltonian in Eq. (8.40) gives a non vanishing contribution when acting on $|\psi_S\rangle$. This produces a transition to a final state different from $|\psi_S\rangle$, which contains quasiparticles. Thus, the main effect of the CSL noise on a superconductor initially in its ground state, to first order in perturbation theory, is the generation of quasiparticles. In particular, the only final states which give non zero contribution to the expectation value in Eq. (8.37) are those of the form

$$|f\rangle = \hat{\gamma}^\dagger_{\mathbf{q}\uparrow}\hat{\gamma}^\dagger_{-\mathbf{p}\downarrow}\,|\psi_S\rangle\ , \tag{8.46}$$

where q and p are fixed. Choosing $|f\rangle$ as in Eq. (8.46), the zero order term of the Dyson series is zero when inserted into Eq. (8.37). The first order contribution of the Dyson series is

$$T^{(1)}_{qp} = -\frac{i}{\hbar}\int_{t_i}^{t} dt_1\,\langle\psi_S|\,\hat{\gamma}_{-\mathbf{p}\downarrow}\hat{\gamma}_{\mathbf{q}\uparrow}\hat{H}^{(I)}_{\rm CSL}(t_1)\,|\psi_S\rangle\ , \tag{8.47}$$

and by substituting Eq. (8.40) for the interacting Hamiltonian we find

$$\begin{aligned} T^{(1)}_{qp} =& \frac{i\sqrt{\lambda}m}{m_0 V}\int_{t_i}^{t} dt_1 \sum_{\mathbf{k_1}\mathbf{k_2}} \widetilde{G}_{\mathbf{k_1}-\mathbf{k_2}}\widetilde{W}_{\mathbf{k_1}-\mathbf{k_2}}(t_1)M(k_1,k_2)\times \\ & e^{i\phi}e^{\frac{i}{\hbar}(E_{\mathbf{k}_1}+E_{\mathbf{k}_2})t_1}\,\langle\psi_S|\,\hat{\gamma}_{-p\downarrow}\hat{\gamma}_{q\uparrow}\hat{\gamma}^\dagger_{\mathbf{k}1\uparrow}\hat{\gamma}^\dagger_{-\mathbf{k}2\downarrow}\,|\psi_S\rangle\ . \end{aligned} \tag{8.48}$$

The expectation value in the last line is simplified using the anticommutation rules

$$\langle\psi_S|\,\hat{\gamma}_{-p\downarrow}\hat{\gamma}_{q\uparrow}\hat{\gamma}^\dagger_{\mathbf{k}_1\uparrow}\hat{\gamma}^\dagger_{-\mathbf{k}_2\downarrow}\,|\psi_S\rangle = \delta_{\mathbf{k_1},\mathbf{q}}\delta_{\mathbf{k_2},\mathbf{p}}\,, \tag{8.49}$$

leading to

$$T^{(1)}_{qp} = \frac{i\sqrt{\gamma}m}{m_0 V}\int_{t_i}^{t} dt_1\,\widetilde{G}_{\mathbf{q}-\mathbf{p}}\widetilde{W}_{\mathbf{q}-\mathbf{p}}(t_1)M(q,p)e^{i\phi}e^{\frac{i}{\hbar}(E_q+E_p)t_1}\,. \tag{8.50}$$

This is the transition amplitude to a specific final state with fixed momenta p and q. The transition probability from the BCS ground state to a state as in Eq. (8.46) is computed by using Eq. (8.37). In doing so, one has to compute the two-point correlator between the noise and its complex conjugate. Using the fact that $\widetilde{W}^*_{\mathbf{k}}(t) = \widetilde{W}_{-\mathbf{k}}(t)$ and Eq. (8.35), one has that

$$P_{qp} = \frac{\lambda m^2}{m_0^2 V}\widetilde{G}^2_{\mathbf{q}-\mathbf{p}}\,M^2(q,p)\,t\,, \tag{8.51}$$

where we assumed that $t_0 = 0$ and we performed integration over t_1. This probability grows linearly with time. By dividing Eq. (8.51) by t, we obtain the transition rate for two quasiparticles with given momentum p and q to be generated by the CSL

noise. Given this rate, we can compute the steady state quasiparticle density due to CSL, ultimately assessing the fundamental limits imposed by CSL on superconducting devices. In order to do so, we have to consider how intrinsic thermal processes and the CSL generation of quasiparticles contribute to the evolution of the occupation function $f(E)$ of quasiparticles. In this regime $f(E)$ redistributes over time to a steady state different from a thermal state, that enters Eq. (8.17) to give a different steady state quasiparticle density due to CSL. Thus, we consider a superconductor starting at thermal equilibrium and we neglect all sources of environmental noise other than CSL. To account for intrinsic thermal effects, we consider the electron-phonon interaction only, since it is dominant over the electron-electron interaction. The electron-phonon interaction comprises three main physical processes: quasiparticle scattering (both by emission and absorption of a phonon), quasiparticle recombination (by the emission of a phonon) and quasiparticle generation (by the absorption of a phonon).

The kinetic equation for the quasiparticle occupation function describes how $f(E)$ redistributes over time because of the above processes. It contains the rates of the electron-phonon processes, and a generation rate given by an external source [110,111]

$$\begin{aligned}\frac{df(E)}{dt} &= \gamma_g^{\text{ext}}(E) + \frac{\gamma_0}{\Delta^3}\int_E^\infty dE' S(E,E')[(\bar{f}(E))f(E')(N(E'-E)+1) \\ &\quad - f(E)\bar{f}(E')N(E'-E)] \\ &+ \frac{\gamma_0}{\Delta^3}\int_\Delta^E dE' S(E,E')[(\bar{f}(E))f(E')N(E-E') - f(E)\bar{f}(E')(N(E-E')+1)] \\ &+ \frac{\gamma_0}{\Delta^3}\int_\Delta^\infty dE' G(E,E')[(\bar{f}(E))\bar{f}(E')N(E+E') - f(E)f(E')(N(E+E')+1)]\,,\end{aligned} \tag{8.52}$$

where $S(E,E') = (E-E')^2\rho(E')L^2(E,E')$, $G(E,E') = (E+E')^2\rho(E')M^2(E,E')$ and the rate γ_0 is a characteristic electron-phonon rate and it is a constant for a given material (for aluminum $1/\gamma_0 = \tau_0 = 438$ns [110]). The factor $N(\Omega)$ is the occupation function of phonons, which is taken to follow a Bose-Einstein distribution

$$N(\Omega) = \frac{1}{e^{\Omega/k_B T_{ph}} - 1}\,, \tag{8.53}$$

for a phonon bath at temperature T_{ph}. Phonons are assumed to be in equilibrium at the refrigerator temperature and thus $N(\Omega)$ does not change in time. The rate $\gamma_g^{\text{ext}}(E)$ is the generation rate per unit time due to external sources, for our purposes due to CSL. The second and third terms in Eq.(8.52) are associated to thermal quasiparticle scattering, and the fourth term to thermal quasiparticle recombination and generation.

We start from the transition probability in Eq.(8.51), integrating over one momentum variable p

$$\begin{aligned}\gamma_g^{\rm CSL}(E_{\mathbf{q}}) &= \frac{\lambda(4\pi r_c)^{3/2}m^2}{m_0^2(2\pi)^3}\int d^3p e^{-r_c^2(p-q)^2}M^2(p,q)\bar{f}(E_{\mathbf{p}}) \\ &= \frac{\lambda m^2(4\pi)^{3/2}r_c}{m_0^2 2(2\pi)^2}\int dp\frac{p}{q}\left(e^{-r_c^2(p-q)^2}-e^{-r_c^2(p+q)^2}\right)M^2(p,q)\bar{f}(E_{\mathbf{p}})\,,\end{aligned} \tag{8.54}$$

where in the second line we expressed the integral in polar coordinates. With the substitutions $q=\sqrt{2m}/\hbar(\sqrt{E^2-\Delta^2}+\epsilon_F)^{1/2}$ and $p=\sqrt{2m}/\hbar(\sqrt{E'^2-\Delta^2}+\epsilon_F)^{1/2}$ one obtains

$$\begin{aligned}\gamma_g^{\rm CSL}(E) = &\frac{m^2\lambda r_c}{2\sqrt{\pi}m_0^2}\frac{\sqrt{2m}}{\hbar}\frac{1}{\sqrt{\sqrt{E-\Delta^2}+\epsilon_F}} \\ &\int_\Delta^\infty dE'\Bigg(e^{-\frac{2mr_c^2}{\hbar^2}(\sqrt{\sqrt{E-\Delta^2}+\epsilon_F)}-\sqrt{\sqrt{E'-\Delta^2}+\epsilon_F)})^2} \\ &-e^{-\frac{2mr_c^2}{\hbar^2}(\sqrt{\sqrt{E-\Delta^2}+\epsilon_F)}+\sqrt{\sqrt{E'-\Delta^2}+\epsilon_F)})^2}\Bigg) \\ &\times\rho(E')M^2(E,E')\bar{f}(E')\,.\end{aligned} \tag{8.55}$$

The above expression is simplified by expanding the squares in the exponential and collecting the common factors

$$\begin{aligned}\gamma_g^{\rm CSL}(E) = &\frac{m^2\lambda r_c}{2\sqrt{\pi}m_0^2}\frac{\sqrt{2m}}{\hbar}\frac{1}{\sqrt{\sqrt{E^2-\Delta^2}+\epsilon_F}}e^{-\frac{2mr_c^2}{\hbar^2}\sqrt{E^2-\Delta^2}} \\ &e^{-\frac{4mr_c^2\epsilon_F}{\hbar^2}}\int_\Delta^\infty dE' e^{-\frac{2mr_c^2}{\hbar^2}\sqrt{E_1^2-\Delta^2}} \\ &\Bigg(e^{\frac{2mr_c^2}{\hbar^2}2(\sqrt{(\sqrt{E^2-\Delta^2}+\epsilon_F)(\sqrt{E'^2-\Delta^2}+\epsilon_F)}} \\ &-e^{-\frac{2mr_c^2}{\hbar^2}2(\sqrt{(\sqrt{E^2-\Delta^2}+\epsilon_F)(\sqrt{E'^2-\Delta^2}+\epsilon_F)}}\Bigg) \\ &\times\rho(E')M^2(E,E')\bar{f}(E')\,.\end{aligned} \tag{8.56}$$

By defining $T_{\rm CSL}$ through $k_B T_{\rm CSL}=\hbar^2/(2mr_c^2)$, and making the substitution $x=E/\Delta$

and $y = E'/\Delta$, we get

$$\begin{aligned}\gamma_g^{\mathrm{CSL}}(x) = &\frac{m^2\lambda r_c}{2\sqrt{\pi}m_0^2}\frac{\sqrt{2m\Delta}}{\hbar}\frac{1}{\sqrt{s(x)+\beta}}e^{-\frac{\Delta}{k_B T_{\mathrm{CSL}}}s(x)} \\ &e^{-\frac{2T_F}{T_{\mathrm{CSL}}}}\int_1^\infty dy\, e^{-\frac{\Delta}{k_B T_{\mathrm{CSL}}}s(y)}\rho(y)M^2(x,y)\bar{f}(\Delta y)) \\ &\left(e^{\frac{2\Delta}{k_B T_{\mathrm{CSL}}}(\sqrt{(s(x)+\beta)(s(y)+\beta)}} - e^{-\frac{2\Delta}{k_B T_{\mathrm{CSL}}}(\sqrt{(s(x)+\beta)(s(y)+\beta)}}\right),\end{aligned} \tag{8.57}$$

where we called $s(x) = \sqrt{x^2-1}$. We can further simplify this expression by neglecting the negative term in the last line because it is exponentially suppressed. We can finally write

$$\begin{aligned}\gamma_g^{\mathrm{CSL}}(x) = &\frac{m^2\lambda r_c}{2\sqrt{\pi}m_0^2}\frac{\sqrt{2m\Delta}}{\hbar}\frac{1}{\sqrt{s(x)+\beta}}e^{-\frac{\Delta}{k_B T_{\mathrm{CSL}}}s(x)} \\ &e^{-\frac{2T_F}{T_{\mathrm{CSL}}}}\int_1^\infty dy\, e^{-\frac{\Delta}{k_B T_{\mathrm{CSL}}}s(y)}\, e^{\frac{2\Delta}{k_B T_{\mathrm{CSL}}}(\sqrt{(s(x)+\beta)(s(y)+\beta)}} \\ &\times\rho(y)\frac{1}{2}\left(1-\frac{\sqrt{x^2-1}\sqrt{y^2-1}}{xy}+\frac{1}{xy}\right)\bar{f}(\Delta y)\,,\end{aligned} \tag{8.58}$$

We solve numerically Eq. (8.52) with $\gamma_g^{\mathrm{ext}} = \gamma_g^{\mathrm{CSL}}$ and $\lambda = 10^{-10}\mathrm{s}^{-1}$. Figure 8.1 shows the evolved occupation function obtained numerically (blue solid line) for a starting equilibrium temperature of 20 mK, which is a typical operational temperature of transmon qubits. The steady state deviates strongly from the starting Fermi Dirac distribution in Eq. (8.16) with $T = 20$ mK, not shown in the figure because too small. Interestingly, the evolved occupation function can not be approximated by a thermal distribution at some effective temperature.

Finally, the steady state quasiparticle density x_{qp}^{CSL} generated by CSL is obtained by using Eq. (8.17) with $f(E)$ given by the evolved quasiparticle occupation function computed with the simulation. x_{qp}^{CSL} turns out to be $\sim 10^{-18}$.

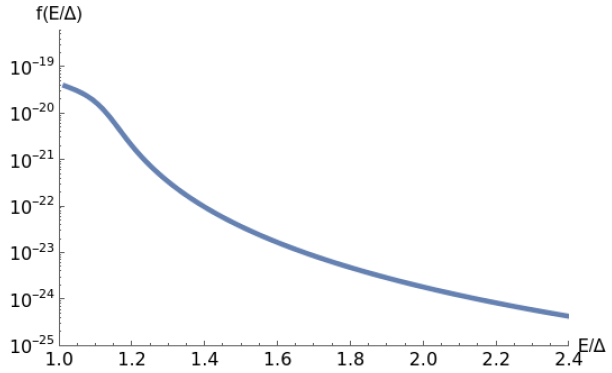

Figure 8.1: Log plot of the quasiparticle occupation function obtained by solving Eq.(8.52) numerically for a starting equilibrium temperature of 20 mK. The evolved occupation function deviates significantly from the initial thermal distribution f_{FD}, here not shown because too small.

This value for the quasiparticle density is ~ 9 orders of magnitude lower than the lowest reported experimental value of $x_{qp} = 10^{-9}$ [105], meaning that environmental noise sources are dominant with the current technological implementation of the transmon qubits. Nevertheless we can use the CSL quasiparticle density to get the limit on the coherence time of transmon qubits set by CSL.

Indeed, for a transmon qubit, the contribution to the relaxation rate due to quasiparticles depends linearly on the normalized quasiparticle density x_{qp} [110, 112–114]

$$\Gamma_1 = \sqrt{\frac{2\omega_q \Delta}{\pi^2 \hbar}} x_{qp} \tag{8.59}$$

where ω_q is the frequency of the qubit (in [112] $\omega_q = 2\pi \times 3.48$ GHz).

Given the obtained value of $x_{qp}^{CSL} \sim 10^{-18}$, we have $\Gamma_1^{CSL} \approx 10^{-6}\text{s}^{-1}$. This is ~ 10 orders of magnitude larger than the CSL reduction rate estimated in section 8.2.1, showing that CSL dissipation is way stronger than the direct collapse process. Note that $T_1^{CSL} = 1/\Gamma_1^{CSL} \approx 10^6$s is anyhow 10 orders of magnitude larger than the $T_1 = 100$ μs of current transmon qubits, showing that CSL dissipation would not influence effectively the performance of a single qubit. In [115] we have investigated the implications of this limitation on a noisy quantum computer comprising many transmon qubits, and we further explored the possibility of testing CSL models with superconducting devices. Detection of CSL effects is currently beyond the experimental sensitivity of superconducting devices, for which other environmental sources are dominant. Experimental test of CSL models may be possible in the future as the technology develops [116], given the importance that superconducting devices have

for quantum computing. In particular, in [115] we show that when a superconducting sample is sufficiently shielded against environmental noises, CSL quasiparticles tunneling through the Josephson junction could be detected at the current refrigerators temperature.

8.3 Discussion

We showed how the CSL model affects superconducting transmon qubits. In particular, the intrinsic localization of superpositions dictated by collapse models leaves the superposition of basis states of transmon qubits intact for very long times. However CSL contributes to decoherence also in an indirect way: dissipation induced by the CSL noise perturbs the superconducting material and leads to the generation of quasiparticles. These accumulate over time inside the volume of the device leading to relaxation at a rate proportional to their density. We estimated the steady state quasiparticle density due to CSL by adding the CSL generation rate of quasiparticles to the kinetic equation for the quasiparticle occupation function. We solved the kinetic equation numerically to find its steady state solution. With this calculation we obtained a lower quasiparticle density than the experimental one, so we conclude that other environmental noise sources are currently giving the dominant contribution to the experimental excess of quasiparticles.

Chapter 9

Summary and outlook

Quantum computers are currently limited by noises and error mitigation strategies will play an increasingly crucial role in suppressing their impact. Research is already moving in this direction showing potential for fruitful outcomes [53]. Still, major advancements are needed to improve the capabilities of error mitigation techniques to realize quantum advantage. In particular, all efforts must be directed into the modeling, characterization and accurate simulations of the effects of noises on quantum computation.

Alignin to this long term goal, the thesis introduced a novel method, the noisy gates approach, for classically simulating the noisy behavior of quantum circuits. The noisy gates approach is shown to surpass other existing methods by offering the most efficient and accurate noisy simulator. By combining environmental effects and gate evolution, it provides a more faithful representation of the interplay between these two competing dynamics. Moreover, computational costs are reduced not only by evolving state vectors instead of density matrices, but also by minimizing the total number of matrix vector multiplications. The improved performance of the noisy gates was shown for superconducting devices and the approach proved to be very versatile, as it was successfully extended to simulate noisy optical circuits within the dual rail framework.

Error analysis is not the only application inspired by the noisy gates approach. The quantum generalization of noisy gates was exploited to introduce an efficient quantum algorithm for simulating open quantum systems.

In the final part of the thesis, the impact of fundamental noises on superconducting transmon qubits was evaluated, specifically focusing on the effects of the CSL collapse model. The direct effect of reducing superpositions of transmon qubits is found to be negligible, while the indirect manifestation of CSL as dissipation-induced decoherence though stronger than loss of coherence is hindered by other excited states generation mechanisms.

The next milestone to be achieved is to show possible improvements on the quality of error mitigation by using the noisy gates approach. A first application is to pair the noisy gates approach with machine learning techniques to perform more effectively Zero Noise Extrapolation (ZNE) [117]. ZNE is an error mitigation strategy that requires to build a curve of noisy expectation values from the same quantum circuit affected by an increasing level of noise and to extrapolate to the zero noise limit. The limiting factor of ZNE is the uncertainty related to the way extrapolation is performed. The noisy gates approach could be exploited to reduce this problem as follows. Assume that a complete underlying noise model of a given device is available such that simulating this noise model with the noisy gates emulates with high accuracy the real quantum hardware. First, simulate classically with the noisy gates method a set of test circuits changing the level of noises to get a training set of extrapolation curves. This allows to vary the noise parameters from the zero noise values so that the full extrapolation curves are available, including the zero noise limit. Then, train a neural network to learn all the features, i.e. symmetries, of the extrapolation curves in the training set. Such features are likely to be present also on unseen data coming from quantum circuits run on real devices for which the zero noise limit is not available. This allows for a more effective extrapolation.

Another error mitigation technique, Probabilistic Error Cancellation (PEC) [52, 117], can benefit from the noisy gates approach. PEC is a stochastic technique that requires to act after ideal gates in a circuit with additional gates realizing on average the inverse (which is not in general a quantum operation) of the quantum operations of the standard noise gate separation method, i.e. the noise term in Eq. (3.3). Adapting PEC to the noisy gates approach would allow to invert the noise channel in Eq. (3.6), that contains more terms to first order in the noise parameters and it is thus more expressive.

Finally, following the research line presented in [54] it is possible to use a tensor network structure to classically simulate an inverting circuit that counteracts the effects of noises and allows to extract useful output from the quantum computer. This technique is very similar to standard PEC, but the inverting circuit is simulated classically and in post processing. The fact that the noisy gates approach is more accurate and uses less computational resources implies that employing it in a tensor network structure allows to build an inverting circuit which is not only more effective but also easier to simulate.

In summary, the noisy gates approach emerges as a key contribution for quantum computation, providing a robust and efficient simulation method that advances our understanding of noisy quantum circuits and opens new avenues for effective error mitigation and, eventually, for practical quantum applications.

Bibliography

[1] Heinz-Peter Breuer, Francesco Petruccione, et al. *The theory of open quantum systems*. Oxford University Press on Demand, 2002.

[2] Michael A Nielsen and Isaac L Chuang. *Quantum computing and quantum information*. Cambridge University Press, Cambridge, 2000.

[3] Vittorio Gorini, Andrzej Kossakowski, and Ennackal Chandy George Sudarshan. Completely positive dynamical semigroups of n-level systems. *Journal of Mathematical Physics*, 17(5):821–825, 1976. doi:https://doi.org/10.1063/1.522979.

[4] Goran Lindblad. On the generators of quantum dynamical semigroups. *Communications in Mathematical Physics*, 48(2):119–130, 1976. doi:https://doi.org/10.1007/BF01608499.

[5] Ibm quantum compute resources, 2022. URL: https://quantum-computing.ibm.com/services/resources.

[6] Giuliano Benenti, Giulio Casati, Davide Rossini, and Giuliano Strini. *Principles of Quantum Computation and Information: A Comprehensive Textbook*. World Scientific, 2019.

[7] Jean Dalibard, Yvan Castin, and Klaus Mølmer. Wave-function approach to dissipative processes in quantum optics. *Phys. Rev. Lett.*, 68:580–583, Feb 1992. URL: https://link.aps.org/doi/10.1103/PhysRevLett.68.580, doi:10.1103/PhysRevLett.68.580.

[8] K. Jacobs and P. L. Knight. Linear quantum trajectories: Applications to continuous projection measurements. *Phys. Rev. A*, 57:2301–2310, Apr 1998. URL: https://link.aps.org/doi/10.1103/PhysRevA.57.2301, doi:10.1103/PhysRevA.57.2301.

[9] Matteo Caiaffa, Andrea Smirne, and Angelo Bassi. Stochastic unraveling of positive quantum dynamics. *Phys. Rev. A*, 95:062101, Jun 2017. URL: https://link.aps.org/doi/10.1103/PhysRevA.95.062101, doi:10.1103/PhysRevA.95.062101.

[10] Angelo Bassi. Stochastic schrödinger equations with general complex gaussian noises. *Phys. Rev. A*, 67:062101, Jun 2003. URL: https://link.aps.org/doi/10.1103/PhysRevA.67.062101, doi:10.1103/PhysRevA.67.062101.

[11] Kurt Jacobs. *Quantum measurement theory and its applications*. Cambridge University Press, 2014.

[12] Howard M Wiseman and Gerard J Milburn. *Quantum measurement and control*. Cambridge university press, 2009.

[13] Angelo Bassi and GianCarlo Ghirardi. Dynamical reduction models. *Physics Reports*, 379(5-6):257–426, 2003. doi:https://doi.org/10.1016/S0370-1573(03)00103-0.

[14] Angelo Bassi, Kinjalk Lochan, Seema Satin, Tejinder P. Singh, and Hendrik Ulbricht. Models of wave-function collapse, underlying theories, and experimental tests. *Rev. Mod. Phys.*, 85:471–527, Apr 2013. URL: https://link.aps.org/doi/10.1103/RevModPhys.85.471, doi:10.1103/RevModPhys.85.471.

[15] Stephen L Adler and Angelo Bassi. Collapse models with non-white noises. *Journal of Physics A: Mathematical and Theoretical*, 40(50):15083, 2007. doi:10.1088/1751-8113/40/50/012.

[16] Sabrina Maniscalco and Francesco Petruccione. Non-markovian dynamics of a qubit. *Phys. Rev. A*, 73:012111, Jan 2006. URL: https://link.aps.org/doi/10.1103/PhysRevA.73.012111, doi:10.1103/PhysRevA.73.012111.

[17] Walter T. Strunz, Lajos Diósi, Nicolas Gisin, and Ting Yu. Quantum trajectories for brownian motion. *Phys. Rev. Lett.*, 83:4909–4913, Dec 1999. URL: https://link.aps.org/doi/10.1103/PhysRevLett.83.4909, doi:10.1103/PhysRevLett.83.4909.

[18] Jay Gambetta and HM Wiseman. The non-markovian stochastic schrödinger equation for the position unravelling. *Journal of Optics B: Quantum and Semiclassical Optics*, 6(8):S821, 2004. doi:10.1088/1464-4266/6/8/031.

[19] CW Gardiner and P Zoller. *Quantum Noise*. Springer-Verlag Berlin, 2004.

[20] Crispin W Gardiner et al. *Handbook of stochastic methods*, volume 3. springer Berlin, 1985.

[21] Kurt Jacobs. *Stochastic processes for physicists: understanding noisy systems*. Cambridge University Press, 2010.

[22] Peter Zoller and C. W. Gardiner. Quantum noise in quantum optics: the stochastic schrödinger equation, 1997. arXiv:quant-ph/9702030.

[23] Md Sajid Anis, Héctor Abraham, R Agarwal AduOffei, Gabriele Agliardi, Merav Aharoni, Ismail Yunus Akhalwaya, Gadi Aleksandrowicz, Thomas Alexander, Matthew Amy, Sashwat Anagolum, et al. Qiskit: An open-source framework for quantum computing. *Qiskit/qiskit*, 2021.

[24] pyQuill, 2022. URL: https://pyquil-docs.rigetti.com/en/v3.3.2/noise.html.

[25] Seyon Sivarajah, Silas Dilkes, Alexander Cowtan, Will Simmons, Alec Edgington, and Ross Duncan. t— ket¿: a retargetable compiler for nisq devices. *Quantum Science and Technology*, 6(1):014003, 2020. doi:10.1088/2058-9565/ab8e92.

[26] Ville Bergholm, Josh Izaac, Maria Schuld, Christian Gogolin, Shahnawaz Ahmed, Vishnu Ajith, M. Sohaib Alam, Guillermo Alonso-Linaje, B. Akash-Narayanan, Ali Asadi, et al. Pennylane: Automatic differentiation of hybrid quantum-classical computations, 2022. arXiv:1811.04968.

[27] Nathan Killoran, Josh Izaac, Nicolás Quesada, Ville Bergholm, Matthew Amy, and Christian Weedbrook. Strawberry Fields: A Software Platform for Photonic Quantum Computing. *Quantum*, 3:129, March 2019. doi:10.22331/q-2019-03-11-129.

[28] Dave Wecker and Krysta M. Svore. Liqui—¿: A software design architecture and domain-specific language for quantum computing, 2014. arXiv:1402.4467.

[29] Cirq, 2022. URL: https://quantumai.google/cirq/noise/representing_noise.

[30] Michael Broughton, Guillaume Verdon, Trevor McCourt, Antonio J. Martinez, Jae Hyeon Yoo, Sergei V. Isakov, Philip Massey, Ramin Halavati, Murphy Yuezhen Niu, Alexander Zlokapa, et al. Tensorflow quantum: A software framework for quantum machine learning, 2021. arXiv:2003.02989.

[31] Gian Giacomo Guerreschi, Justin Hogaboam, Fabio Baruffa, and Nicolas PD Sawaya. Intel quantum simulator: A cloud-ready high-performance simulator of quantum circuits. *Quantum Science and Technology*, 5(3):034007, 2020. doi:10.1088/2058-9565/ab8505.

[32] Paddle Quantum, 2020. URL: https://qml.baidu.com/tutorials/qnn-research/simulating-noisy-quantum-circuits-with-paddle-quantum.html.

[33] Amazon Braket, 2020. URL: https://aws.amazon.com/it/braket/.

[34] Stavros Efthymiou, Sergi Ramos-Calderer, Carlos Bravo-Prieto, Adrián Pérez-Salinas, Diego García-Martín, Artur Garcia-Saez, José Ignacio Latorre, and Stefano Carrazza. Qibo: a framework for quantum simulation with hardware acceleration. *Quantum Science and Technology*, 7(1):015018, 2021. doi:10.1088/2058-9565/ac39f5.

[35] J.R. Johansson, P.D. Nation, and Franco Nori. Qutip: An open-source python framework for the dynamics of open quantum systems. *Computer Physics Communications*, 183(8):1760–1772, August 2012. URL: http://dx.doi.org/10.1016/j.cpc.2012.02.021, doi:10.1016/j.cpc.2012.02.021.

[36] Ludwig Arnold. *Stochastic differential equations: theory and applications*. John Wiley & Sons, 1974.

[37] Philip Krantz, Morten Kjaergaard, Fei Yan, Terry P Orlando, Simon Gustavsson, and William D Oliver. A quantum engineer's guide to superconducting qubits. *Applied Physics Reviews*, 6(2):021318, 2019. doi:https://doi.org/10.1063/1.5089550.

[38] Konstantinos Georgopoulos, Clive Emary, and Paolo Zuliani. Modeling and simulating the noisy behavior of near-term quantum computers. *Phys. Rev. A*, 104:062432, Dec 2021. URL: https://link.aps.org/doi/10.1103/PhysRevA.104.062432, doi:10.1103/PhysRevA.104.062432.

[39] Abdullah Ash-Saki, Mahabubul Alam, and Swaroop Ghosh. Analysis of crosstalk in nisq devices and security implications in multi-programming regime. In *Proceedings of the ACM/IEEE International Symposium on Low Power Electronics and Design*, pages 25–30, 2020. doi:https://doi.org/10.1145/3370748.3406570.

[40] David C. McKay, Christopher J. Wood, Sarah Sheldon, Jerry M. Chow, and Jay M. Gambetta. Efficient z gates for quantum computing. *Phys. Rev. A*,

96:022330, Aug 2017. URL: https://link.aps.org/doi/10.1103/PhysRevA.96.022330, doi:10.1103/PhysRevA.96.022330.

[41] Giovanni Di Bartolomeo, Michele Vischi, Francesco Cesa, Roman Wixinger, Michele Grossi, Sandro Donadi, and Angelo Bassi. Noisy gates for simulating quantum computers. *Phys. Rev. Res.*, 5:043210, Dec 2023. URL: https://link.aps.org/doi/10.1103/PhysRevResearch.5.043210, doi:10.1103/PhysRevResearch.5.043210.

[42] Chad Rigetti and Michel Devoret. Fully microwave-tunable universal gates in superconducting qubits with linear couplings and fixed transition frequencies. *Phys. Rev. B*, 81:134507, Apr 2010. URL: https://link.aps.org/doi/10.1103/PhysRevB.81.134507, doi:10.1103/PhysRevB.81.134507.

[43] Angelo Bassi and Dirk-André Deckert. Noise gates for decoherent quantum circuits. *Phys. Rev. A*, 77:032323, Mar 2008. URL: https://link.aps.org/doi/10.1103/PhysRevA.77.032323, doi:10.1103/PhysRevA.77.032323.

[44] Ibm qiskit, 2022. URL: https://qiskit.org/.

[45] Wolfram Research, Inc. Mathematica, Version 13.1. Champaign, IL, 2022. URL: https://www.wolfram.com/mathematica.

[46] Christopher D Wilen, S Abdullah, NA Kurinsky, C Stanford, L Cardani, G d'Imperio, C Tomei, L Faoro, LB Ioffe, CH Liu, et al. Correlated charge noise and relaxation errors in superconducting qubits. *Nature*, 594(7863):369–373, 2021. doi:https://doi.org/10.1038/s41586-021-03557-5.

[47] Peng Zhao, Kehuan Linghu, Zhiyuan Li, Peng Xu, Ruixia Wang, Guangming Xue, Yirong Jin, and Haifeng Yu. Quantum crosstalk analysis for simultaneous gate operations on superconducting qubits. *PRX Quantum*, 3:020301, Apr 2022. URL: https://link.aps.org/doi/10.1103/PRXQuantum.3.020301, doi:10.1103/PRXQuantum.3.020301.

[48] Peter W Shor. Algorithms for quantum computation: discrete logarithms and factoring. In *Proceedings 35th annual symposium on foundations of computer science*, pages 124–134. Ieee, 1994. doi:10.1109/SFCS.1994.365700.

[49] Lidia Ruiz-Perez and Juan Carlos Garcia-Escartin. Quantum arithmetic with the quantum fourier transform. *Quantum Information Processing*, 16(6):1–14, 2017. doi:https://doi.org/10.1007/s11128-017-1603-1.

[50] John Preskill. Sufficient condition on noise correlations for scalable quantum computing, 2012. arXiv:1207.6131.

[51] Mohan Sarovar, Timothy Proctor, Kenneth Rudinger, Kevin Young, Erik Nielsen, and Robin Blume-Kohout. Detecting crosstalk errors in quantum information processors. *Quantum*, 4:321, September 2020. doi:10.22331/q-2020-09-11-321.

[52] Ewout Van Den Berg, Zlatko K Minev, Abhinav Kandala, and Kristan Temme. Probabilistic error cancellation with sparse pauli–lindblad models on noisy quantum processors. *Nature Physics*, pages 1–6, 2023. doi:https://doi.org/10.1038/s41567-023-02042-2.

[53] Youngseok Kim, Andrew Eddins, Sajant Anand, Ken Xuan Wei, Ewout Van Den Berg, Sami Rosenblatt, Hasan Nayfeh, Yantao Wu, Michael Zaletel, Kristan Temme, et al. Evidence for the utility of quantum computing before fault tolerance. *Nature*, 618(7965):500–505, 2023. doi:https://doi.org/10.1038/s41586-023-06096-3.

[54] Sergei Filippov, Matea Leahy, Matteo A. C. Rossi, and Guillermo García-Pérez. Scalable tensor-network error mitigation for near-term quantum computing, 2023. arXiv:2307.11740.

[55] Zhenyu Cai, Ryan Babbush, Simon C. Benjamin, Suguru Endo, William J. Huggins, Ying Li, Jarrod R. McClean, and Thomas E. O'Brien. Quantum error mitigation. *Rev. Mod. Phys.*, 95:045005, Dec 2023. URL: https://link.aps.org/doi/10.1103/RevModPhys.95.045005, doi:10.1103/RevModPhys.95.045005.

[56] Suguru Endo, Simon C. Benjamin, and Ying Li. Practical quantum error mitigation for near-future applications. *Phys. Rev. X*, 8:031027, Jul 2018. URL: https://link.aps.org/doi/10.1103/PhysRevX.8.031027, doi:10.1103/PhysRevX.8.031027.

[57] Zhiding Liang, Hanrui Wang, Jinglei Cheng, Yongshan Ding, Hang Ren, Zhengqi Gao, Zhirui Hu, Duane S Boning, Xuehai Qian, Song Han, et al. Variational quantum pulse learning. In *2022 IEEE International Conference on Quantum Computing and Engineering (QCE)*, pages 556–565. IEEE, 2022. doi:10.1109/QCE53715.2022.00078.

[58] Mohannad M. Ibrahim, Hamed Mohammadbagherpoor, Cynthia Rios, Nicholas T. Bronn, and Gregory T. Byrd. Evaluation of parameterized quantum circuits with cross-resonance pulse-driven entanglers. *IEEE Transactions*

on Quantum Engineering, 3:1–13, 2022. URL: http://dx.doi.org/10.1109/TQE.2022.3231124, doi:10.1109/tqe.2022.3231124.

[59] Sean Greenaway, Francesco Petiziol, Hongzheng Zhao, and Florian Mintert. Variational quantum gate optimization at the pulse level, 2023. arXiv:2211.16322.

[60] Pieter Kok, W. J. Munro, Kae Nemoto, T. C. Ralph, Jonathan P. Dowling, and G. J. Milburn. Linear optical quantum computing with photonic qubits. *Rev. Mod. Phys.*, 79:135–174, Jan 2007. URL: https://link.aps.org/doi/10.1103/RevModPhys.79.135, doi:10.1103/RevModPhys.79.135.

[61] E. Knill, R. Laflamme, and G. Milburn. Efficient linear optics quantum computation, 2000. arXiv:quant-ph/0006088.

[62] Marlan O Scully and M Suhail Zubairy. *Quantum optics*. Cambridge University Press, 1999.

[63] Werner Vogel and Dirk-Gunnar Welsch. *Quantum optics*. John Wiley & Sons, 2006.

[64] Daniel Klaus Burgarth and Vittorio Giovannetti. Dual-and multi-rail encoding. In *Quantum State Transfer and Network Engineering*, pages 87–122. Springer, 2013. doi:https://doi.org/10.1007/978-3-642-39937-4_3.

[65] Daniel Burgarth and Sougato Bose. Conclusive and arbitrarily perfect quantum-state transfer using parallel spin-chain channels. *Phys. Rev. A*, 71:052315, May 2005. URL: https://link.aps.org/doi/10.1103/PhysRevA.71.052315, doi:10.1103/PhysRevA.71.052315.

[66] Rawad Mezher and Shane Mansfield. Assessing the quality of near-term photonic quantum devices, 2022. arXiv:2202.04735.

[67] Mathias Pont, Riccardo Albiero, Sarah E. Thomas, Nicolò Spagnolo, Francesco Ceccarelli, Giacomo Corrielli, Alexandre Brieussel, Niccolo Somaschi, Hêlio Huet, Abdelmounaim Harouri, Aristide Lemaître, Isabelle Sagnes, Nadia Belabas, Fabio Sciarrino, Roberto Osellame, Pascale Senellart, and Andrea Crespi. Quantifying n-photon indistinguishability with a cyclic integrated interferometer. *Phys. Rev. X*, 12:031033, Sep 2022. URL: https://link.aps.org/doi/10.1103/PhysRevX.12.031033, doi:10.1103/PhysRevX.12.031033.

[68] Artur Czerwinski and Katarzyna Czerwinska. Statistical analysis of the photon loss in fiber-optic communication. In *Photonics*, volume 9, page 568. MDPI, 2022. doi:https://doi.org/10.3390/photonics9080568.

[69] Artur Czerwinski and Jakub Szlachetka. Efficiency of photonic state tomography affected by fiber attenuation. *Phys. Rev. A*, 105:062437, Jun 2022. URL: https://link.aps.org/doi/10.1103/PhysRevA.105.062437, doi:10.1103/PhysRevA.105.062437.

[70] Jakub Mielczarek. Quantum gravity on a quantum chip, 2018. arXiv:1803.10592.

[71] Lucjan Jacak, Pawel Hawrylak, and Arkadiusz Wojs. *Quantum dots*. Springer Science & Business Media, 2013.

[72] Dan Cogan, Oded Kenneth, Netanel H. Lindner, Giora Peniakov, Caspar Hopfmann, Dan Dalacu, Philip J. Poole, Pawel Hawrylak, and David Gershoni. Depolarization of electronic spin qubits confined in semiconductor quantum dots. *Phys. Rev. X*, 8:041050, Dec 2018. URL: https://link.aps.org/doi/10.1103/PhysRevX.8.041050, doi:10.1103/PhysRevX.8.041050.

[73] Sunil Pai, Ben Bartlett, Olav Solgaard, and David A. B. Miller. Matrix optimization on universal unitary photonic devices. *Phys. Rev. Appl.*, 11:064044, Jun 2019. URL: https://link.aps.org/doi/10.1103/PhysRevApplied.11.064044, doi:10.1103/PhysRevApplied.11.064044.

[74] Nicolas Heurtel, Shane Mansfield, Jean Senellart, and Benoît Valiron. Strong simulation of linear optical processes. *Computer Physics Communications*, page 108848, 2023. doi:https://doi.org/10.1016/j.cpc.2023.108848.

[75] Perceval, 2022. URL: https://perceval.quandela.net/docs/.

[76] Scott Aaronson and Daniel J. Brod. Bosonsampling with lost photons. *Phys. Rev. A*, 93:012335, Jan 2016. URL: https://link.aps.org/doi/10.1103/PhysRevA.93.012335, doi:10.1103/PhysRevA.93.012335.

[77] M. Oszmaniec, R. Augusiak, C. Gogolin, J. Kołodyński, A. Acín, and M. Lewenstein. Random bosonic states for robust quantum metrology. *Phys. Rev. X*, 6:041044, Dec 2016. URL: https://link.aps.org/doi/10.1103/PhysRevX.6.041044, doi:10.1103/PhysRevX.6.041044.

[78] Michał Oszmaniec and Daniel J Brod. Classical simulation of photonic linear optics with lost particles. *New Journal of Physics*, 20(9):092002, 2018. doi:10.1088/1367-2630/aadfa8.

[79] Daniel Jost Brod and Michał Oszmaniec. Classical simulation of linear optics subject to nonuniform losses. *Quantum*, 4:267, May 2020. doi:10.22331/q-2020-05-14-267.

[80] Nicolas Heurtel, Andreas Fyrillas, Grégoire de Gliniasty, Raphaël Le Bihan, Sébastien Malherbe, Marceau Pailhas, Eric Bertasi, Boris Bourdoncle, Pierre-Emmanuel Emeriau, Rawad Mezher, Luka Music, Nadia Belabas, Benoît Valiron, Pascale Senellart, Shane Mansfield, and Jean Senellart. Perceval: A Software Platform for Discrete Variable Photonic Quantum Computing. *Quantum*, 7:931, February 2023. doi:10.22331/q-2023-02-21-931.

[81] Javier Osca and Jiri Vala. Implementation of photon partial distinguishability in a quantum optical circuit simulation. *Computer Physics Communications*, 289:108773, 2023. doi:https://doi.org/10.1016/j.cpc.2023.108773.

[82] M. Cerezo, Andrew Arrasmith, Ryan Babbush, Simon C. Benjamin, Suguru Endo, Keisuke Fujii, Jarrod R. McClean, Kosuke Mitarai, Xiao Yuan, Lukasz Cincio, and Patrick J. Coles. Variational quantum algorithms. *Nature Reviews Physics*, 3(9):625–644, August 2021. URL: http://dx.doi.org/10.1038/s42254-021-00348-9, doi:10.1038/s42254-021-00348-9.

[83] Alberto Peruzzo, Jarrod McClean, Peter Shadbolt, Man-Hong Yung, Xiao-Qi Zhou, Peter J Love, Alán Aspuru-Guzik, and Jeremy L O'brien. A variational eigenvalue solver on a photonic quantum processor. *Nature communications*, 5(1):4213, 2014. doi:https://doi.org/10.1038/ncomms5213.

[84] Johan Håstad. Some optimal inapproximability results. *Journal of the ACM (JACM)*, 48(4):798–859, 2001. doi:https://doi.org/10.1145/502090.502098.

[85] Piotr Berman and Marek Karpinski. On some tighter inapproximability results. In *Automata, Languages and Programming: 26th International Colloquium, ICALP'99 Prague, Czech Republic, July 11–15, 1999 Proceedings 26*, pages 200–209. Springer, 1999.

[86] Massimiliano Proietti, Filippo Cerocchi, and Massimiliano Dispenza. Native measurement-based quantum approximate optimization algorithm applied to the max k-cut problem. *Phys. Rev. A*, 106:022437, Aug 2022. URL: https://link.aps.org/doi/10.1103/PhysRevA.106.022437, doi:10.1103/PhysRevA.106.022437.

[87] scipy COBYLA documentation, 2023. URL: https://docs.scipy.org/doc/scipy/reference/optimize.minimize-cobyla.html.

[88] Yuxuan Du, Zhuozhuo Tu, Xiao Yuan, and Dacheng Tao. Efficient measure for the expressivity of variational quantum algorithms. *Phys. Rev.*

Lett., 128:080506, Feb 2022. URL: https://link.aps.org/doi/10.1103/PhysRevLett.128.080506, doi:10.1103/PhysRevLett.128.080506.

[89] Michele Vischi, Giovanni Di Bartolomeo, Massimiliano Proietti, Seid Koudia, Filippo Cerocchi, Massimiliano Dispenza, and Angelo Bassi. Simulating photonic devices with noisy optical elements, 2023. arXiv:2311.10613.

[90] Edward Farhi, Jeffrey Goldstone, and Sam Gutmann. A quantum approximate optimization algorithm, 2014. arXiv:1411.4028.

[91] Nicolas Maring, Andreas Fyrillas, Mathias Pont, Edouard Ivanov, Petr Stepanov, Nico Margaria, William Hease, Anton Pishchagin, Thi Huong Au, Sébastien Boissier, et al. A general-purpose single-photon-based quantum computing platform, 2023. arXiv:2306.00874.

[92] Ryan Sweke, Ilya Sinayskiy, Denis Bernard, and Francesco Petruccione. Universal simulation of markovian open quantum systems. *Phys. Rev. A*, 91:062308, Jun 2015. URL: https://link.aps.org/doi/10.1103/PhysRevA.91.062308, doi:10.1103/PhysRevA.91.062308.

[93] Wibe A. de Jong, Mekena Metcalf, James Mulligan, Mateusz Płoskoń, Felix Ringer, and Xiaojun Yao. Quantum simulation of open quantum systems in heavy-ion collisions. *Phys. Rev. D*, 104:L051501, Sep 2021. URL: https://link.aps.org/doi/10.1103/PhysRevD.104.L051501, doi:10.1103/PhysRevD.104.L051501.

[94] Marco Cattaneo, Gabriele De Chiara, Sabrina Maniscalco, Roberta Zambrini, and Gian Luca Giorgi. Collision models can efficiently simulate any multipartite markovian quantum dynamics. *Phys. Rev. Lett.*, 126:130403, Apr 2021. URL: https://link.aps.org/doi/10.1103/PhysRevLett.126.130403, doi:10.1103/PhysRevLett.126.130403.

[95] Marco Cattaneo, Matteo A.C. Rossi, Guillermo García-Pérez, Roberta Zambrini, and Sabrina Maniscalco. Quantum simulation of dissipative collective effects on noisy quantum computers. *PRX Quantum*, 4:010324, Mar 2023. URL: https://link.aps.org/doi/10.1103/PRXQuantum.4.010324, doi:10.1103/PRXQuantum.4.010324.

[96] Richard Cleve and Chunhao Wang. Efficient quantum algorithms for simulating lindblad evolution, 2019. arXiv:1612.09512.

[97] Hirsh Kamakari, Shi-Ning Sun, Mario Motta, and Austin J. Minnich. Digital quantum simulation of open quantum systems using quantum imaginary–time

evolution. *PRX Quantum*, 3:010320, Feb 2022. URL: https://link.aps.org/doi/10.1103/PRXQuantum.3.010320, doi:10.1103/PRXQuantum.3.010320.

[98] M. Kliesch, T. Barthel, C. Gogolin, M. Kastoryano, and J. Eisert. Dissipative quantum church-turing theorem. *Phys. Rev. Lett.*, 107:120501, Sep 2011. URL: https://link.aps.org/doi/10.1103/PhysRevLett.107.120501, doi:10.1103/PhysRevLett.107.120501.

[99] Luca Ferialdi and Angelo Bassi. Continuous spontaneous localization reduction rate for rigid bodies. *Phys. Rev. A*, 102:042213, Oct 2020. URL: https://link.aps.org/doi/10.1103/PhysRevA.102.042213, doi:10.1103/PhysRevA.102.042213.

[100] John Robert Schrieffer. *Theory of superconductivity*. CRC press, 2018.

[101] Giuseppe Grosso and Giuseppe Pastori Parravicini. *Solid state physics*. Academic press, 2013.

[102] Michael Tinkham. *Introduction to superconductivity*. Courier Corporation, 2004.

[103] G. Catelani, J. Koch, L. Frunzio, R. J. Schoelkopf, M. H. Devoret, and L. I. Glazman. Quasiparticle relaxation of superconducting qubits in the presence of flux. *Physical Review Letters*, 106(7), February 2011. URL: http://dx.doi.org/10.1103/PhysRevLett.106.077002, doi:10.1103/physrevlett.106.077002.

[104] P. J. de Visser, D. J. Goldie, P. Diener, S. Withington, J. J. A. Baselmans, and T. M. Klapwijk. Evidence of a nonequilibrium distribution of quasiparticles in the microwave response of a superconducting aluminum resonator. *Phys. Rev. Lett.*, 112:047004, Jan 2014. URL: https://link.aps.org/doi/10.1103/PhysRevLett.112.047004, doi:10.1103/PhysRevLett.112.047004.

[105] K. Serniak, S. Diamond, M. Hays, V. Fatemi, S. Shankar, L. Frunzio, R.J. Schoelkopf, and M.H. Devoret. Direct dispersive monitoring of charge parity in offset-charge-sensitive transmons. *Phys. Rev. Appl.*, 12:014052, Jul 2019. URL: https://link.aps.org/doi/10.1103/PhysRevApplied.12.014052, doi:10.1103/PhysRevApplied.12.014052.

[106] Matteo Carlesso and Sandro Donadi. Collapse models: main properties and the state of art of the experimental tests. In *Advances in Open Systems and Fundamental Tests of Quantum Mechanics*, pages 1–13. Springer, 2019. doi:https://doi.org/10.1007/978-3-030-31146-9_1.

[107] Stephen L Adler. Lower and upper bounds on csl parameters from latent image formation and igm heating. *Journal of Physics A: Mathematical and Theoretical*, 40(12):2935, 2007. doi:10.1088/1751-8113/40/12/S03.

[108] Chen Wang, Yvonne Y Gao, Ioan M Pop, Uri Vool, Chris Axline, Teresa Brecht, Reinier W Heeres, Luigi Frunzio, Michel H Devoret, Gianluigi Catelani, et al. Measurement and control of quasiparticle dynamics in a superconducting qubit. *Nature communications*, 5(1):1–7, 2014. doi:https://doi.org/10.1038/ncomms6836.

[109] Jens Koch, Terri M. Yu, Jay Gambetta, A. A. Houck, D. I. Schuster, J. Majer, Alexandre Blais, M. H. Devoret, S. M. Girvin, and R. J. Schoelkopf. Charge-insensitive qubit design derived from the cooper pair box. *Phys. Rev. A*, 76:042319, Oct 2007. URL: https://link.aps.org/doi/10.1103/PhysRevA.76.042319, doi:10.1103/PhysRevA.76.042319.

[110] John M. Martinis, M. Ansmann, and J. Aumentado. Energy decay in superconducting josephson-junction qubits from nonequilibrium quasiparticle excitations. *Phys. Rev. Lett.*, 103:097002, Aug 2009. URL: https://link.aps.org/doi/10.1103/PhysRevLett.103.097002, doi:10.1103/PhysRevLett.103.097002.

[111] DJ Goldie and S Withington. Non-equilibrium superconductivity in quantum-sensing superconducting resonators. *Superconductor Science and Technology*, 26(1):015004, 2012. doi:10.1088/0953-2048/26/1/015004.

[112] Antti P Vepsäläinen, Amir H Karamlou, John L Orrell, Akshunna S Dogra, Ben Loer, Francisca Vasconcelos, David K Kim, Alexander J Melville, Bethany M Niedzielski, Jonilyn L Yoder, et al. Impact of ionizing radiation on superconducting qubit coherence. *Nature*, 584(7822):551–556, 2020. doi:https://doi.org/10.1038/s41586-020-2619-8.

[113] G. Catelani, R. J. Schoelkopf, M. H. Devoret, and L. I. Glazman. Relaxation and frequency shifts induced by quasiparticles in superconducting qubits. *Phys. Rev. B*, 84:064517, Aug 2011. URL: https://link.aps.org/doi/10.1103/PhysRevB.84.064517, doi:10.1103/PhysRevB.84.064517.

[114] Leonid I. Glazman and Gianluigi Catelani. Bogoliubov quasiparticles in superconducting qubits. *SciPost Phys. Lect. Notes*, page 31, 2021. URL: https://scipost.org/10.21468/SciPostPhysLectNotes.31, doi:10.21468/SciPostPhysLectNotes.31.

[115] Michele Vischi, Luca Ferialdi, Andrea Trombettoni, and Angelo Bassi. Possible limits on superconducting quantum computers from spontaneous wave-function collapse models. *Phys. Rev. B*, 106:174506, Nov 2022. URL: https://link.aps.org/doi/10.1103/PhysRevB.106.174506, doi:10.1103/PhysRevB.106.174506.

[116] Laura Cardani, Francesco Valenti, Nicola Casali, Gianluigi Catelani, Thibault Charpentier, Massimiliano Clemenza, Ivan Colantoni, Angelo Cruciani, G D'Imperio, L Gironi, et al. Reducing the impact of radioactivity on quantum circuits in a deep-underground facility. *Nature communications*, 12(1):1–6, 2021. doi:https://doi.org/10.1038/s41467-021-23032-z.

[117] Kristan Temme, Sergey Bravyi, and Jay M. Gambetta. Error mitigation for short-depth quantum circuits. *Phys. Rev. Lett.*, 119:180509, Nov 2017. URL: https://link.aps.org/doi/10.1103/PhysRevLett.119.180509, doi:10.1103/PhysRevLett.119.180509.